Alma Mater Studiorum - Università di Bologna

DOTTORATO DI RICERCA IN

CHIMICA

Ciclo 33

Settore Concorsuale: 03/A1 - CHIMICA ANALITICA

Settore Scientifico Disciplinare: CHIM/01 - CHIMICA ANALITICA

CHEMILUMINESCENCE DNA-BASED NANOTECHNOLOGIES FOR BIOANALYTICAL APPLICATIONS

Presentata da: Elisa Marchegiani

Coordinatore Dottorato

Domenica Tonelli

Supervisore

Mara Mirasoli

Co-supervisore

Massimo Guardigli

Esame finale anno 2021

CONTENTS

ABSTRACT

DNA as powerful *building molecule,* is widely used for the assembly of molecular structures and dynamic molecular devices with different potential applications, ranging from synthetic biology to diagnostics. The feature of sequence programmability, which makes it possible to predict how single stranded DNA molecules fold and interact with one another, allowed the development of spatiotemporally controlled nanostructures and the engineering of supramolecular devices.

The first part of this thesis addresses the development of an integrated chemiluminescence (CL)-based lab-on-chip sensor for detection of Adenosine-5-triphosphate (ATP) life biomarker in extra-terrestrial environments. We choose ATP according to the idea that life developed on extra-terrestrial environments following the same evolutionary principles as Earth, ATP could be detected in the presence of an organism's activity. Our approach is based on a structure-switching ATP-binding DNA aptamer. We engineered a stem loop structure with two functional domains: a catalytic DNAzyme domain and an ATP aptamer binding domain. The sensor can be described as an equilibrium between two conformational states, "off state" and "binding competent state". In the presence of ATP, we can observe a shift from the "off state" to "on state", that allows the correct G-quadruplex structure folding. Adding hemin, a small molecule with a peroxidase activity, its substrate, luminol, and hydrogen peroxide, we obtain a significant chemiluminescent signal emission. Chemiluminescence readout was chosen to improve the detectability of the sensor, as CL ensures high analytical performance without external radiation sources and complex optical systems.

Subsequently, we investigated whether it is possible to study the interaction and the recognition between biomolecules and their targets, mimicking the intracellular environment in terms of crowding, confinement and compartmentalization. To this purpose, we developed a split G-quadruplex DNAzyme platform for the chemiluminescent and quantitative detection of antibodies based on antibody-induced co-localization proximity mechanism in which a split G-quadruplex DNAzyme is led to reassemble into the functional native G-quadruplex conformation as the effect of a guided spatial nanoconfinement.

The following part of this thesis aims at developing chemiluminescent nanoparticles for bioimaging and photodynamic therapy applications. The innovative approach consists in employing the light emission generated by chemiluminescent reaction as source of light for photodynamic therapy (PDT). Indeed, the aim of the project consists in the construction of a breakable shell around the enzyme that can be released from the stimulus-responsive container once internalized into cells. The natural reducing environment of the cancer cells, due to the presence of high concentration of glutathione, is used to trigger the disruption of the shell of silica nanoparticles, which release the enzyme for carrying out the luminescent reaction, with a consequent generation of light.

In chapter5 a realistic and accurate evaluation of the potentiality of electrochemistry and chemiluminescence (CL) for biosensors development (i.e., is it better to "measure an electron or a photon"?), has been achieved. During the last few decades, different transduction principles, from electrochemical (such as conductometric, voltammetric, potentiometric, amperometric, and impedimetric detection), through optical (including absorbance/reflectometry, photoluminescence, bio-chemiluminescence (BL/CL), and thermochemiluminescence), hybrid photon-electron systems (such as electrogenerated chemiluminescence (ECL) and photoelectrochemistry) have been proposed in the attempt to achieve ultrasensitive detection, fast response time and cost-effectiveness in biosensor development. Nevertheless, a literature-based comparison is not possible, as different conditions are employed in each paper. In this study, which measurement, photons or electrons, yields better biosensor performance has been evaluated directly comparing amperometry and chemiluminescence-based biosensors with the same biospecific reagents and analytical formats.

In chapter 6 the emission anisotropy phenomenon for an emitting dipole bound to the interface between two media with different refractive index has been investigated for chemiluminescence detection. We propose a simple method for the real-time evaluation of the chemiluminescence emission anisotropy based on a radial array of optical fibers, embedded in a poly (methyl methacrylate) (PMMA) semicylinder and coupled with a Charge-Coupled Device (CCD) camera through a suitable interface. Evidence of the anisotropy phenomenon is observed, opening new perspectives in the development of CL-based miniaturized analytical devices.

ACKNOWLEDGEMENTS

First and foremost, I would like to deeply thank my supervisors Prof. Mara Mirasoli and Prof. Massimo Guardigli for their invaluable guidance and wisdom, their trust and support, patience and motivation, and the great opportunity they gave me of carrying out this project. Thank you for always answering my questions and for teaching me about thinking creatively and problem solving.

I am deeply grateful to Prof. Aldo Roda for his efforts in terms of time, ideas, motivation, tutelage, and immense knowledge towards my Ph.D. work. I must say that your passion and enthusiasm are contagious, and I am glad our path crossed; thanks for sowing a part of your knowledge and experience into my career.

My sincere thanks go to Dr. Martina Zangheri and Dr. Donato Calabria for introducing me to research areas of chemiluminescence immunoassay and microfluidic biosensor technologies, your contribution toward my experimental work is highly appreciated, thanks so much.

Likewise, I was given the chance to work with an amazing set of scientists, in particular Prof. Michael J. Sailor and Prof. Luisa De Cola, who gave me interesting insights into porous silicon nanomaterials and supramolecular structures, thanks for providing me the opportunity to carry out the research in your lab and for your support, encouragement, advice, and enthusiasm.

I would also like to thank all group members, both past and present, who made the countless hours spent in the laboratory a joyful experience.
Outside of lab-life, the wonderful array of friends who provided fantastic support, making the last three years unforgettable. It has always been great inspiration.

Most importantly, I would like to thank my mother and my sisters, for their unconditional love, support, motivation, and humour.

1

INTRODUCTION TO DNA AND DNA NANOTECHNOLOGY

1.1 DNA

1.1.1 STRUCTURE AND PROPERTIES OF DNA

The double helix structure of DNA was elucidated for the first time by James Watson and Francis Crick, who developed a three-dimensional model of DNA based on X-ray diffraction studies conducted by Rosalind Franklin. The two scientists announced their revolutionary results in a famous paper of April 1953 as follows: "We wish to suggest a structure for the salt of deoxyribose nucleic acid (D.N.A.). This structure has novel features which are of considerable biological interest" [1, 2]. Since then, the central role of DNA in biology as bearer of genetic code was determined, inducing a great scientific interest in the decryption of many genomic sequences as well as the human genome [3]. However, the story is far from over, and many questions still remain to be answered, in particular, the details of supramolecular DNA behaviour, including the sequence-dependent local structure, protein binding to DNA, and the regulation of gene expression (as methylation of DNA and selective unwinding from histones).

Later, the self-assembly ability of this biopolymer inspired several fields of research on new oligonucleotide-based systems from synthetic chemistry, bioanalytical methods, biophysics and even computer programming. The basic principle of DNA self-assembly-based chemistry is simple: the molecule forms a well-understood double helix through the predictable complementary base pairing of two antiparallel strands [4].

A DNA strand is a polynucleotide chain composed of four types of nucleotides covalently linked together. The structure of a nucleotide comprises a five-carbon deoxyribose sugar to which a single phosphate group is attached [5]. What holds together the nucleotides of each single DNA strand are phosphodiester type bonds, which are present between the phosphate group of a nucleotide and the so-called "carbon 5" of the immediately following nucleotide. The phosphate groups are negatively charged and therefore confer the DNA polymer an overall negative charge. An N-glycosidic bond links the base to a carbon on the deoxyribose sugar [6]. The bases, which extend from the sugar, may be adenine (A), cytosine (C), guanine (G), or thymine (T). Both A and G are purine molecules and comprise two aromatic rings, whereas T and C, the pyrimidines, have just one aromatic ring [7]. The bases are depicted in Figure 1 b.

DNA strands are inherently polar, and the DNA molecule comprises two complementary, anti-parallel strands, which are held together by hydrogen bonds [7]. Polarity is indicated either by a 5′ phosphate group or a 3′ hydroxyl group (named after the location of the group on either the 5′ or 3′ carbon of the sugar ring) [8]. The DNA helical configuration, ascribable to the reciprocal winding of the filaments in antiparallel directions of oligonucleotides, generates two grooves, one wider than the other: the major and the minor groove. So called ‘base-pairs’ arise between A and T (which form two hydrogen bonds) and G and C (which form three hydrogen bonds). Additionally, neighbouring bases in the twisted helix are involved in non-covalent π-π orbital stacking interactions which arise between π orbitals in adjacent aromatic rings and play a major role in stabilising the helix [9]. DNA may be mechanically rigid or flexible. Naturally occurring ds 'B-form' DNA, the most present in nature, wraps around itself forming a plectonemic coil, characterized by a persistence length of 40-50 nm, which roughly corresponds to 150 base pairs (bps) [10-12]. A double helix spans approximately 2 nm in diameter, and each helical turn comprises 10.5 bps with a length of 3.6 nm (see Figure 1 a), which depends on the salt concentration of the solution and the sequence [5, 13]. B-form DNA has an intrinsic righthanded (RH) chirality, but 'Z-form' DNA, among less common forms also existing in nature, adopts a left-handed (LH) conformation. For instance, Z-form DNA is assembled from regions of alternating purines and pyrimidines such as GCGCGCGC. In this thesis we are primarily concerned with B-form DNA [14, 15].

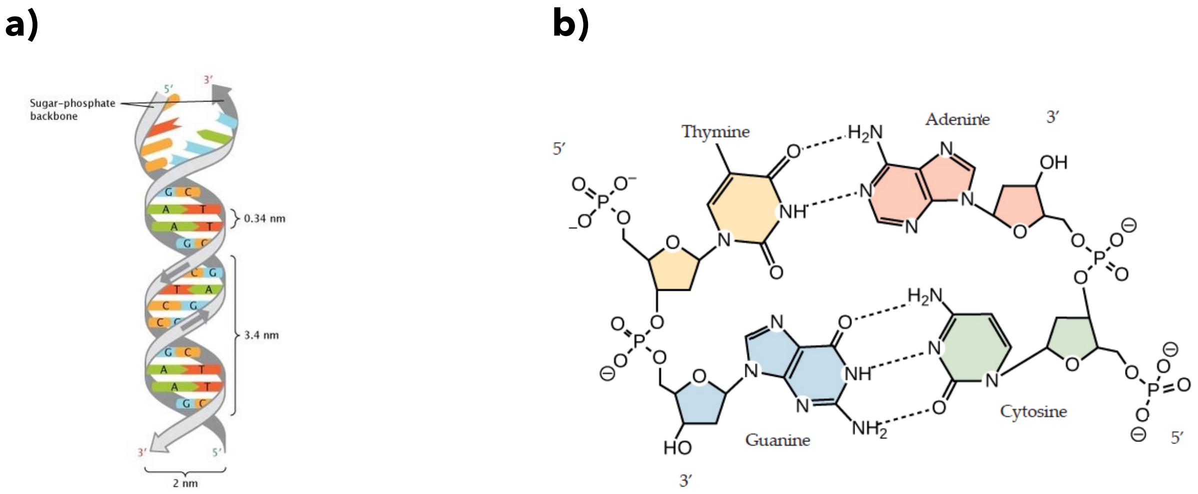

Figure 1: The structure and properties of DNA. a) DNA has a pitch of 0.34 nm per base and of 1.36 nm per helical turn. The width of a helix is roughly 2 nm. [16] The bases of DNA are adenine, guanine, cytosine and thymine and comprise one or two aromatic rings depending on whether the base is a purine or pyrimidine, respectively.

1.1.2 DNA AS A BUILDING MATERIAL: FUNCTIONAL DNA NANOTECHNOLOGIES

The countless possibilities of creating DNA structures are key ingredients at the base of DNA nanotechnology. DNA can assume both a rigid conformation (duplex) and a flexible structure (single strand), thus providing the possibility of creating architectures with nanometric precision through a complementarity mechanism similar to Lego bricks. Furthermore, multiple tertiary structures are possible, such as loops, triple strands, quadruplexes and various junctions, very common in complex biological systems [17]. In 1980, the pioneer of the field of structural DNA nanotechnology, Nadrian Seeman, while at a campus pub was inspired by M. C. Escher woodcut "*Depth*" and imagined handling DNA outside of its traditional biological context, creating a three-dimensional lattice, using DNA as a structural building material [18].

After an initial strong interest in the mechanization of DNA nanostructures [11,12] based on the dynamism of such structures, whose functions depend on the change of their conformations, the vast advances in DNA nanotechnology have turned to the improvement of geometric complexity structural DNA nanotechnology, considered as a static object. Over the past decade, a huge increase in interest in dynamic DNA nanotechnology and nanoscale DNA testing devices [13] has led to several applications, including but not limited to sensors [14-20], molecular algorithms [18, 21-23], biological assays [24-26], cargo sorting devices [27] and delivery [28-31], tunable plasmonic devices [32-36] and nano-scale robotic arms [37,38]. Whether simple or complex, the incorporation of dynamic mechanisms into DNA systems can dramatically boost their potential applications. In general, artificial molecular machines and devices can be designed using two different approaches. One approach consists in the design according to the principles of mechanical engineering, and, consequently, input to a device will produce a single response [29]. Devices can also be engineered to mimic biomolecular machines like enzymes and molecular motors which are inherently flexible. Based on the tremendous progress achieved in both DNA nanotechnology and in the study of functional DNA, it is natural to combine these two exciting fields to create a new interdisciplinary field that uses functional DNA to control and fine-tune the structure and dynamics of DNA nanostructures and materials [12-18]. Because new DNA functions always involve interactions with other chemical and biological molecules, they brought to the generation of 'smart' nanoscale architectures, which assembly and function are responsive to chemical or biological stimuli. The change in chemical or physical properties of the devices can be used to detect those stimuli in a highly sensitive and selective manner [21-33].

An ideal approach to modelling dynamic DNA nanostructures is based on the binding of an external strand. The most used method is the toehold-mediated strand displacement (TMSD) method [12,38,39]. As illustrated in Fig. 2a and b, a DNA strand acting as "invading set" displaces an "incumbent" DNA strand hybridized to a single-stranded region of the DNA device. This displacement process is initiated at a short unhybridized region or ''toehold''. The energy needed for the displacing mechanism through TMSD is provided by the difference in the free energies of hybridization of the incumbent and invader strands [41]. The kinetics of TMSD [40,42] can be controlled by the length of the toehold, up to a length of about 5 to 7 nucleotides (nt), beyond which the rate constant becomes independent of toehold length [40]. Device applications of TMSD include precisely controlled DNA walkers [37], DNA tweezers [35,36], biologically-inspired linear actuators [38], drug-containing boxes which release drugs upon exposure to DNA sequences that are known markers of diseases [33-38], as shown in Figure2.

Research in recent years has focused on the specificity of the sequence: changing its order can increase the degrees of freedom of dynamic systems, induced by the desired conformational changes.

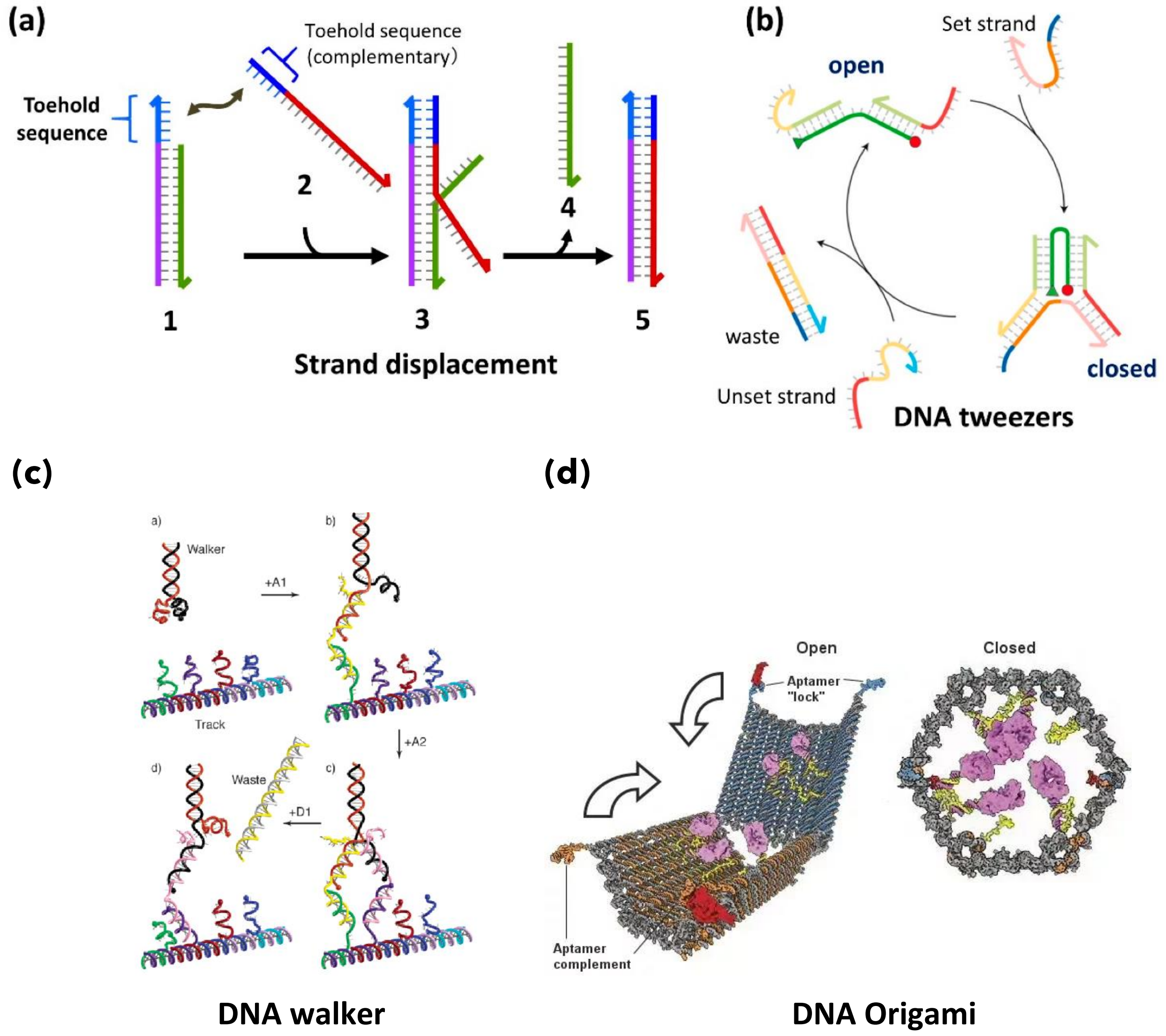

Figure2. Molecular binding-based DNA device actuation. (a) TMSD mechanism. (b) First application of TMSD to make a pair of ‘‘tweezers’’ which close and open with the addition of fuel (F) or antifuel (F-bar) strands, respectively. (c) Schematic of a DNA walker. The walker is bound on a track through partial base-pairing with complementary anchor strands. Introduction of fuel strands replaces walker foot on the anchorage and recycles the walker to the higher free energy state. (d) Upon the introduction of a protein matching the aptamer formed by the blue strand, the blue strand tends to dissociate from the orange strand and bind the

target. When this happens on both sides of the DNA device, the latter is no longer held shut and spring energy drives the device open. [*Reprinted with permission from M. DeLuca et al., Dynamic DNA nanotechnology: toward functional nanoscale devices; Nanoscale Horiz., 2020, 5, 182-201*].

1.2 DNA CONFORMATIONAL SWITCHES AND ALLOSTERY: NATURE-INSPIRED POPULATION SHIFT MECHANISMS

During the last twenty years, several efforts have been addressed to build fine-tuned molecular machines that perform specific tasks at the nanoscale [41]. Since new DNA functions always involve interactions with other chemical and biological molecules, they allow the generation of ‘smart’ nanoscale architectures; responsive to chemical or biological stimuli [42]. Compared with DNA nanotechnology based on base-pair hybridizations, nanotechnologies based on functional DNA could potentially be more versatile and dynamic. The change in chemical or physical properties of the system can be used to detect those stimuli in a highly sensitive and selective way [43].

Inspired by Nature, strong efforts to re-create *in vitro* artificial switches using synthetic molecules or re-engineered biomolecules have been done [44]. In response to different stimuli, for example, cells and organisms have evolved different mechanisms able to adjust rapidly and precisely to both extracellular and intracellular changes [44]. Conformational changes and the oligomerization state of biomacromolecules induced by interaction with specific targets are the basis of most of these natural mechanisms, in which biopolymers act as molecular switches [45]. In order to regulate the affinities of biomolecules and, through this, to control cellular processes and pathways, living organisms usually employ allosteric effectors that act on a distal site on the biomolecule to modulate the overall affinity with which a second ligand (i.e. target) binds to the receptor, as depicted in Figure 3.

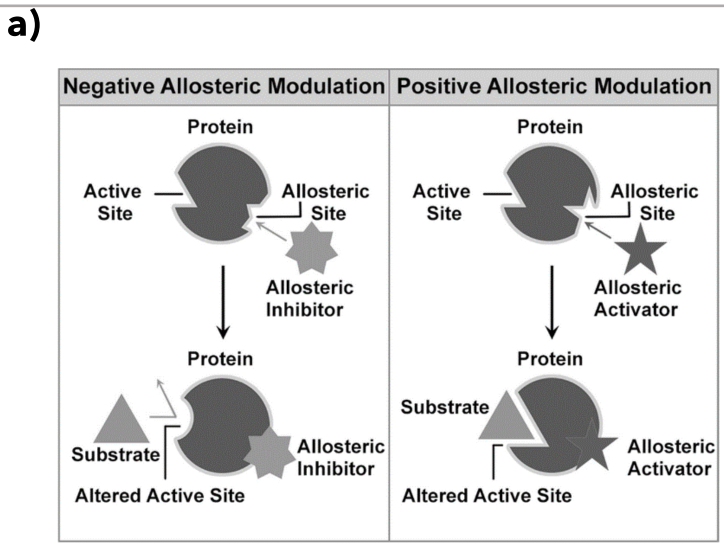

Reprinted with permission from: Cheng X., Jiang H., vol 1163. Springer, . (2019)

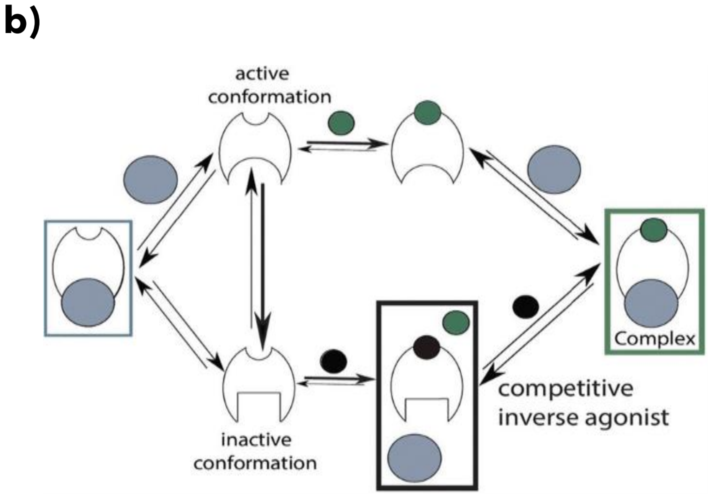

Reprinted with permission from: Gavriilidou, A.F.M., Hunziker, H., Mayer, D. *et al.* . *J. Am. Soc. Mass Spectrom.* **30,** 529–537 (2019).

Figure3. Schematic representation of the binding mechanism. A)The binding to the receptor allows a conformational change that triggers protein shift functionality. B) The receptor is depicted in an equilibrium of active and inactive conformations, whereas the inactive population is in general much more occupied. Many naturally occurring chemo-receptors work via a population-shift mechanism in which target binding pushes a pre-existing equilibrium between the binding-competent state and the non-binding state to the bound state (Top). In allosterically regulated switches, the binding of an external effector stabilizes either the non-binding state (bottom) or competent-binding states of the receptor thus reducing or improving the overall affinity for the target.

In particular, DNA-based switches represent an emerging class of structure-switching receptors whose structure and function are regulated by the interaction with specific molecular and chemical inputs. The use of DNA-based switches (DNA-switches) presents many advantages so that they have been implemented in a wide range of artificial technologies in the areas of smart materials, diagnostics, imaging, and biosensing [46-51]. This class of DNA receptors has a high selectivity and this is not influenced by non-specific interactions with interfering proteins, therefore it can be considered as an excellent candidate for applications in real samples and matrices, such as biological fluids [52,53]. The main strategy for engineering DNA-switches is based on the generation of an inactive conformation unable to bind the target (the non-binding "off" state; Fig. 3b bottom). The non-binding state of DNA-switches can be engineered and tuned via the insertion of non-native interactions at the molecular level (i.e., for example, the introduction of Watson-Crick interactions) in order to combine input recognition to structural motion. DNA switches are therefore realized to selectively bind to a molecular input that induces a structural change from a non-binding conformation to a specific second conformation. Precisely, DNA-switch mechanism consists in the shift from a non-binding conformation to a second binding-competent conformation, upon the recognition of a specific molecular input (Fig. 3b, top) [57]. Indeed, the binding of the target stabilizes the latter state, modifying the pre-existing equilibrium and thus coupling recognition with a wide spectrum of conformational switches and a stable output. Label-free strategy based on the use of unmodified DNA [58-60] with chemiluminescence readout [51-53] have been developed to overcome the need of labeled oligonucleotide or bioconjugation steps (i.e., oligonucleotides anchored on metal surfaces) [54]. Indeed, the introduction of non-native interactions into the DNA-switches structure can negatively influence the thermodynamics of the recognition mechanism, increasing the activation energy of the transition state necessary to reach an unfavorable conformation. The resulting reduced affinity between active site and target molecule results in a larger signal change, lower dynamic range and worse detection limits [55,56]. However, a wide range of inputs that can be used to induce such switching, including complementary nucleic acid strands [57,58] as well as small molecules or protein targets (i.e., through the use of aptamer sequences or consensus binding sequence) [59-63].

A second advantage is the ease with which secondary chemical and biological effectors can be used to modulate biomolecular functions via a mechanism called “allostery”, which consists in the binding of the external effector (i.e., nucleic acid complementary sequence, small molecule, protein) able to stabilize either the binding-competent or non-binding states (respectively) of the DNA-based receptor, improving (Fig. 3a, right) or reducing (Fig. 3a, left) the overall affinity for its target (Kd). On the other hand, the possibility to design DNA-based receptors with an increasing affinity modulated by self-induced conformational changes, due to the allosteric properties, represents the main advantage of these molecular machines. Moreover, it has also been demonstrated that allosteric control does not affect the specificity of the biomolecule for its target because the distal site binding event of the external effector to the receptor does not interact with the target-receptor interface.

1.3 APTAMERS AND DNAZYMES: A NOVEL MOLECULAR TOOLKIT

Since the early 1990s, many DNA molecules – known as DNA aptamers – have been isolated that are able to bind a broad range of molecules with high affinity and specificity [64, 65]. The molecules that can be recognized by aptamers range from small organic molecules to proteins, cells and even intact viral particles [66], as depicted in Figure4. The versatility of aptamers comes from a wide range of sequences able to shape their three-dimensional structure in a complementary and selective way to the target biomarker and to form a number of non-covalent bonds between its bind pocket and the target protein or small molecule [103].

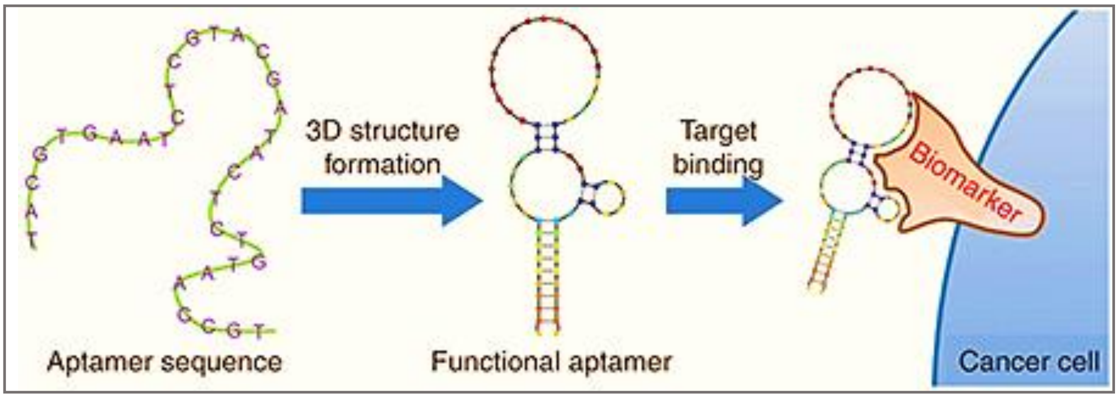

Reprinted with permission from: Hongguang S., Xun Z., *et al.*, *Mol Ther Nucleic Acids*.; **3(8)**: e182(2014)

Figure4.Aptamers are oligonucleotide sequences that form functional 3D structures and they are able to bind to their targets with high specificity and affinity.

Aptamers can be synthesized to bind to a wide range of chemical and biological targets from small molecules to whole cells. The process used to isolate aptamers from large random-sequence libraries is called *in vitro* selection, the so-called SELEX method (Systematic Evolution of Ligands by Exponential Enrichment), first introduced by Tuerk and Gold in 1990 [67–69]. Similar to natural selection, SELEX consists of an iterative selection and amplification of a large pools of nucleic acid molecules (typically >1 trillion distinct sequences) able to bind to a desired target under a defined set of conditions (for example, temperature and salt concentration). Molecules bound to the target are isolated from the unbound pool and subsequently amplified to generate a new population of molecules, enriched in members with common functional property [68], as shown in Figure5. The first aptamers composed exclusively of RNA sequences were revealed in 1990 by Ellington and Szostak, who would later win the 2009 Nobel Prize in Medicine [70]. Aptamers are often compared with antibodies, as both molecules function as affinity reagents [71]. However, unlike antibodies and other protein-based affinity reagents (including single-chain variable fragment antibodies, affibodies and designed ankyrin repeat proteins) [72–74] aptamers have unique advantages that make them powerful tools to develop artificial receptors. This provides an opportunity to integrate DNA devices with a wide variety of bioorganic compounds and to enlarge the detectability towards other biomolecules than nucleic acids, with exciting potentials in sensing and diagnostics applications [75-76].

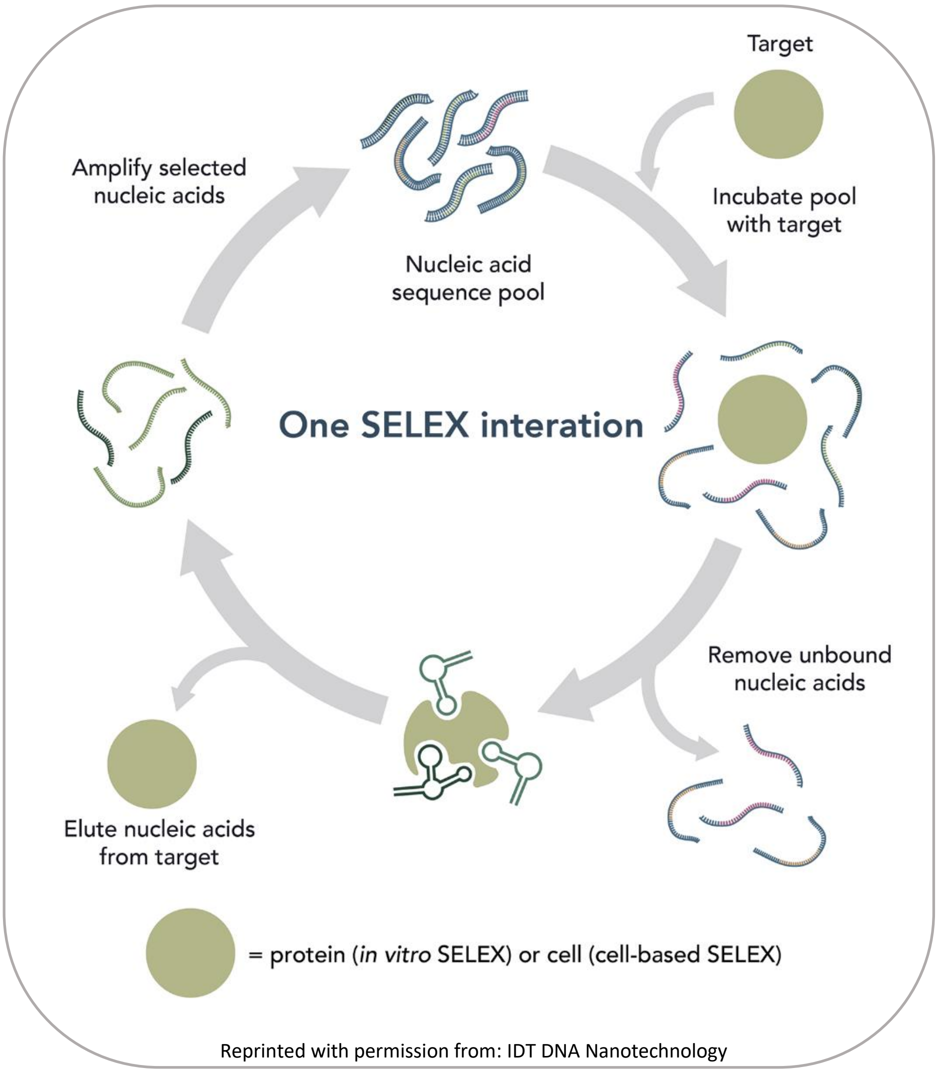

Reprinted with permission from: IDT DNA Nanotechnology

Figure5. A schematic representation of a typical SELEX cycle used to generate aptamers with affinity for an arbitrary target. A library of nucleic acid sequences is incubated with a target. Molecules that bind to the target are separated from the pool of non-functional sequences through the use of physical methods. Functional sequences are recovered and amplified. The whole process is repeated until the pool is dominated by sequences that exhibit the highest affinity to the target. Aptamers isolated by SELEX are analysed for

possible secondary structural motifs using computational programs that identify regions of the sequence that are capable of Watson–Crick base-pairing [104].

Another breakthrough in the development of functional DNA was achieved in 1994 with the discovery of the catalytic action exerted by DNA [77]. All catalytic DNA molecules, called DNAzymes (also described as DNA enzymes, deoxyribozymes or catalytic DNA elsewhere), are artificially obtained through the procedure of *in vitro* selection (SELEX) [78]. Herein, DNAzyme functions extend beyond the canonical Watson–Crick base pair recognition of complementary strands [79]. Indeed, nucleic acids can also participate in another kind of pairing known as "Hoogsteen base pairing". This kind of hydrogen bonding in a guanine-rich sequence DNA strand provides self-organized higher-order folded structures called *G-Quadruplex*. The complexity in space of G-quadruplexes depends on folding topologies, orientation of loops and capping structures. One sequence may form several conformations that exhibit different stabilities and are influenced by environmental conditions. In the simplest form, four guanosines assemble by hydrogen bonding between the Hoogsteen and Watson-Crick faces of adjacent guanosines. Two to four G-quartets can stack on each other to form aggregates, stabilized by the interaction of monovalent cations such as Na^+ and K^+ with the carbonyl oxygens of the guanosines [80]. G-quartets can also arise from two strands of DNA that assemble such that each strand contributes two guanosines to each quartet [81]. The G-quartet structure is very stable and highly symmetric. Changing the symmetry, the orientation of the complementary filaments and the configuration of the glycosidic portions of the quartets, it is possible to obtain a large pool of diversified structures (Figure6).

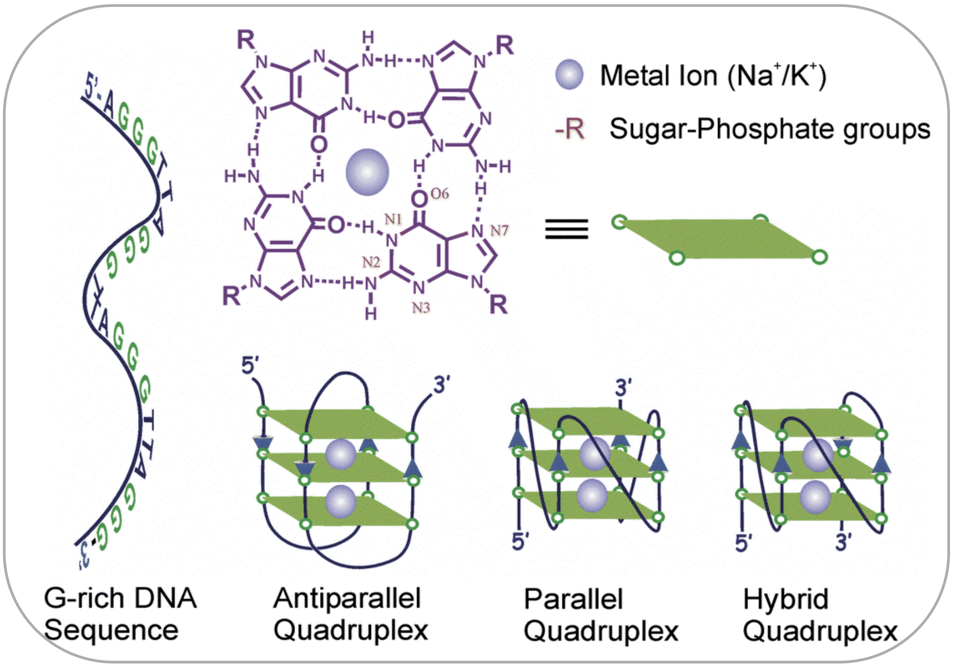

Reprinted with permission from: Bhasikuttan A.C. and Mohanty J., *Chem. Commun*, **51**, 7581-7597, .,(2015)

Figure6. Structures of the G-quartet/tetrad and the various common folding topologies found in G-quadruplexes.

In 2009, Shangguan and co-workers [82] noticed that the G-quadruplex structure was able to bind hemin and to mimic peroxidase activity. These so-called DNAzymes, exhibited a low catalytic activity when they assumed the configuration of tetramolecular structures with parallel strands or unimolecular antiparallel quadruplexes. On the contrary, the highest activity was observed for parallel or mixed intramolecular quadruplexes [83-84]. The most stable structure of G-quadruplex/hemin complex is the parallel form, due to π-π end-stacking bonds between external guanines and the porphyrin ring. On the contrary, the steric hindrance caused by loops in the antiparallel conformation reduced the strength of bond with hemin and consequently the peroxidase-like activity [85]. The topology of G-quadruplexes is also influenced by the nature of coordinated cation, the number of G-tetrads and the loop composition. The presence of cations is necessary for quadruplex formation. Early studies indicated that the potassium ion was crucial for quadruplex formation and catalytic activity [86]. The catalytic activity of

DNAzymes can be observed by an appropriate coupled detection reaction. In biological applications the commonly employed detection methods are based on the use of horseradish peroxidase (HRP) as catalyst of the oxidation reaction between the substrates ABTS (2,2′-azino-bis(3-ethylbenzthiazoline-6-sulphonic acid) or luminol with H_2O_2. The oxidation of ABTS in the presence of H_2O_2 generates a colored product, and changes in the absorption spectrum can be used to monitor the reaction progress [87]. The reaction of luminol with hydrogen peroxide produces chemiluminescence, for which the intensity serves as an analytical signal (Figure.7). A study performed by Wang and co-workers [88] showed that peroxidase activity was dependent on H_2O_2 but not on substrate concentration. In the reaction catalyzed by DNAzymes, the transfer of oxygen from H_2O_2 to Fe(III) in hemin is a rate-limiting step, as shown in Figure7.

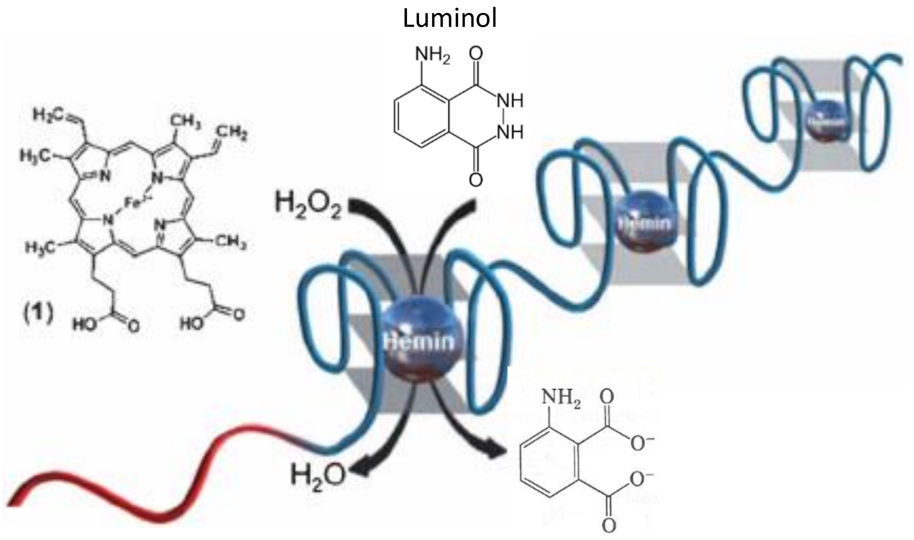

Figure7. Scheme of indicator reactions catalyzed by peroxidase-mimicking DNAzymes: the oxidation of luminol

DNAzymes with peroxidase-mimicking activity have great potential in bioanalytical chemistry, including nucleic acid probes with DNAzyme labels for the detection of specific DNA sequences in colorimetric or chemiluminescent assays and methods for enzymatic activity evaluation of telomerase or methyltransferase, which are potential targets in anticancer therapy, have also been reported [89-90].

1.4 CHEMICAL LUMINESCENCE SYSTEM

Chemical luminescence is a physical phenomenon caused by the production of light via a chemical reaction. Different subtypes are distinguished by the nature of stimulus able to trigger the reaction: chemiluminescence (CL) and bioluminescence (BL) are referred to the chemical production of light started by mixing the reagents, the latter exploiting enzymes and photoproteins isolated from living organisms [91]; electrogenerated chemiluminescence (ECL) is the luminescence generated by relaxation of exited state molecules produced during an electron-transfer reaction that occurs at the surface of an electrode [92]; thermo-chemiluminescence (TCL) is the emission of light produced by the thermally-induced decomposition of a molecule.

Some essential requirements so that a chemical reaction could produce light are [93]:

1. the sufficient exergonic character of reaction to populate an electronically excited (singlet) state. The free energy requirement can be calculated using the following equation:

$$-\Delta \mathrm{G} \geq \frac{hc}{\lambda_{ex}} = \frac{28600}{\lambda_{ex}}$$

Therefore, the energy required by a chemiluminescence reaction producing photons in the visible (400–750 nm) range is around 40–70 kcal mol^{-1}.

2. the accessibility on the reaction coordinates of this electronically excited state.

3. Photon emission from the excited state has to be a favorable energy release route. This means that either the product of the reaction has to be fluorescent or – if by energy transfer – an excited state can be populated (this energy transfer can occur intra- or intermolecularly).

The chemical luminescence quantum yield, is defined as the number of photons emitted per reacting molecule and can be calculated as:

$$\Phi_{CL} = \Phi_R \, \Phi_{ES} \, \Phi_F$$

where Φ_R reflects the chemical yield of the reaction, Φ_{ES} is the fraction of the product entering the excited state and Φ_F is the fluorescent quantum yield.

The oxidation of luminol is one of the oldest described CL reactions. Luminol can be considered a diprotic acid with pK_a values of 6 and 13, respectively. During the CL reaction under alkaline conditions in the presence of H_2O_2, luminol is oxidized to the corresponding radical anion in its excited state, which releases a photon while decaying to the ground state (Fig. 8). The light is emitted at 428 nm (blue light emission) with a relatively low quantum yield of 1% [94]. The reaction is usually catalyzed by horseradish peroxidase (HRP), commonly used as a label in immunometric assays, because of its signal amplification capability and high turnover number [95].

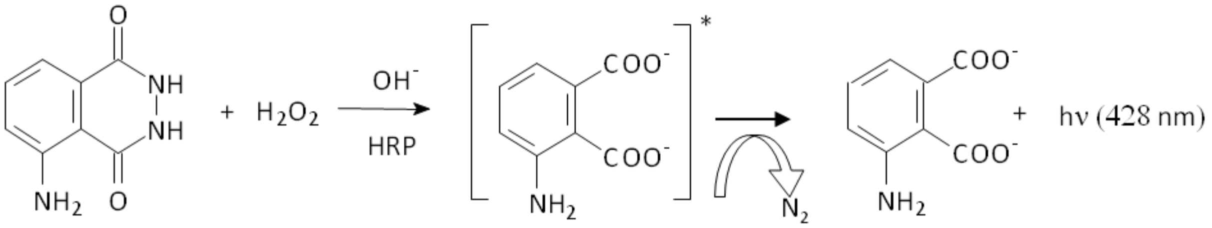

Figure8. HRP-catalyzed oxidation of luminol.

The possibility to use an enzyme like horseradish peroxidase (HRP) or alkaline phosphatase (AP) as a label allows to amplify the CL signal, since in the presence of an excess of CL substrate many product molecules are generated from one enzyme molecule [95]. Moreover, the achievement of a steady-state of the CL emission allows the standardization of the experimental conditions and quantitation of the labeled probe under investigation, since the steady-state light intensity is directly related to the enzyme activity. A way to improve the analytical performance of the HRP-catalyzed CL oxidation of luminol consists of the addition to the CL cocktail of some enhancers like p-iodophenol (PIP), 4- (1-imidazolyl)phenol, [96] and other p-phenol derivatives, [97] p-phenylphenol and sodium tetraphenylborate as synergistic enhancer, [98] or $K_3Fe(CN)_6$ as electron mediator [99]. These enhancers allow to amplify and stabilize the CL signal increasing the sensitivity of the analytical method [100].

The analytical interest of chemical luminescence detection techniques mainly arises from the possibility to produce photons with no need for photoexcitation, as for fluorescence-based techniques, thereby overcoming problems related to light scattering, background fluorescence or light source instability. Therefore, instrumentation for chemical luminescence measurements is in principle very simple, since no excitation source is required. In addition, when chemical luminescence detection is employed in conjunction with imaging detection systems, such as charge coupled device (CCD) or complementary metal-oxide semiconductor (CMOS) cameras, flexible configurations of the reading cell (e.g., the spatial distribution of microarray spots on a functionalized surface) are possible, provided that cross-talk phenomena are controlled. Finally, chemical luminescence detection showed wide dynamic ranges, thus facilitating analysis of samples with very different analyte concentrations. On the other hand, the main limit of these detection techniques is the potential interference of sample matrix on the chemical reaction, which can either enhance or inhibit the light producing reaction. These effects are by definition unpredictable and may lead to artefacts or spurious results. Furthermore, due to the high detectability of the chemical luminescence labels, non-specific binding must be carefully controlled to avoid high background signals and thus surfaces functionalization strategies are crucial for the success of the assay [101]. Another aspect that needs to be taken into account, especially when signal acquisition is performed in a flow regimen, is the dependence of kinetics of photons emission by the chemistry employed (ranging from flash- to glow-type). As the chemical luminescence signal is not stable over time, the light-emitting species are subjected to diffusion phenomena in solution, thus causing a loss in resolution [102].

1.5 PROPOSAL FOR THIS THESIS

The theme of this thesis is chemiluminescent DNAzyme based nanotechnology. In Chapter 2 a structure-switching aptasensor exploiting ATP-induced hemin-DNAzyme catalytic activity for generating a chemiluminescent signal was developed for its implementation on the PLEIADES chip. In Chapter 3 the development of split G-quadruplex DNAzyme platform for the chemiluminescent and quantitative detection of antibodies based on antibody-induced co-localization mechanism has been investigated. Chapter 4 differs from the previous chapters in that HRP enzyme has been employed. In particular, the enzyme has been encapsulated inside glutathione-stimuli responsive breakable silica nanocapsules. In this case, the innovative element consists in employing the light emission generated by chemiluminescent reaction as source of light for photodynamic therapy (PDT) *in vivo* application. In Chapter 5 a comparison of performance between optic and electrochemical biosensor was evaluated by photons and electron detection measurements. Upon outlining an update in recent achievements to boost analytical performance, amperometry and chemiluminescence (CL)-based biosensors were directly compared. In Chapter 6, a simple method for the real-time evaluation of the CL emission anisotropy based on a radial array of optical fibers, embedded in a poly (methyl methacrylate) semicylinder and coupled with a Charge-Coupled Device (CCD) camera through a suitable interface, was proposed, with the aim of providing new insights for efficient light collection in miniaturized chemiluminescence-based analytical devices.

REFERENCES

1 J D Watson and F H C Crick. Molecular structure of nucleic acids, Nature, 1953, 171, 737–738.

2 A Rutherford. Creation: The Origin of Life / The Future of Life. Penguin UK, 2013.

3 BBC History. Historic figures: Crick and Watson (1916-2004), 2014.

4 Nobelprize.org. The Nobel Prize in Physiology or Medicine 1962, 2014.

5 D Luo. The road from biology to materials. Materials Today, 6 (11):38–43, 2003.

6 T. J. Bandy, A. Brewer, J. R. Burns, G. Marth, T. N. Nguyen, E. Stul,Chem. Soc. Rev., 2011, 40, 138–148

7 B Alberts, A Johnson, J Lewis, M Raff, K Roberts, and P Walter. The Structure and Function of DNA. In Molecular Biology of the Cell. Garland Science, New York, 4th edition, 2002.

8 H Lodish, A Berk, and S L Zipursky. Section 4.1 Structure of Nucleic Acids. In Molecular Cell Biology. W. H. Freeman, New York, 4th edition, 2000

9 S L Price and A J Stone, Journal of Chemical Physics, 1987, 86:2859

10 B Tinland, A Pluen, J Sturm, and G Weill, Macromolecules, 1997, 30(19):5763–5765

11S B Smith, Y Cui, and C Bustamente, Science, 1996, 271:795–798

12 M Vologodskaia and A Vologodskii, Journal of molecular biology, 2002, 317(2):205–213

13 S Geggier and A Vologodskii., 2010, 107(35):15421–15426,

14 V I. Ivanov, L E Minchenkova, E E Minyat, and M D Schyolkina,1974, 87(4):817–833.

15 A Rich, A Nordheim, and A H Wang, 1984, 53:791–846

16 C. Mao, W. Sun, Z. Shen and N. C. Seeman, Nature, 1999, 397, 144–146.

17 A. P. Mills, F. C. Simmel, A. J. Turberfield, J. L. Neumann and B. Yurke, Nature, 2002, 406, 605–608.

18 Y. Krishnan and F. C. Simmel, Angew. Chem., Int. Ed., 2011, 50, 3124–3156

19 N. Hamaguchi, A. Ellington and M. Stanton, Anal. Biochem., 2001, 294, 126–131.

20. D. Selnihhin, S. M. Sparvath, S. Preus, V. Birkedal and E. S. Andersen, ACS Nano, 2018, 12, 5699–5708

21 B. Ding and N. C. Seeman, Science, 2006, 314, 1583–1585.

22 D. Woods, D. Doty, C. Myhrvold, J. Hui, F. Zhou, P. Yin and E. Winfree, Nature, 2019, 567, 366–372

23 Y. Amir, E. Ben-Ishay, D. Levner, S. Ittah, A. Abu-Horowitz and I. Bachelet, Nat. Nanotechnol., 2014, 9, 353–357.

24 N. D. Derr, B. S. Goodman, R. Jungmann, A. E. Leschziner, W. M. Shih and S. L. Reck-Peterson, Tug-of-War, Science, 2012, 338, 662–665.

25 J. J. Funke, P. Ketterer, C. Lieleg, S. Schunter, P. Korber and H. Dietz, Sci. Adv., 2016, 2, e1600974.

26 J. V. Le, Y. Luo, M. A. Darcy, C. R. Lucas, M. F. Goodwin, M. G. Poirier and C. E. Castro, ACS Nano, 2016, 10, 7073–7084.

27 A. J. Thubagere, W. Li, R. F. Johnson, Z. Chen, S. Doroudi, Y. L. Lee, G. Izatt, S. Wittman, N. Srinivas, D. Woods, E. Winfree and L. Qian, Science, 2017, 357, eaan6558.

28 D. Koirala, P. Shrestha, T. Emura, K. Hidaka, S. Mandal, M. Endo, H. Sugiyama and H. Mao, Angew. Chem., Int. Ed., 2014, 53, 8137–8141.

29 S. M. Douglas, I. Bachelet and G. M. Church, Science, 2012, 335, 831–834.

30 D. Y. Zhang and G. Seelig, Nat. Chem., 2011, 3,103–113.

31 F. C. Simmel, B. Yurke and H. R. Singh, Chem. Rev., 2019, 119, 6326–6369.

32 D. Y. Zhang and E. Winfree, J. Am. Chem. Soc., 2009, 131, 17303–17314

33 E. S. Andersen, M. Dong, M. M. Nielsen, K. Jahn, R. Subramani, W. Mamdouh, M. M. Golas, B. Sander, H. Stark, C. L. P. Oliveira, J. S. Pedersen, V. Birkedal, F. Besenbacher, K. V. Gothelf and J. Kjems, Nature, 2009, 459, 73–76.

34 W. B. Sherman and N. C. Seeman, Nano Lett., 2004, 4, 1203–1207.

35 J. Pan, F. Li, T. G. Cha, H. Chen and J. H. Choi, Curr. Opin. Biotechnol., 2015, 34, 56–64.

36 P. Zhan, S. Both, T. Weiss and N. Liu, Nano Lett., 2019, 19, 6385–6390.

37 S. Li, Q. Jiang, S. Liu, Y. Zhang, Y. Tian, C. Song, J. Wang, Y. Zou, G. J. Anderson, J. Y. Han, Y. Chang, Y. Liu, C. Zhang, L. Chen, G. Zhou, G. Nie, H. Yan, B. Ding and Y. Zhao, Nat. Biotechnol., 2018, 36, 258–264.

38 L. Zhou, A. E. Marras, C. M. Huang, C. E. Castro and H. J. Su, Small, 2018, 14, 1802580

39 F. Pu, C. Wang, D. Hu, Z. Huang, J. Ren, S. Wang and X. Qu, Mol. BioSyst., 2010, 6, 1928–1932

40 C. Zhou, X. Duan and N. Liu, Nat. Commun., 2015, 6, 8102.

41 Yi Lu and Juewen Liu, Current Opinion in Biotechnology,2006,17,580–588

42 M. DeLuca, Z. Shi, C. E. Castro and G. Arya, Nanoscale Horiz., 2020,5, 182-201

43 K. Vermeulen, D.R. Van Bockstaele, Z.N. Berneman, Cell Prolif, 2003, 36, pp. 131-149

44 M. Rossetti, A. Porchetta, Analytica Chimica Acta, 2018, 1012,30-41

45 J. Cherfils, M. Zeghou, Nat. Chem. Biol.,2011,7, pp. 493-495

46 J. Soboloff, M. Madesh, D.L.,Nat. Chem. Biol., 2011,7, pp. 488-492

47 A. Vallée-Bélisle, K.W., Curr. Opin. Struct. Biol., 2010,20, pp. 518-526

48 A.A. Lubin, K.W. Plaxco, Acc. Chem. Res., 2010, 43, pp. 496-505

49 K.W. Plaxco, H.T. Soh, Trends Biotechnol., 2011, 29, pp. 1-5

50 S. Slomovic, K. Pardee, J.J., Proc. Natl. Acad. Sci. Unit. States Am., 2015,112 pp. 14429-14435

51 H.-M. Meng, H. Liu, H. Kuai, R. Peng, L. Mo, X.-B., Chem. Soc. Rev., 2016, 45, pp. 2583-2602,

52T.J. Zwang, S. Hürlimann, M.G. Hill, J.K. Barton, J. Am. Chem. Soc., 138 (2016), pp. 15551-15554

53 F. Wang, C.-H. Lu, I. Willner, Chem. Rev., 2014, 114 pp. 2881-2941,

54 F. Wang, X. Liu, I. Willner, Angew. Chem. Int. Ed. Engl, 2015, 54 pp. 1098-1129,

55 S. Ranallo, M. Rossetti, K.W. Plaxco, A. ValléeBélisle, F. Ricci, Angew. Chem. Int. Ed., 2015, 54, pp. 13214-13218

56J.S. Swensen, Y. Xiao, B.S. Ferguson, A.A. Lubin, R.Y. Lai, A.J. Heeger, K. W. Plaxco, H.T. Soh, J. Am. Chem. Soc., 2009, 131, pp. 4262-4266

57 S. Modi, C. Nizak, S. Surana, S. Halder, Y. Krishnan, Nat. Nanotechnol., 2013, 8, pp. 459-467

58 X. Zhang, Y. Song, A. Shah, V. Nucleic Acids Res., 2013, 41 Article e152

59 A. Vallée-Bélisle, F. Ricci, K.W. Plaxco, Proc. Natl. Acad. Sci. USA, 2009, 106, pp. 13802-13807,

60 Y. Krishnan, F.C., Angew. Chem. Int. Ed. Engl, 2011, 50, pp. 3124-3156

61 M. Wang, Z. Mao, T.-S. Kang, C.-Y. Wong, J.-L. Mergny, C.-H. Leung, D.-L. Ma, Chem. Sci., 7 (2016), pp. 2516-2523

62 J. Shen, H. Wang, C. Li, Y. Zhao, X. Yu, X. Luo, Biosens. Bioelectron., 2017, 90, pp. 356-362

63 K.-H. Leung, H.-Z. He, B. He, H.-J. Zhong, S. Lin, Y.-T. Wang, D. L. Ma, C.-H., Chem. Sci., 2015, 6, pp. 2166-2171

64 P. Zou, Y. Liu, H. Wang, J. Wu, F. Zhu, H., Biosens.Bioelectron., 2016, 79, pp. 29-33,

65 T. Li, E. Wang, S. Dong, Anal. Chem., 2010, 82, pp. 1515-1520

66 Y. Li, X. Ji, W. Song, Y. Guo, Anal. Chim. Acta, 2013, 770, pp. 147-152,

67 A.L. Furst, M.J. Smith, MaB. Francis, J. Am. Chem. Soc., 2017, 139, pp. 12610-12616

68 C.L. Beisel, T.S. Bayer, K.G. Hoff, C.D. Smolke, Mol. Syst. Biol., 2008,4

69 J.S. Marvin, H.W. Hellinga, Nat. Struct. Biol., 8 (2001), pp. 795-798

70 R.R.F. Machinek, T.E. Ouldridge, N.E.C. Haley, J. Bath, A.J. Turberfield., N.Commun.,2014,5, p. 5324

71 D.Y. Zhang, E. Winfree, J. Am. Chem. Soc., 2009, 131, pp. 17303 17314

72L. Chen, J. Chao, X. Qu, H. Zhang, D. Zhu, S. Su, A. Aldalbahi, L. Wang, H. Pei, ACS Appl. Mater. Interfaces, 2017, 9, pp. 8014-8020

73 N. Wu, I. Willner, Nanoscale, 2016,1, pp. 1-7

74 S. Perrier, P. Bouilloud, G. de Oliveira Coelho, M. Henry, E. Peyrin, Biosens. Bioelectron., 2016, 82, pp. 155-161,

75 A. Desrosiers, A. Vallée-Bélisle, Nanomedicine, 2017, 12, pp. 175-179

76 Y. Tang, F. Long, C. Gu, C. Wang, S. Han, M. He, Anal. Chim. Acta, 2016, 933, pp. 182-188

77 SK. Silverman, Trends Biochem Sci., 2016;41(7):595-609

78 M. Hollenstein, Molecules, 2015;20, 20777-20804

79 T. Y. Nakama, D. Takezawa, M. Sasaki, M. Shionoya, J. Am. Chem. Soc. 2020, 142, 22, 10153–1016

80 Yang X.L., Sugiyama H., Ikeda S., Saito I., Wang A.H.J., Biophysical Journal, 1998, 75,1163–1171

81 W. Sundquist, A. Klug, Nature, 1989, 342, 825–829

82 X. Cheng, Xiangjun L.,Tao B., Cehui C., Dihua S., Biochemistry, 2009, 48, 7817-23

83 T. Bhattacharyya, P. Saha, J. Dash., ACS Omega 2018, 3 (2) , 2230-2241

84 P. Hanyong, Newbigging A.M., T. Jeffrey, D.X.C.L. Wenchan, Z. Hongquan, Anal. Chem., 2018, 90,1, 190-20

85 T. Chang, W. Li, Z. Ding, S. Cheng, K. Liang, X. Liu, T. Bing, D. Shangguan, Anal. Chem., 2017, 89, 8162-8169

86 J. Haojun, L. Yuqian, X. Tianshu, Q. Xiaojun, B. Feika, A. Qingjiang, Anal. Chem., 2016, 88, 10411-10418

87 X. Lu, Z. Zhaojuan, F. Mengli, T. Aijun, X. Yu, Bioconjugate Chem., 2016, 27, 621-627

Z. Wang, J. Zhao, J. Bao, Z. Dai, ACS Appl. Mater. Interfaces, 2016, 8, 827-833

89 F. T. Zhang, J. Nie, D. W. Zhang, J. T. Chen, Y. L. Zhou, X.X. Zhang Anal. Chemistry, 2014, 86, 9489-9495

90 J. Shen, Y. Li, H. Gu, F. Xia, X. Zuo ,Chem. Rev., 2014, 114, 7631-7677

91 A. Roda, M. Guardigli, Anal. Bioanal. Chem., 2012, 402, 69–76

92 L. Hu, G. Xu,) Chem. Soc. Rev., 2010,39, 3275–3304

93 Chemiluminescence and Bioluminescence: Past, Present and Future, Edited by Aldo Roda, Royal Society of Chemistry 2011, Published by the Royal Society of Chemistry

94 R. Creton, L.F. Jaffe, BioTechniques, 2001, 31, 1098-1105

95 A. Roda, P. Pasini, M. Guardigli, M. Baraldini, M. Musiani, M. Mirasoli M, J. Fresenius, Anal. Chem., 2000, 366, 752-759

96 Y. Dotsikas, Y.L. Loukas, Anal Chim Acta, 2004, 509, 103-109

97 Y. Dotsikas, Y.L. Loukas, Talanta , 2007, 71, 906-910

98 X.J. Luo, X.C Yang, Anal. Chim. Acta, 2003, 485, 57-62

99 R.S. Chouhan, K.V. Babu, M.A. Kumar, N.S. Neeta, M.S. Thakur, B.E.A. Rani, A. Pasha, N.G.K. Karanth, N.G. Karanth, Biosen Bioelectron, 2006, 21, 1264-1271

100 E. Marzocchi, S. Grilli, L. Della Ciana, L. Prodi, M. Mirasoli, A. Roda, Anal. Biochem., 2008, 377, 189–194

101 A. Wolter, R. Niessner, M. Seidel, Anal Chem, 2007, 79, 4529–4537

102 B.J. Cheek, A.B. Steel, M.P. Torres,Y.Y. Yu, H. YanG, Anal. Chem., 2001, 73, 5777–5783

103 M. De Luca, Z. Shi, C. E. Castro, G. Arya, Nanoscale Horiz., 2020,5, 182-201

104 M. Dunn, R. Jimenez, J. Chaput, Nat. Rev. Chem., 2017, 1, 0076

2

INTEGRATED CHEMILUMINESCENCE-BASED LAB-ON-CHIP FOR DETECTION OF LIFE MARKERS IN EXTRATERRESTRIAL ENVIRONMENTS

Reproduced from: "Integrated chemiluminescence-based lab-on-chip for detection of life markers in extra-terrestrial environments"
Augusto Nascetti, Mara Mirasoli, Elisa Marchegiani, Martina Zangheri, Francesca Costantini, Alessandro Porchetta, Lorenzo Iannascoli, Nicola Lovecchio, Domenico Caputo, Giampiero De Cesare, Simone Pirrotta, Aldo Roda
Biosensors and Bioelectronics, 2019,123, 195-203
Reproduced by permission of The Royal Society of Chemistry
https://www.sciencedirect.com/science/article/pii/S0956566318306651

2.1 INTRODUCTION

The search for organic compounds in the surface or sub-surface of planets, satellites or other small bodies is a major challenge in extra-terrestrial exploration. Up to date, space missions dedicated to the search for biosignatures of extant or extinct life mainly relied on pyrolytic extraction of volatile compounds and their detection by gas chromatography (GC) coupled with mass spectrometry (MS). However, pyrolysis-GC-MS mainly detects simple organic molecules (e.g., aminoacids, sugars, nucleobases, carboxylic acids) that can be present in space environments also as products of abiotic processes. In addition, only very recently some organic molecules could be detected and identified in exploration missions [1] . Unsuccessful previous analyses can be probably ascribed to targets decomposition caused by complex interactions between analytes and matrix components occurring at high volatilization temperatures for pyrolysis-GC-MS analysis, such as oxidation by perchlorates present on Mars surface [2]. In recent years, scientists have been turning towards gentler bioanalytical approaches based on immunoassays performed in microfluidic devices, such as the Life Marker Chip (LMC) [3], or microarrays, such as the Signs Of Life Detector (SOLID) [4]. A major advantage is the possibility to target biomolecules in a wide range of molecular sizes, from small organic molecules to biopolymers and even cells, thus expanding detection capabilities beyond low-to-mid-molecular-weight organic life markers. Adenosine 5′-triphosphate (ATP) is a good candidate as the target analyte, basing on the hypothesis that life developed on extraterrestrial environments would follow similar evolutionary principles as in Earth, given that the initial organics inventory, and in some cases the environments, were likely to have been similar [5]. ATP is an energy storage/transfer biomolecule, ubiquitous on Earth, that is considered a relevant marker of extant life, as it rapidly degrades in the absence of viable organisms due to the intrinsic instability of its high-energy bonds. The detection of life markers present at very low concentration requires highly sensitive techniques. Bioaffinity methods based on the use of antibodies as specific recognition elements can guarantee high sensitivity and selectivity and are suitable for their implementation into miniaturized biochips [6]. Although relatively high stability of antibodies to cosmic radiations has been reported [7], recently nucleic acid aptamers have been proposed as substitutes, taking advantage of their higher stability under harsh conditions [8]. Aptamers are single-stranded DNA or RNA oligonucleotides (generally 20–70 nucleobases) obtained by the systematic evolution of ligands by exponential enrichment (SELEX) procedure [9]. DNA aptamers are stable for many years under freeze-dried conditions, while in solution a denaturation-renaturation process (heating/cooling step) allows their regeneration in 30 min. In addition to being employed merely as antibody substitutes, aptamers can be exploited to produce nucleic acid-based molecular nanoswitches, suitable for real-time molecular sensing in complex environments and exploiting DNAzyme-mediated catalysis to reach high target detectability [10]. Enzyme-based assays are also worth being explored for life marker detection, as they are well established in clinical chemistry analyses and they would enable enlarging the suite of detectable molecules to low-molecular weight compounds, for which antibodies with high binding avidity are not easily obtained. Taking into account space payloads constraints, such as reduced mass, volume, and power consumption, extremely compact analytical instruments are required. In this context, lab-on-chip devices are extremely attractive for space missions [11]. However, the vast majority of the proposed lab-on-chip systems, including both commercial and research devices, can be referred as”chip-in-a-lab” instead [12], since operation of microfluidic chips requires bulky ancillary equipment such as fluidic pumps, high current power supplies, signal acquisition devices (microscopes, spectrometers, etc.). Furthermore, many systems, as e.g. the LMC and SOLID, rely on fluorescence detection methods that require complex optical systems including radiation sources, lenses and optical filters for the rejection of the excitation wavelength and the selection of the proper analytical signal. Chemiluminescence detection, in which the photon emitter is brought to its excited state by a chemical reaction, represents a valid alternative to fluorescence methods, eliminating the need to implement the photoexcitation system [13]. Additionally, chemiluminescence detection has been proved to provide superior detectability, as several sources of background and interference found in fluorescence-based assays are avoided, such as light scattering and fluorescent emission from cofactors or sample compounds, that decrease the signal-to-noise ratio and require mitigation [14]. In this work, we describe the development of the Planetary Life Explorer with Integrated Analytical Detection and Embedded Sensors (PLEIADES) chip, that integrates on a single glass substrate: 1) an autonomous microfluidic network in which samples and reagents are handled exploiting capillary forces, thus eliminating the need for external pumping units; 2) a set of functionalized detection sites where antibody or aptamer-based binding assays based on chemiluminescent detection will be carried out; 3) an array of thin-film hydrogenated amorphous silicon (a-Si:H) photosensors for the detection of the chemiluminescent signal [15]. The PLEIADES chip is interfaced with a custom low-noise front-end electronics for the biasing of the photodiode array and the readout of the photocurrents. The front-end electronics provides a digital interface with a computer where a custom Java software performs data preprocessing, visualization, analysis and storage. To investigate the possibility to detect ATP by means of different luminescent bioassays, we optimized and applied on-chip a bioluminescence luciferase-based assay, a chemiluminescence competitive enzyme immunoassays and an aptamer-based DNA nanoswitch assay.

2.2 MATERIALS AND METHODS

2.2.1 Reagents and materials

Adenosine 5′-triphosphate (ATP) disodium salt hydrate (99%), guanosine 5′-triphosphate (GTP), cytidine 5′-triphosphate (CTP), uridine 5′-triphosphate (UTP), hemin from bovine (≥ 90%), trizma hydrochloride, luminol sodium salt, anti-rabbit IgG conjugated to horseradish peroxidase (HRP-IgG), sodium dodecyl sulfate (SDS), formamide, dithiothreitol (DTT), Alconox, bovine serum albumin (BSA), n-propyldimethylchlorosilane, 3-aminopropyldimethylethoxysilane, N-[ε-maleimidocaproyloxy]sulfosuccinimide ester (sulfo-EMCS), and Silane-Prep slides were purchased from Sigma-Aldrich (St Louis, MO). Antibody anti-ATP produced in rabbit and ATP conjugated to ovalbumin (OVA-ATP) were bought from Cloud-Clone Corp (Katy, TX). Chemiluminescent substrate for HRP Supersignal ELISA Femto was purchased from Thermo Fisher Scientific (Waltham, MA). Sodium hydroxide and potassium dihydrogen phosphate were purchased from Carlo Erba Reagents (Milano, Italy). Hydrogen peroxide (30%) was purchased from VWR International (Radnor, PA). DNA sequences purified via high-performance liquid chromatography (HPLC) were purchased from Integrated DNA Technologies (IDT, Skokie, IL). All reagent-grade chemicals were used without further purification. Ultrapure water from Merckmillipore (Billerica, MA) source was used throughout the experiments. Samples simulating an extract from an assumed soil sample were prepared by spiking with known ATP amounts a water:methanol (80:20, v/v) solution containing 1.5 mg mL−1 Polysorbate 80. All reagents employed for poly 2-(hydroxylethyl methacrylate) (PHEMA) were purchased from Aldrich Chemicals. 2-Hydroxylethil methacrylate (HEMA) was distilled prior to use, whereas the other chemicals were used without further purification. 2-Bromo-2-methyl-propionic acid 3-trichlorosylanyl-propyl ester (BMPTS) was synthesized following a reported procedure (Costantini et al., 2016). Acetone and ethanol 96% (analytical reagent grade) were used without further purification, while toluene was distilled over sodium. The synthesis of the poly(2-hydroxyethyl methacrylate) was performed useing a previously reported procedure (Costantini et al., 2015, Costantini et al., 2016). The CellTiter-Glo Luminescent Cell Viability Assay was purchased from Promega.

2.2.2 Reference optical instrumentation

Absorbance measurements were performed using a Varian Cary 50Scan UV–Vis spectrophotometer. For optimizing the DNA nanoswitch protocol, chemiluminescence measurements in microtiter plate format were carried out using a Thermo Scientific Luminoskan Ascent luminometer (Thermo Fisher Scientific). As a reference instrumentation, an ultrasensitive CCD camera (MZ-2PRO from MagZero, Pordenone, Italy), equipped with a thermoelectrically cooled monochrome Sony ICX285 sensor, coupled with an objective and inserted into a light-tight dark box to avoid interference from ambient light, was used to image the chemiluminescence signal from the PLEIADES chip.

2.3. PLEIADES CHIP

The core of the proposed analytical platform is an innovative lab-on-chip device that integrates on a single glass substrate the microfluidic network for the implementation of the analytical protocols, the functionalized surface for the immobilization of the target molecules and an array of thin-film a-Si:H photodiodes for the transduction of the chemiluminescent signal into an electrical signal. The structure of the chip is reported in Figure1.

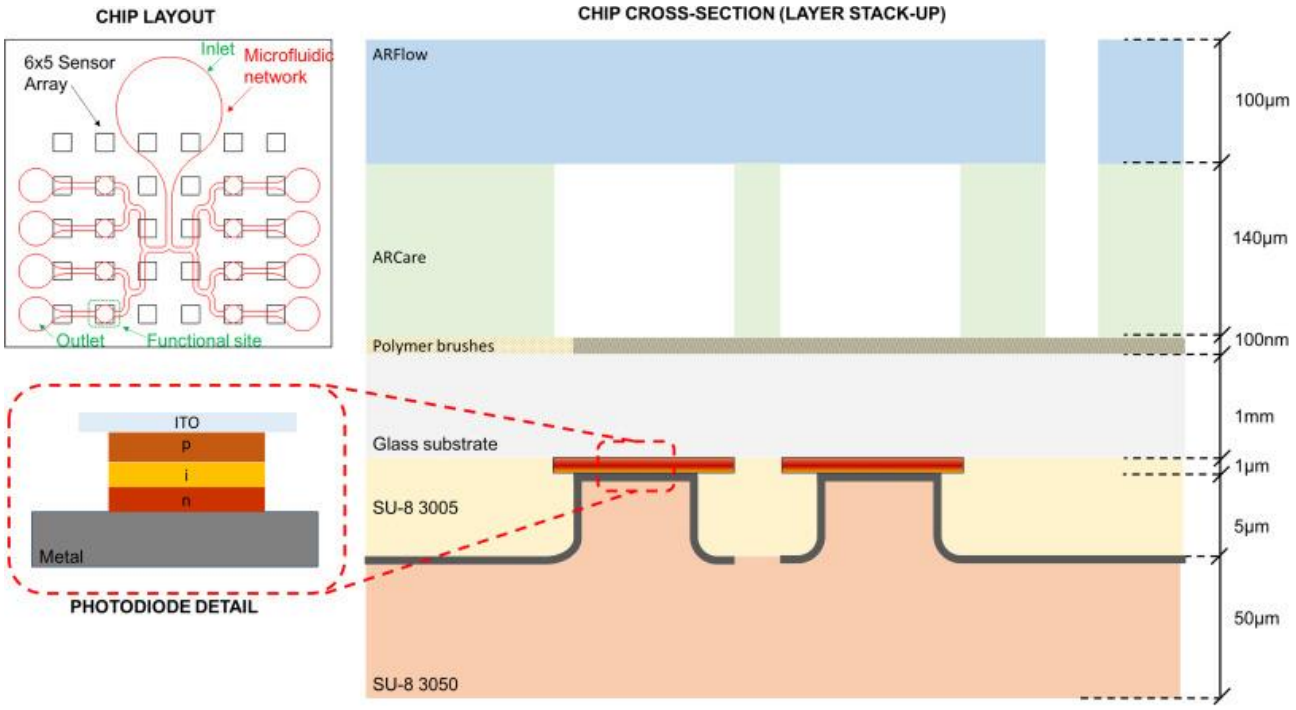

Figure1. Schematic view of the PLEIADES chip. Top-left: simplified chip layout view showing the position of the 30 photodiodes (squares) and the shape of the microfluidic network with one inlet and 8 identical branches, each having a functional site and an outlet. Right: cross-section of the chip (not to scale). The thickness of each layer is reported on the right. Bottom-left: detail of the thin-film a-Si:H p-i-n photodiode with transparent contact at the glass side to measure the CL signal coming from the opposite side of the glass.

The substrate is a soda-lime glass. The microfluidic network is fabricated using a stack of Pressure Sensitive Adhesives (PSA) from Adhesive Research (ARFlow 93049, ARCare 90106). The microfluidic network has been cut in the PSA layers by means of a cutting plotter (Silhouette Curio). The glass surface functionalization for the final device has been achieved using a layer of PHEMA polymer brushes grown on one side of the glass substrate. The thin-film photodiodes are stacked structures of p-doped, intrinsic and n-doped hydrogenated amorphous silicon (a-Si:H) with transparent indium tin oxide (ITO) bottom contact and metallic (Cr-Al-Cr)-stack as top contact. The a-Si:H layers have been deposited by Plasma Enhanced Chemical Vapor Deposition (PECVD) using a three-chamber ultra-high-vacuum system (Glasstech Solar Incorporation, Denver, Colorado). The 180 nm-thick ITO layer was deposited by a magnetron sputtering physical deposition system from Materials Research Corporation (Orangeburg, NY, USA). The top metal electrode is a three-metal layer stack (30 nm-thick Cr, 150 nm-thick Al, 30 nm-thick Cr) deposited using the same sputtering system. SU-8 (SU-8 305 and SU-8 3050 from Micro Resist Technology GmbH) is used both as interlayer dielectric and final passivation layer. The fabrication process has been optimized to ensure the compatibility among all the process steps. The high-level sequence of processing steps is the following: 1) fabrication of the array of thin-film photodiodes on one side of the glass substrate (Costantini et al., 2015); 2) growth of the PHEMA polymer brushes layer on the other side of the glass substrate; 3) mounting of the PSA microfluidic network on the PHEMA side of the glass substrate. Preliminary characterization of the lab-on-chip device has been performed by testing all of its components. Current-voltage characterization and spectral responsivity measurements were performed on the a-Si:H photodiodes using a setup based on a Keithley 236 Source Measure Unit (SMU), a tungsten light source, a monochromator (model Spex 340E from Jobin-Yvon), an UV-enhanced crystalline silicon diode (model DR 2550–2BNC from Hamamatsu) used as reference, a beam-splitter and focusing optics (from Melles-Griot). Several versions of the microfluidic network have been designed and tested to implement all the features needed for the execution of multi-step analytical protocols with good reproducibility and reliability. The tests have been performed by filling the network with colored buffer solutions that mimic the real solutions of the actual experimental protocols, and by filming the capillary filling of the network with a camera.

2.4. FRONT-END ELECTRONICS

The front-end electronics (Figure2) enables the simultaneous acquisition of all the on-chip sensors of the PLEIADES chip. The 32-channel front-end electronic board has been developed for this project starting from a previous 8-channel design [16]. The board includes the following sections: 1) a card edge connector (Samtec MB1–150-S-02-SL) as physical interface with the lab-on-chip; 2) a low-noise analog section including the current readout circuit (DDC118 from Texas Instruments) and the bias voltage supply circuit (AD5665 digital-to-analog converter from Analog Devices with LM7321 op-amp in buffer configuration from Texas Instruments) for the operation of the array and the digitization of the acquired signals; 3) a digital section (PIC18F4550 from Microchip) for timing and control of the analog part and for the interfacing (Universal Serial Bus, USB) with a computer. The front-end electronics is enclosed in a light-tight 5-mm thick aluminum box to ensure shielding from electromagnetic interferences (EMI) and from ambient light. A custom Java Graphical User Interface (GUI) has been developed to access all the board functionalities (including calibration and experimental protocol execution) and for real-time data pre-processing, visualization, statistical analysis and storage (Figure2). Figure2 also shows the complete PLEIADES system.

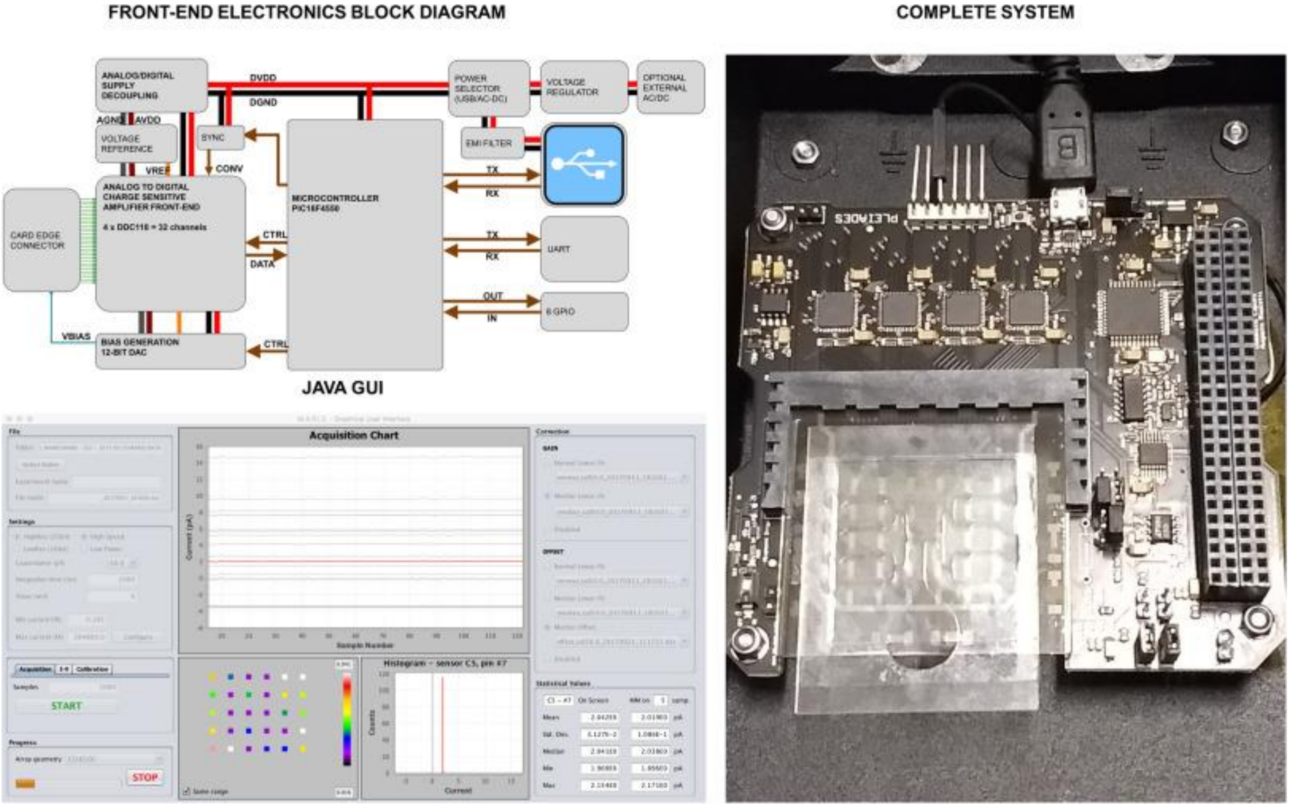

Figure2. Top-left: block diagram of the electronic front-end showing its main components and connections. Bottom-left: screenshot of the Java Graphical User Interface acquired during a test experiment. Right: picture of the whole system inside the black metallic shielding box with the PLEAIDES chip attached to the card edge-connector. The PLEIADES front-end board has PC-104 format and has been designed according to electronics reliability guidelines.

2.5. BIOASSAYS

2.5.1. Competitive Immunoassay

Once the PHEMA polymer brushes layer had grown on the glass substrate, 1 μL-spots of OVA-ATP (0.01 mg mL−1 in 50 mM borate buffer, pH 9.6, containing 0.1% (v/v) glycerol) were deposited onto the activated glass surface and incubated for 1 h at room temperature. After rinsing the chip with abundant PBS and drying with nitrogen flow, the top liner of the ARcare layer was removed and the chip was sealed with the ARFlow layer. The microfluidic network was then filled with a solution of blocking buffer (10 mM HEPES, 5 mM KCl, 120 mM NaCl, 10 mM CaCl2, pH 7, 2% BSA), and incubated for 2 h before rinsing with ultrapure water. The channels were then emptied using a cellulose pad (Whatman CF7, Whatman plc, Maidstone, UK) at the outlets and, if needed, also at the inlet. At this point the chip was ready to be stored at 4 °C prior to the use. For performing the assay, the double-sided PSA layer had to be mounted on the glass substrate on the opposite side with respect to the photosensor array taking care to leave accessible the microfluidic network for the injection of sample and reagents. For starting the immunoassay, a solution containing the sample and the anti-ATP antibody diluted 1:500 (v/v) in PBS was injected at the eight inlets and incubated for 30 min. After a washing step performed as the one after saturation, a solution containing HRP-IgG diluted 1:2000 (v/v) in PBS was loaded (30 min of incubation). After rinsing with PBS to remove unbound HRP-IgG, the cellulose pad was removed, and the fluidic channels were filled with Super Signal ELISA Femto substrate for HRP. The detection of the chemiluminescence signal was performed by measuring the photocurrents of the on-chip sensors after enclosing the whole system into a dark box equipped with a CCD camera, for monitoring the signal with the a-Si:H photosensors and the CCD simultaneously. Calibration curves were generated in a concentration range comprised between 10 nM and 20 μM ATP. Each point of the calibration curve corresponds to the plateau value of photocurrent measured during the entire luminescent reaction kinetics averaged over three independent measurements. The reported limits of detection (LOD) have been calculated as the ATP concentration whose signal corresponds to three times the standard deviation of the blank signal, which is measured in the absence of the target analyte.

2.5.2. DNA Nanoswitch

The oligonucleotides were used as provided and diluted in pH 7.5, 50 mM of phosphate buffer solution to give stock solutions of 100 μM. The sequences of the DNA-Nanoswitches regulated by ATP are as follows:

Switch #1: 5′-*ACCTGGGGGAGTAT*AACCTGCGGAGGAAGGT ATTGGGT GGGTTGGGTGGGT-3′

Switch #2: 5′-*ACCTGGGGGAGTAT*AACCCTGCGGAGGAAGGT TTTGGGT GGGTTGGGTGGGT-3′

Switch#3:5′-*ACCTGGGGGAGTAT*CCAACCCTGCGGAGGAAGGT TTTGGGTGGGTTGGGTGGGT-3′

Control G-quadruplex: 5′-GGGTGGGTTGGGTGGGT-3′

Control ATP aptamer: 5′-ACCTGGGGGAGTATTGCGGAGGAAGGT –3′

In the sequences above the underlined bases represent the stem portion of the "non-binding" state, while the italic bases represent the ATP recognition element and the stem of the "bound" state. The DNA sequence also contains a 5′ linker with a terminal SH group, used for grafting the nanoswitch to the glass surface of PLEIADES chip through covalent bonding. Thiol-modified DNA nanoswitch #3 was immobilized on glass following a published procedure [17]. Upon cleaning with 1% Alconox (w/v) in deionized water, silanized microscope glass slides were treated with 1 mM sulfo-NHS in 0.1 M sodium phosphate buffer, pH 7.5, for 40 min at room temperature, then washed with sodium phosphate buffer and dried in on nitrogen flow. Thiol-modified DNA sequences, which were protected with a disulfide bond by the vendor, were reduced to the sulfhydryl active form by incubating the sample with 0.1 M DTT in sodium phosphate buffer, pH 8.4, for 1 h at room temperature. Then, 1 μL of the probe was pipetted onto modified substrates and allowed to incubate for 2 h at room temperature in a humid chamber. Finally, the glass surface was treated with a prehybridization buffer (0.1% SDS, 0.1 mg mL−1 BSA) for 1 h at 42 °C to prevent nonspecific adsorption. After washing and drying under nitrogen, the glass slides were stored at 4 °C until use. For performing the assay, the glass slide was coupled with the PSA microfluidic network and then integrated with the photosensors array. The assay was started by injecting the sample which contains ATP; upon 2 h incubation at room temperature and emptying the channels using adsorbent cellulose pad, hemin was added and incubated for 1 h at room temperature to form the hemin/G-quadruplex structures. Finally, after a washing step, a solution containing luminol and hydrogen peroxide was used for filling the channels and the chemiluminescence signals were acquired using the configuration described for the competitive immunoassay.

2.5.3. Bioluminescence Luciferase Assay

Disposable multiwell cartridges with integrated a-Si:H photosensors were obtained by coupling with the glass support a 10-mm-thick black PDMS unit bearing holes aligned with the photosensors array, as previously described [18]. In this configuration each hole represents a microwell in which the bioluminescence reaction occurs, while the corresponding photosensor monitors the photons emission. The assay was started by depositing in each microwell 5 μL of the solution containing ATP (calibration curve was generated into the concentration range 1 μM–10 nM) and then an equal volume of CellTiter-Glo® Reagent was added. The obtained mixture was incubated 10 min at room temperature. After enclosing the integrated multiwell cartridge into a dark box (also equipped with a CCD camera for reference parallel measurements), the luminescent signal was monitored with the a-Si:H photosensors, through consecutive acquisitions for 10 min. Each point of the calibration curve corresponds to the plateau value of photocurrent measured during the entire luminescent reaction kinetics averaged over three independent measurements. The reported LOD has been calculated as the ATP concentration whose signal corresponds to three times the standard deviation of the blank signal, which is the signal measured when the BL cocktail was poured in a well without the analyte.

2.6 RESULTS AND DISCUSSION

2.6.1. PLEIADES Chip Design

The PLEIADES lab-on-chip includes a set of 30 photodiodes arranged in 5 rows of 6 elements each. Each photodiode is 2 × 2 mm2 and the pitch of the array is 5 mm in both directions. The microfluidic network has been designed according to the following requirements: 1) multiple samples should be analyzed in parallel on the same chip: different samples must therefore be loaded in correspondence of different sensors and must not interact with each other; 2) washing buffer and reagents should be flowed on each functional site; in particular, fresh CL reagents should arrive on each functional site (i.e. the CL reagents that flowed on the site where a given sample was loaded should not flow on the sites where other samples have been loaded: this is to prevent the depletion of the CL reagents and the consequent change in the signal intensity); 3) the microfluidic network should operate by autonomous capillary flow without the need of external pumping devices. The requirements listed above have been met by a capillary network having a single inlet followed by successive splitting channels leading to eight identical branches each of them with a reaction site and an outlet pad. In this case only eight out of the thirty available photodiodes are used to monitor the reaction sites; the remaining sensors were used to monitor the residual background radiation, if any, and the background spontaneous luminescence of the chemiluminescence reagents, to define the zero-level of the analytical signal. The microfluidic network described above is cut in the double-sided PSA layer (ARCare 90106) and is sealed with the single-sided PSA (ARFlow 93049).

2.6.2. PLEIADES Chip Operation

The life-cycle of the proposed lab-on-chip device can be divided in three main phases: the fabrication phase, the preparation phase and the operation phase. Referring to the cycle of a planetary exploration mission, the first two steps would be made on ground in the lab prior to the launch into space, while the last one would be executed once landed on the target body. These aspects have been considered when defining the protocols reported in the following paragraphs. The fabrication phase includes the fabrication of the photodiode array, the functionalization of the glass surface (growth of the PHEMA polymer brushes layer or of the aminosilane film) and the preparation of the PSA microfluidic layers with the desktop cutting plotter. This phase ends with the mounting of the double-sided PSA layer on the glass substrate on the opposite side with respect to the photosensor array. At this point the top protective liner is left in place and the microfluidic network remains accessible for the next phase. Regardless of the type of implemented assay, the preparation phase consists of immobilization of the bio-specific recognition molecules at the functional sites defined in the microfluidic network aligned with the photodiode array. The biofunctionalized chip can be stored at 4 °C prior to use. The operation phase comprises the addition and incubation of the sample and the addition and incubation of suitable reagents; it can include washing steps depending on the protocol involved. Up to eight different samples can be loaded in the network by pipetting 1 μL of each sample at the eight outlets of the microfluidic network. The sample moves backwards inside the microfluidic channels by autonomous capillary flow, then stops just after having filled the functional site that is present on each of the eight branches of the network. Labeled reagents (HRP-IgG or hemin) are loaded employing the same procedure. Although this step could be performed by inserting the solution at the inlet of the microfluidic network, the selected procedure implies a lower consumption of the labeled reagents and limits the risk of non-specific adsorption along the microfluidic network that would lead to disturbing non-specific background signals. All washings are performed though a rinsing flow, achieved by approaching a piece of adsorbent cellulose pad at the eight outlets of the microfluidic network and repeatedly filling the inlet reservoir with rinsing solution. Chemiluminescence reagents are loaded at the common inlet of the chip and the photon emission is concurrently detected by measuring the photocurrents of the on-chip sensors. The fabrication, preparation and operation protocol described above highlights some of the advantages of the proposed lab-on-chip device, such as high system robustness, limited need for ancillary hardware and reduced power consumption. The on-chip photosensors allow a perfect optical coupling and higher light collection angle with respect to off-chip detectors, such as CCDs. This implies a more efficient photons collection and thus lower LOD values. In addition, the room-temperature bonding procedure for the attachment of the PSA microfluidic network significantly simplifies the immobilization phase that is performed prior to the sealing of the chip. This fact implies, for example, the possibility to immobilize different biospecific probes in different sites to implement multi-parametric assays. Moreover, the use of PHEMA brushes as anchor for the biospecific probes, e.g., OVA-ATP, increases the specific surface available for the biorecognition event in the functional sites leading to an increase of the system sensitivity [19].

2.6.3. PLEIADES Chip Characterization

For the preliminary experimental validation of the proposed system, it was decided to fabricate the lab-on-chip using two different glass substrates: one hosting the a-Si:H photodiodes and the other with the functionalized surface and the microfluidic network. No changes have been done in the fabrication protocol, which is therefore identical to that used to produce the monolithic exemplars of the lab-on-chip. This choice was taken to focus on the analytical performances and reduce the number of variables that may affect the results. In particular, with the abovementioned approach, the same array of photodiodes has been used throughout an entire series of experiments making the achieved results directly comparable to each other. To ensure optimal optical coupling an optical index matching oil was used between the two glass substrates. This technique proved to deliver results that closely match those achieved with monolithic devices. The results of the preliminary characterization of the sensors showed dark-current density around 10−10 A/cm2 measured at 10 mV reverse-bias voltage and responsivity values around 250 mA/W at 465 nm with the same bias level. The overall system noise has been measured in the practical operation conditions sampling the current of the photodiode in dark conditions before the last step of the protocol, namely before the pipetting of the chemiluminescence reagents at the microfluidic inlet. An average noise current level of 50 fA has been achieved working with a full-scale signal range of 1 nA and a data rate of 5 samples/s. After the preliminary system characterization, several experiments have been performed as reported in the next paragraphs.

2.6.4. Competitive Immunoassay for ATP Detection

Exploiting the PLEIADES chip, we developed an indirect competitive ELISA method for the detection of ATP, based on the competition of ATP present in the sample and ATP conjugated to ovalbumin immobilized into the microchannel for binding anti-ATP primary antibody. The detection was performed using a secondary HRP-labeled antibody and adding the proper CL substrate. All the experimental parameters, including reagents composition and incubation times and conditions have been optimized. A typical calibration curve is reported in Figure3B, while FigureS1 of Supplementary material reports the signals obtained for different concentrations of ATP in a range comprised between 0.3 nM and 20 μM. From these data, a limit of detection of 60 nM was found, confirming the data obtained using an ultrasensitive cooled CCD camera used as a reference detector. This detectability is comparable with that obtained employing a commercial bioluminescence luciferase-based assay.

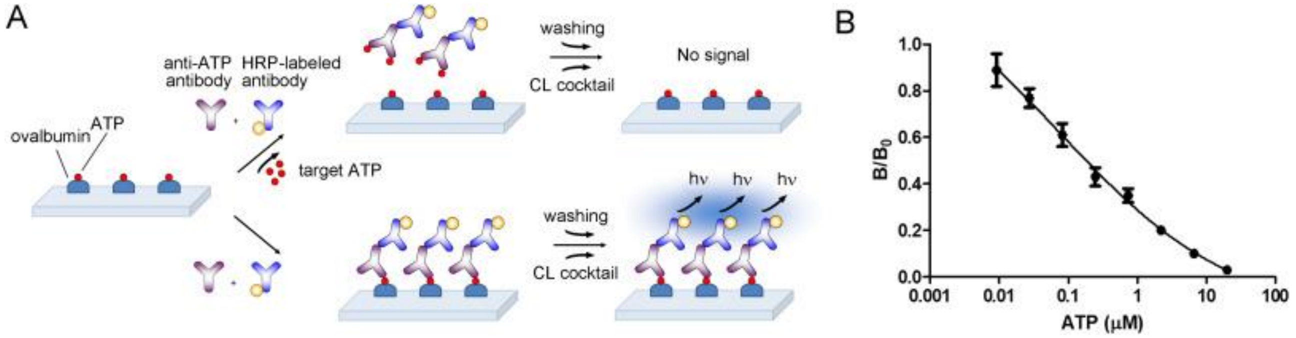

Figure3. (A) Scheme of the competitive immunoassay: top scheme represents the analysis of a sample containing a high amount of ATP, while bottom scheme represents the analysis of a sample containing no ATP; (B) Calibration curve.

As mentioned above, the relatively high stability of free and grafted antibodies exposed to cosmic rays simulating the conditions of a mission to Mars has been assessed [20], provided that appropriate design features (e.g. a surface density of antibodies much larger than the expected proton fluency across the chip) are adopted. However, ELISA-based methods employ enzyme labels, that pose additional conservation issues, including the requirement for low temperature storage conditions (typically 2–8 °C) and a limited shelf life. Several additives can be added to the storing solution to significantly increase long-term enzymes stability [21] and, as an alternative, novel artificial catalytic systems could be used for replacing traditional enzymes, such as DNAzymes. For example, the recently proposed heme synthetic proteins, named mimochromes, can mimic the peroxidase activity with improved stability and efficiency [21] and they will be explored as a high potential tool to be exploited as label in ELISA-based method for extra-terrestrial applications.

2.6.5. DNA Nanoswitch

A structure-switching aptasensor exploiting ATP-induced hemin-DNAzyme catalytic activity [22] for generating a chemiluminescent signal was developed for its implementation on the PLEIADES chip. The assay principle, shown in Fig. 4a, is based on a stem-loop DNA-nanoswitch that can adopt two exclusive conformations: “non-binding conformation” containing a stem domain and a “binding-competent” conformation containing a duplex stem (blue stem, Figure4a) recognized by the specific target analyte ATP. The binding of ATP pushes the conformational equilibrium towards the latter “bound” state to allow the hemin/G-quadruplex structuring. The incorporation of hemin into the resulting G-quadruplex ATP-nanoswitch aptamer complex yields an active HRP-mimicking DNAzyme, which generates a chemiluminescence signal in the presence of H2O2/luminol proportional to ATP concentration.

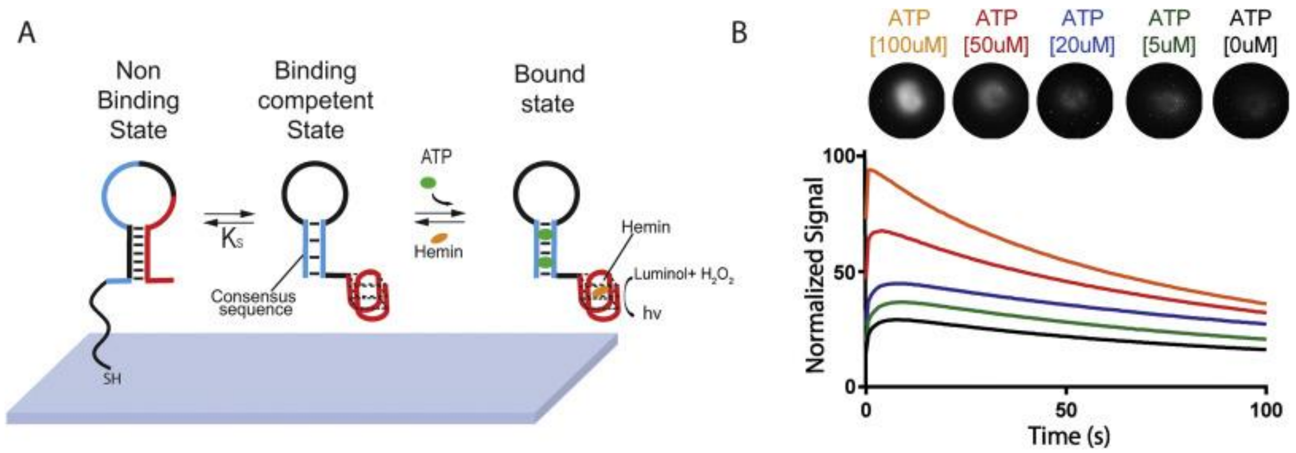

Figure4. (A) ATP-regulated DNA-nanoswitches coexist in two mutually exclusive stem-loop conformations, i.e. “Non-Binding” and “Binding-competent”. The binding of ATP pushes this conformational equilibrium towards the “Bound” state, thus triggering the hemin/G-quadruplex structuring. (B) Chemiluminescence nanoswitch #3 spectra generated by the hemin/G-quadruplex aptamer ATP complex, in the presence of H2O2/luminol and different concentrations of ATP. As the concentration of ATP is elevated, the

chemiluminescence is intensified, consistent with the higher content of the assembled DNAzyme G-quadruplex structure.

We designed three variants of ATP-regulated DNA-nanoswitches, each having the same binding domain for ATP with different "binding-competent" state stability. Control G-quadruplex sequence was employed to predict the signal/noise ratio of G-quadruplex structure/hemin, while control ATP aptamer sequence was employed to investigate non-specific interactions between ATP aptamer and hemin, eventually caused by G-quadruplex ATP aptamer structure. Firstly, a characterization of the DNA-nanoswitches was performed in solution in a conventional microtiter plate format. We evaluated the different DNA-nanoswitches affinity, producing chemiluminescence binding curves in the presence of increasing ATP concentrations. We found that DNA-nanoswitch # 3 displayed the highest signal intensity and affinity, as shown in Fig. 5a. We therefore selected switch #3 to further characterize the kinetics of the system. We observed an increase in activation with increasing ATP, with a signal increase of 160% observed for 100 μM ATP, consistent with the higher content of the assembled DNAzyme G-quadruplex structure (Fig. 5b). In contrast, the DNAzyme remains inactive when challenged with other non-specific targets, such as 100 μM CTP, GTP, and UTP (Figure 5c).

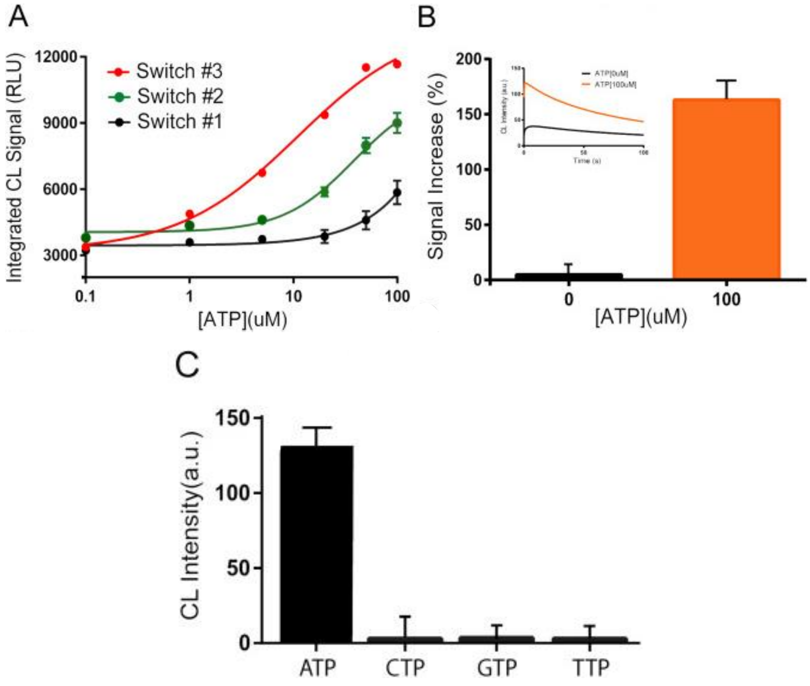

Figure5. (A) chemiluminescence binding curves of DNA-nanoswitches variants (#1, #2, #3) in the presence of increasing ATP concentrations. (B) For nanoswitch #3 we observed an increase in activation of 160%. (C) The DNAzyme remains inactive when challenged with other non-specific targets. Incubation with 100 μM of different nucleoside triphosphates, for example CTP, GTP, TTP, does not produce any significant signal increase.

Subsequently, the DNA-nanoswitch #3 was immobilized onto the PLEIADES chip for performing the on-chip assay. Following a published procedure [23], an inhomogeneous aminosilane film was produced on glass, followed by grafting by a maleimide-terminated crosslinker to provide a reactive site for the thiol-modified DNA covalent attachment. We employed this protocol, as it was reported to provide the best compromise in terms of immobilized DNA probe density, still avoiding excessive steric hindrance that would prevent proper DNA folding. As shown in Figure 4b, we observed an increase in activation with increasing ATP and an EC50 (the effector concentration at which 50% activation is observed) of 5 ± 0.8 μM (Fig. 4b, red line), consistent with the dissociation constant (6 ± 3 μM) reported for the ATP binding 27-mer aptamer employed in this work [24]. The present study has demonstrated that G-quadruplex DNA-nanoswitches can recognize different ATP concentrations and turn into catalytically active DNAzymes that generate chemiluminescence in the presence of H2O2/luminol. Specifically, nanoswitch #3 can be used as a potential biosensor to detect the life marker ATP through DNAzyme-like catalytic activity. In the future, to reach lower limits of detection, a target recycling-induced amplification mechanism will be explored [25].

2.6.6. Bioluminescence Luciferase Assay

Since the mid-1960s bioluminescent luciferase/luciferin-based assay was widely exploited thanks to its high sensitivity, selectivity, rapidity (results are obtained in less than 15 min) and relative ease of application. The assay uses firefly luciferase to catalyze the following luciferin oxidation reaction:

ATP (Mg2+) + d-Luciferin + O2 → Oxyluciferin + AMP + PPi + CO2 + *hν* (560 nm)

When ATP is the limiting factor in the reaction, the amount of light produced is proportional to the ATP concentration. However, the Photinus pyralis luciferase traditionally employed in this assay suffers from relatively low stability in vitro and is sensitive to temperature and to the chemical environment, such as pH and detergents, thus limiting assay robustness. Therefore, the assay was conducted employing the CellTiter-Glo® Reagent, which contains a mutated form of Photuris pennsylvanica luciferase displaying increased chemical and thermostability. With this approach, a single reagent containing all the elements necessary for cell lysis and bioluminescence measurement of ATP could be dispensed in the wells of the cartridge, ready to be reconstituted and to start the assay simply upon sample addition. As the commercial kit is performed in solution, the assay was performed in a microwell format, to ensure rapid reagents mixing and high photons collection efficiency. The protocol was adapted to a 10 µL total volume analysis. By integrating the measured bioluminescence signal obtained at different ATP concentrations, a calibration curve was obtained (Fig. S2 of Supplementary material), displaying a LOD of 40 nM, which was in the same order of magnitude of that obtained using a bench-top luminometer (10 nM). This result is promising when considering the remarkable decrease in the total volume analysis and the ease-of-use of the portable device with respect to a bench top instrumentation. The field applicability of the method could be further improved exploiting luciferases displaying remarkably high stability features allowing to work even at extreme conditions (up to 50 °C for more than 1 h) [26]. In addition, future studies will be performed to immobilize enzymes within the channels of the PLEIADES chip, thus enabling to perform assays in a microfluidic flow regimen.

2.6.7. Applicability of the PLEIADES Chip for Astrobiology

The PLEIADES chip has been specifically designed in view of its future possible application in extraterrestrial exploration missions. The structure of the chip, with the monolithic integration of sensors and detection sites on the same glass substrate, provides compact size, minimal weight, high photons collection efficiency, intrinsic mechanical stability avoiding the risk of misalignment between sensors and reaction sites due to e.g. vibrations or shocks, simplified chip fabrication and handling, higher system robustness and higher overall reliability (e.g. reduces risk of sensor damages due to unwanted leaks from the microfluidic network). Additionally, the absence of pumping devices or radiation sources significantly reduces the overall power consumption and reduces the risk of electromagnetic interferences due to electrically actuated devices as pumps, valves or switches. The only electronic board required is the sensor front-end electronics whose power consumption is well below 1 W. System complexity is highly reduced, due to the limited need for ancillary hardware. As an autonomously-driven capillary flow is employed, microfluidic pumps and pressure-tight fluidic joints are not necessary. Similarly, chemiluminescence detection ensures high sensitivity and high specificity without the need of external radiation sources and radiation filters. Finally, the use of one photodiode for each functional site ensures optimal signal-to-noise ratio as well as a limited data budget, which can be three orders of magnitude lower than that of equivalent experiments performed using a CCD camera while ensuring similar analytical performances, thus providing faster data processing and reduced storage and transmission bandwidth requirements. Reduced system weight, size, complexity, power consumption and data budget are aspects of fundamental importance for a space mission, making the proposed system extremely attractive for application in this field. One of the main critical issues for analytical payloads applied in astrobiology is the long-term stability of reagents and materials under space conditions, in particular cosmic radiations. The PLEIADES chip is equipped with a-Si:H photosensors, which ensure superior performances in terms of radiation hardness with respect to other technologies. As concerns reagents, while the stability of antibodies [27] and aptamers [28] has been assessed in relevant environments, all other reagents still need to be investigated [29]. Further work is required to investigate and improve the stability of enzymes, taking advantage of currently available solutions for long-term enzyme conservation [30] or exploiting synthetic enzyme mimics. Despite this, the possibility to employ enzyme-based assays for searching life markers is worth being explored, since it would expand the range of possible targets to several molecules for which avid antibodies are not available, while enzyme assays are well-established, such as cholesterol, NAD(P), phosphoenolpyruvate, porphyrins. Provided that suitable measures are adopted to ensure long-term enzymes stability and to control key factors, such as temperature and pH during the assay, several relevant analytes could be thus targeted taking advantage of high enzyme turnover and signal amplification that can lead to highly sensitive assays.

2.7 CONCLUSIONS

The primary scientific objective of the PLEIADES chip is to detect a range of biomolecules in a liquid aqueous sample, obtained upon extraction of a soil or crushed rock sample or upon melting of an ice sample. The PLEIADES chip has been designed as an integrated chip containing all the elements for performing the analytical procedure. In a complete analytical system for in situ analysis upon landing on a celestial body, the chip shall be accompanied by some ancillary instrumentation, such as a temperature control system, a sample preparation system and an automated pipetting unit for delivering the samples and the reagents to the inlets of the autonomous capillary network. In addition, suitable protection from cosmic radiations and temperature excursions shall be provided during the journey through the Solar System. Besides the compact size and the minimal weight, the monolithic integration of sensors, detection sites and microfluidics on the same glass substrate provides several positive features for space applications of the PLEIADES chip, such as intrinsic mechanical stability, reduced overall power consumption and data budget. Different chemiluminescence bioassays were implemented on the PLEIADES chip to demonstrate its versatile applicability. In the future, multiplexed assays will be developed and a full laboratory validation with simulated samples will be performed.

ACKNOWLEDGEMENTS

The project PLEIADES (Planetary Life Explorer with Integrated Analytical Detection and Embedded Sensors) was supported by the Italian Space Agency (ASI) (Accordo n. 2015-037-R.0).

REFERENCES

[1] G. Adornetto, A. Porchetta, G. Palleschi, K.W. Plaxco, F. Ricci; Chem. Sci., 2015, 6, pp. 3692-3696

[2] M. Baqué, M. Dobrijevic, A. Le Postollec, T. Moreau, C. Faye, F. Vigier, S. Incerti, G. Coussot, J. Caron, O. Vandenabeele-Trambouze; Int. J. Astrobiol., 2017, 30, pp. 82-90

[3] M. Baqué, A. Le Postollec, C. Ravelet, E. Peyrin, G. Coussot, I. Desvignes, S. Incerti, P. Moretto, M. Dobrijevic, O. Vandenabeele-Trambouze; Astrobiology, 2011, 11, pp. 207-211

[4] R.W. Court, M.R. Sims, D.C. Cullen, M.A. Sephton, Astrobiology, 2014, 14, pp. 733-752

[5] F. Costantini, E.M. Benetti, D.N. Reinhoudt, J. Huskens, G.J. Vancso, W. Verboom, Lab Chip, 2010, 10, pp. 3407-3412

[6] F. Costantini, C. Sberna, G. Petrucci, C. Manetti, G. DeCesare, A. Nascetti, D. Caputo, Sens. Biosens. Res., 2015, 6, pp. 51-58

[7] F. Costantini, C. Sberna, G. Petrucci, M. Reverberi, F. Domenici, C. Fanelli, C. Manetti, G. de Cesare, A. Nascetti, M. De Rosa, D. Caputo, Sens. Actuator B-Chem., 2016, 230, pp. 31-39

[8] J.L. Eigenbrode, R.E. Summons, A. Steele, C. Freissinet, M. Millan, R. Navarro-González, B. Sutter, A.C. McAdam, H.B. Franz, D.P. Glavin, P.D. Archer Jr., P.R. Mahaffy, P.G. Conrad, J.A. Hurowitz, J.P. Grotzinger, S. Gupta, D.W. Ming, D.Y. Sumner, C. Szopa, C. Malespin, A. Buch, P. Coll, Science, 2018, 360, pp. 1096-1101

[9] A.D. Ellington, J.W. Szostak, Nature, 1990, 346, pp. 818-822

[10] D.E. Huizenga, J.W. Szostak, Biochemistry,1995, 34, pp. 656-665

[11] S. Jahanshahi-Anbuhi, B. Kannan, V. Leung, K. Pennings, M. Liu, C. Carrasquilla, D. White, Y.F. Li, R.H. Pelton, J.D. Brennan, C.D.M. Filipe Chem. Sci., 2016, 7, pp. 2342-2346

[12] N. Kajiyama, E. Nakano, Biosci. Biotechnol. Biochem., 1994, 58, pp. 1170-1171

[13] D.L. Ma, W.H. Wang, Z.F. Mao, T.S. Kang, Q.B. Han, P.W.H. Chan, C.H. Leung, ChemPlusChem, 2017, 82, pp. 8-17

[14] M. Mirasoli, M. Guardigli, E. Michelini, A. Roda, J. Pharm. Biomed. Anal., 2014, 87, pp. 36-52

[15] M. Mirasoli, A. Nascetti, D. Caputo, M. Zangheri, R. Scipinotti, L. Cevenini, G. de Cesare, A. Roda, Anal. Bioanal. Chem., 2014, 406, pp. 5645-5656

[16] M.I. Mohammed, S. Haswell, I. Gibson, Procedia Technol., 2015, 20, pp. 54-59

[17] M. Moreno-Paz, A. Gomez-Cifuentes, M. Ruiz-Bermejo, O. Hofstetter, A. Maquieira, J.M. Manchado, S. Morais, M.A. Sephton, R. Niessner, D. Knopp, V. Parro, Astrobiology, 2018, 10.1089/ast.2017.1747

[18] A. Nascetti, G. Colonia, D. Caputo, M. Tavernelli, P. Placidi, A. Scorzoni, G. de Cesare, Procedia Eng., 2014, 87, pp. 1577-1580

[19] J. Parnell, D. Cullen, M.R. Sims, S. Bowden, C.S. Cockell, R. Court, P. Ehrenfreund, F. Gaubert, W. Grant, V. Parro, M. Rohmer, M. Sephton, H. Stan-Lotter, A. Steele, J. Toporski, J. Vago, Astrobiology, 2007, 7, pp. 578-604

[20] V. Parro, G. de Diego-Castilla, J.A. Rodriguez-Manfredi, L.A. Rivas, Y. Blanco-Lopez, E. Sebastian, J. Romeral, C. Compostizo, P.L. Herrero, A. Garcia-Marin, M. Moreno-Paz, M. Garcia-Villadangos, P. Cruz-Gil, V. Peinado,

J. Martin-Soler, J. Perez-Mercader, J. Gomez-Elvira, Astrobiology, 2011, 11, pp. 15-28

[21] N.M.M. Pires, T. Dong, U. Hanke, N. Hoivik, Sensors, 2014, 14 pp. 15458-15479

[22] P. Poinot, C. Geffroy-Rodier, TRAC-Trends Anal. Chem., 2015, 65, pp. 1-12

[23] A. Roda, M. Mirasoli, M. Guardigli, M. Zangheri, C. Caliceti, D. Calabria, P. Simoni, Biosens. Bioelectron., 2018, 111, pp. 18-26

[24] A. Roda, M. Mirasoli, E. Michelini, M. Di Fusco, M. Zangheri, L. Cevenini, B. Roda, P. Simoni, Biosens. Bioelectron., 2016, 76, pp. 164-179

[25] M.A. Sephton, M.R. Sims, R.W. Court, D. Luong, D.C. Cullen, Planet. Sp. Sci., 2013, 86, pp. 66-74

[26] R.A. Shircliff, P. Stradins, H. Moutinho, J. Fennell, M.L. Ghirardi, S.W. Cowley, H.M. Branz, I.T. Martin, Langmuir, 2013, 29, pp. 4057-4067

[27] M.R. Sims, D.C. Cullen, C.S. Rix, A. Buckley, M. Derveni, D. Evans, L.M. Garcia-Con, A. Rhodes, C.C. Rato, M. Stefinovic, M.A. Sephton, R.W. Court, C. Bulloch, I. Kitchingman, Z. Ali, D. Pullan, J. Holt, O. Blake, J. Sykes, P. Samara-Ratna, M. Canali, G. Borst, H. Leeuwis, A. Prak, A. Norfini, E. Geraci, M. Tavanti, J. Brucato, N. Holm, Planet. Sp. Sci., 2012, 72, pp. 129-137

[28] C. Tuerk, L. Gold, Science, 1990, 249, pp. 505-510

[29] R. Vitale, L. Lista, C. Cerrone, G. Caserta, M. Chino, O. Maglio, F. Nastri, V. Pavone, A. Lombardi Org. Biomol. Chem., 2015, 13, pp. 4859-4868

[30] M.H. Xie, K. Zhang, F.F. Zhu, H. Wu, P. Zou, RSC Adv., 2017, 7, pp. 50420-50424

3

SPLIT G-QUADRUPLEX CHEMILUMINESCENT DNAzyme FOR ANTIBODIES DETECTION

3.1 INTRODUCTION

Over the past twenty years, the wide use of nanoscale or nanostructured biomaterials has kicked off the development of novel analytical approaches for point-of-care (POC) applications and new therapy platforms, considerably improving our ability to predict earlier stage diseases and leading to an improvement of the quality of human life [1]. As an emerging field, DNA nanotechnology offers simple, powerful and predictable design techniques for nanostructures self-assembly with unique advantages of improving the sensitivity of the system, leading the multiplex detection of a wide range of targets, from proteins, DNA, RNA to small molecules [2]. Recently the detection of proteins by DNA probes able to fold into active peroxidase-mimicking G-quadruplex DNAzymes has gained increasing interest. Deoxyribozymes (DNAzymes) are defined as artificial nucleic acids able to catalyse some chemical reactions [3]. In particular, an alternative DNA motif with a special four-stranded structure associate via Hoogsteen hydrogen-bonding, the so-called G-quadruplex, has shown great potential for biosensing applications [4,5]. Furthermore, split G-quadruplex has been introduced and applied as a binary probe in many fields for its flexible structure and design [6–7]. In this strategy, the guanine bases of the G-quadruplex are distributed on two different strands, each of which is not catalytically active when alone. The two strands can be, however driven together by external stimuli to reproduce the native G-quadruplex structure, displaying peroxidase-like catalytic activity, which is increased in the presence of hemin, a small molecule able to catalyse H_2O_2-mediated oxidation of 2,2′-azino-bis(3-ethylbenzothiazoline-6-sulfonic acid) (ABTS)[8], luminol[9,10], or thiamine[11]. Among them, chemiluminescence (CL) detection observed in the presence of the luminol/H_2O_2 cocktail, has attracted substantial research efforts due to its remarkable properties such as high sensitivity, wide calibration range, and simple instrumentation [12-14], reducing the number of analytical steps for biomolecule sensing [15]. Several methods for discovering and investigating macro-molecular interactions [16] in a complex matrix have been developed. Two and three-hybrid approaches [17,18] as well as bimolecular fluorescence resonance energy transfer (FRET) [19] are widely used to study protein–protein interactions, both qualitatively and quantitatively. In particular split-protein reassembly methods have emerged as a potentially simple and general solution for studying protein–protein interactions [20]. This approach leans on the appropriate fragmentation of protein reporters, such as the green fluorescent protein (GFP) or firefly luciferase [21], which can reassemble only after the recognition of the partner, regaining its primary function. Inspired by nature, synthetic supramolecular chemistry provides the opportunity to study the biological phenomena which initially found its conception [22]. Supramolecular self-assembly is based on non-covalent interactions of relatively simple building blocks and gaining control over these is the key to define a useful strategy for the inceptive comprehension of more complex biological system behavior. However, the realization of these complex systems, using DNA nanotechnology, need to overcome the gap between chemical experiments performed under standard controlled conditions and spatially structured, densely packed cellular environments [23]. Motivated by the above consideration, a split G-quadruplex DNAzyme platform for the chemiluminescent and quantitative detection of antibodies based on antibody-induced co-localization proximity mechanism, was developed.

3.2 MATERIALS AND METHODS

3.2.1 Reagents and materials

Antibodies were purchased from Roche Diagnostic Corporation, Germany (sheep polyclonal anti-digoxigenin, anti-Dig), Thermo Fisher Scientific, USA (murine monoclonal, anti-OCRA, Anti-OVA). All antibodies were solubilized in phosphate-buffered saline (PBS) pH 7.4 (137 mM NaCl, 2.7 mM KCl, 4.3 mM Na_2HPO_4, 1.47 mM KH_2PO_4), aliquoted and stored at 4°C for immediate use or at -20°C for long-term storage. DNA sequences purified via high-performance liquid chromatography (HPLC) were purchased from Integrated DNA Technologies (IDT) (Iowa, United States). All reagent-grade chemicals were used without further purification. Hemin from bovine (90%), trizma hydrochloride, luminol sodium salt, were purchased from Sigma-Aldrich (St Louis, Missouri). Sodium hydroxide and potassium dihydrogen phosphate were purchased from Carlo Erba Reagents (Milano, Italy). Hydrogen peroxide (30%) was purchased from VWR International (Pennsylvania, United States). Ultrapure water from Merck Millipore (Billerica, MA) source was used throughout the experiments.

3.2.2 DNA Sequences

The oligonucleotides were used as provided and diluted in pH 7.5, 50mM phosphate buffer solution to give 100μM stock solutions. The sequences of the split G-quadruplex DNAzyme are as follows:

Split G-quadruplex 4:8

BRIDGE LENGHT	**6MER**	**8MER**	**NO BRIDGE**
STRAND 1	5'- (DIG) *TTT TTT TTT T* ATC ACA GGG T -3'	5'- (DIG) *TTT TTT TTT T* GT ATC ACA GGG T -3'	5'- (DIG) *TTT TTT TTT T* GGG T -3'

STRAND 2	5’- AGGGCGGG TGT GAT *TTT TTT TTT T* (DIG) -3’	5’- AGGGCGGG TGT GAT AC *TTT TTT TTT T* (DIG) -3’	5’- AGGGCGGG *TTT TTT TTT T* (DIG) -3’

In the sequences above, the underlined bases represent the G-quadruplex split ratio (4:8) while the red bases represent the stem portion, defined as “Bridge”, here reported with different lengths (6, 8 and no bases). The design and free energy comparisons of DNA sequences were performed by hand and verified by NUPACK software suite [30].

3.2.3 Chemiluminescence Measurements

DNA oligos concentration was estimated by measuring the absorbance on a Varian Cary 50Scan UV-Vis spectrophotometer setting excitation wavelength to λ = 260 nm (slit = 10 nm) and using quartz cuvettes of reduced volume (100 μL). Chemiluminescence measurements were carried out in microtiter plate format using a Thermo Scientific Luminoskan Ascent luminometer (Thermo Fisher Scientific). All measurements were performed at T = 25°C. The chemiluminescent emission signals were collected using the optimized final concentration of 50 nM of the G-quadruplex DNA formed by Strand-1 and Strand-2 mixture. The relevant antibody was added at the desired final concentration (in the range 3 nM - 100 nM) and the mixture was incubated for 20 minutes. Eventually equimolar concentration of hemin (50 nM) was added and luminol and hydrogen peroxide were automatically injected at a final concentration of 0.5 mM and 30 mM respectively. The chemiluminescent emission of luminol in presence of hemin and hydrogen peroxide alone was always acquired and subtracted as reference blank sample, as well as Strand-1 and Strand-2 (50 nM) in the absence of the target antibody.

3.3 RESULTS AND DISCUSSION

3.3.1 Assembly of a Split G-Quadruplex DNAzyme using an Anti-Digoxigenin Antibody

Our analytical platform is composed of two DNA single strands (Strand1 and Strand2), both labelled with a specific antigen recognized by the target antibody. We engineered both Strand1 and Strand2 with a split G-quadruplex sequence divided into two portions by the ratio of 4:8. able to undergo conformation reconfiguration from external stimuli once they are bound to the target antibody. Additional spacer tails composed of 10 thymine units were introduced at the 5′-terminus of Strand-1 and at the 3′-terminus of Strand-2 (i.e., in correspondence of the base of the main stem), in order to endow the two DNA segments with enough flexibility. A Dig molecule is then conjugated to each of these spacer tails (Figure1). The proper formation of G-quadruplex is favoured by the specific molecular recognition between the target antibody and its antigen conjugated with the DNA probes. The antigen-antibody interaction induces an increase in the effective concentration of the two DNA strands, which, due to the proximity effect, can fold correctly [4]. After the addition of hemin, hydrogen peroxide and luminol, a chemiluminescent signal is generated. The advantages of pursued strategy are: first, the Y-shaped geometry that all IgG antibodies share, with two identical binding sites separated by about 6–14 nm [24–25]; second, the possibility to easily conjugate different recognition elements to synthetic nucleic acid strands [27]. The two oligonucleotides have complementary stem domain designed to hybridize and form a duplex. Upon antibody binding, the two oligonucleotides are co-localized into a confined volume thus inducing efficient hybridization. This leads to the two split G-quadruplex strands into close proximity, greatly increasing their effective concentration and triggering the proper folding of the G-quadruplex structure (Figure1).

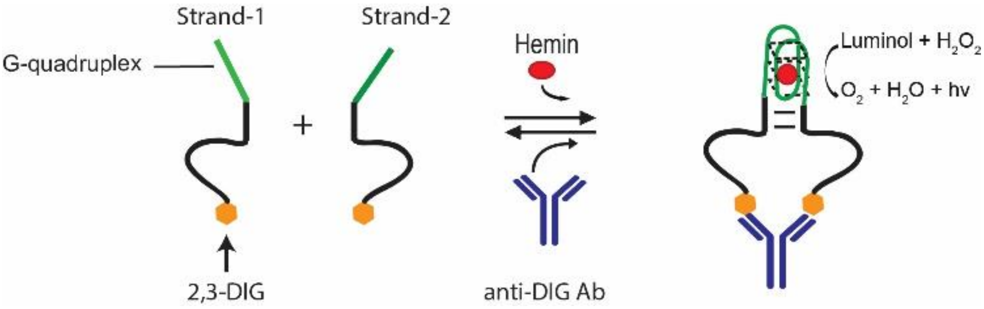

Figure1. Nucleic acid-based co-localization probes for optical antibody detection. Here the DNA nanosystem is employed in conjunction with an antibody-induced co-localization mechanism. In this specific case, the spatial geometry of the target antibody is used to induce an increase in the effective concentration of two DNA strands, each conjugated with a recognition element (i.e., an antigen). The distance of approximately 10–12 nm between the two binding sites of a single antibody provides an increase in effective concentration of the two DNA strands, which can be exploited to trigger the proper folding of the G-quadruplex structure. Upon addition of hemin, hydrogen peroxide and luminol, the G-quadruplex generates a chemiluminescent signal.

Stimulated by the desire to investigate the best split G-quadruplex ratio, we carried out our research about the better comprehension of the mechanism at the base of the effectively G-quadruplex splitting, in order to achieve the best chemiluminescent signal. In this strategy, the guanine bases of the G-quadruplex are distributed on two different strands, held together only after the interaction of the two DNA strands with the target antibody. The binding event allows the colocalization of the two split G-quadruplex sequences in close proximity leading the proper folding of the native G-quadruplex structure. First, three different split G-quadruplex ratios: 4:8, 3:9; 6:6 were studied. As shown in Fig2 the best signal/noise ratio is generated by the Split: 4:8 that shows the lowest background. We deduced that the two G-rich segments, generated by splitting 6 : 6 the G-quadruplex sequence, easy bind together by themselves and the chemiluminescence signal observed is relatively high even without co-localization mechanism induced by the antibody. In 3:9 G-quadruplex split ratio, the three guanine bases on Strand-2 might be too short, hindering the native G-quadruplex conformation. Thus, the structure of the split G-quadruplex is still imperfect and the chemiluminescence signal is weak, as confirmed in the study of Jinbo Zhu and co-workers [26]. Unlike previous, the G-quadruplex split ratio 4:8 is more prone to undergo sequence modification without significant loss of the catalytic activity (i.e., interaction with hemin and activation of chemiluminescence emission), because the main sources of the backgrounds for the corresponding split modes are caused by the long G-rich strand, rather than the interaction between the short and long G-rich strands.

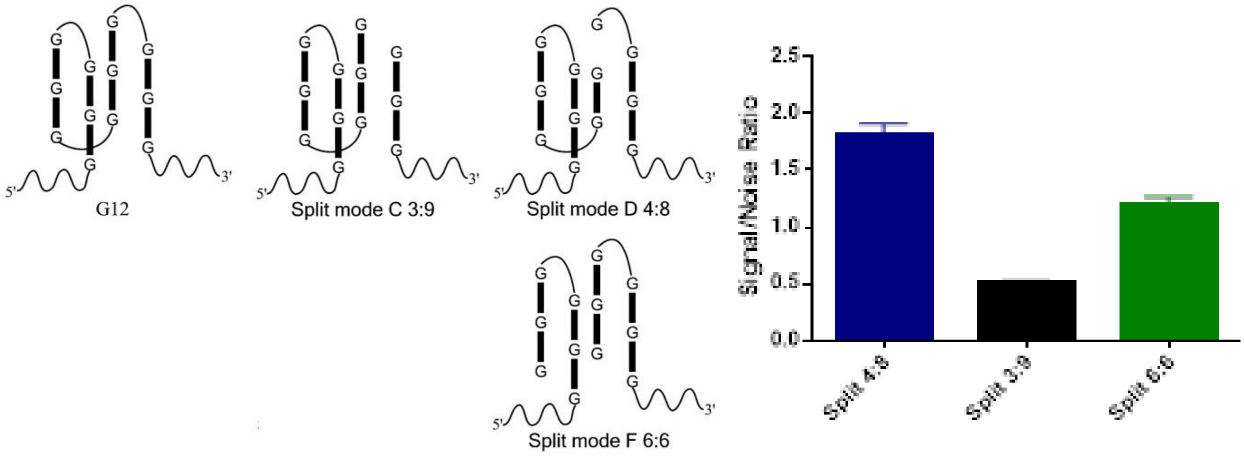

Figure2. Signal/Noise ratio of the three different split mode (4:8; 3:9; 6:6) obtained by chemiluminescent measurements performed using the three different split Strand1 and Strand2 G-quadruplex ratios: 4:8, 3:9; 6:6. As shown in Fig2 the best signal/noise ratio is generated by the Split: 4:8 that shows the lowest background.

In the absence of the target antibody, an equimolar solution of Strand-1 and Strand-2 (NoBridge; 50 nM) shows a hemin catalytic activity that is 10-fold poorer than that of the original native G-quadruplex sequence at the same concentration (Figure 3). This demonstrates that the split G-quadruplex configuration shows only a poor catalytic activity ability which, consequently, leads to very weak signalling. This experimental evidence confirms the fundamental function performed by the antibody. Following the binding with the digoxigenin molecules conjugated to the DNA probes, the target bio-element drives the correct folding of the G-quadruplex. In fact, a local critical increase in the concentration of the two DNA halves is generated, which favours mutual interaction due to the proximity effect.

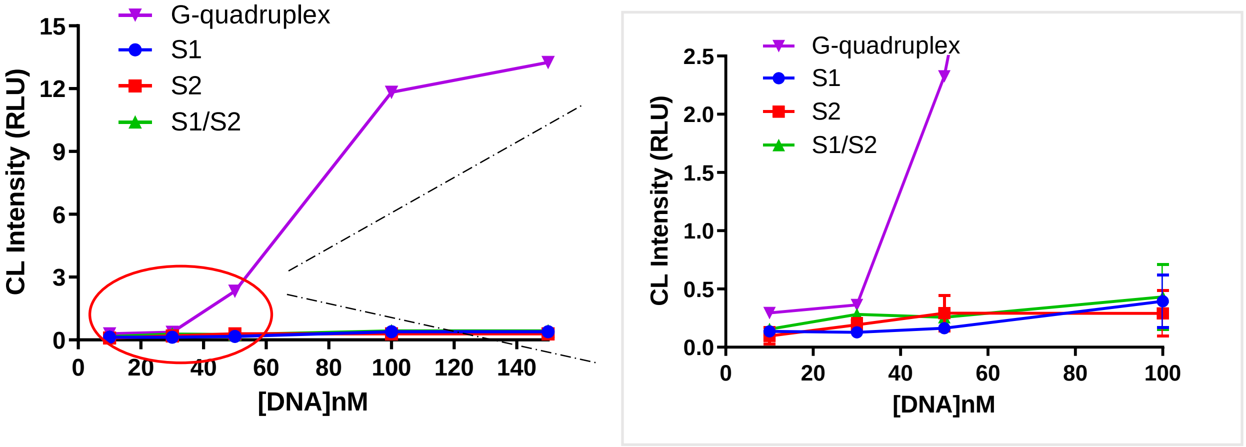

Figure3. Hemin binding curves of Split G-quadruplex (blue, red, green) and native G-quadruplex (purple) in the absence of the target Anti-Digoxigenin Antibody.

However, in the presence of Anti-Digoxigenin (Anti-DIG) antibody, the affinity of the split G-quadruplex for hemin is restored, showing the same behaviour of the original wild-type G-quadruplex sequence. This provides the evidence for the proposed mechanism, as shown in Figure4. For the optimization of the DNA nanosystem, according to the aim mentioned above, the equilibrium of the system was tuned by simply changing the length of the stem sequence, the “bridge”, inside Strand-1 and Strand-2, in order to achieve the best sensitivity towards the target antibody. Indeed, the stem complementary sequence implies a double effect: on the one hand allows the correct co-localization of Strand-1 Strand-2 (Strand-1/Strand-2 rather than Strand1-Strand-1 or Strand2-Strand-2) on the other hand, it might shift the equilibrium toward the hybridization of the Strand1- Strand-2 even in absence of the target antibody. To identify such optimal trade-off, a set of

DNA probes differing in the length of their complementary stem domains (and, therefore, duplex stabilities) was designed. More specifically, the lengths of stem complementary domains with lengths ranges from 0 to 8 nucleotides (nt), in particular corresponding to Strand-1/Strand-2 "NoBridge" (without any complementary sequence region), Strand-1/Strand-2 "Bridge 8MER" (with a complementary sequence region of eight basis), and Strand-1/Strand-2 "Bridge 6MER" (with a stem sequence of six basis). The chemiluminescence signal obtained from the kinetic profile of Strand-1 and Strand-2 (NoBridge, Bridge 8MER and Bridge 6MER) in the presence of an equimolar concentrations of both Anti-Dig antibody (10, 30, 50, 100nM) and hemin (10, 30, 50, 100 nM), incubated for 25 minutes, was compared. The resulting curves allowed us to both evaluate the catalytic activity of the re-folded G-quadruplex and at the same time which couple of DNA Strands was thermodynamically suitable in terms of sensitivity for antibody detection. As expected, co-localization induced by the bivalent binding of the antibody led to an increase in affinity between strand-1 and strand-2. In particular, NoBridge Strands with 0 nucleotides complementary domain led to the highest chemiluminescent signal/noise ratio, as reported in Figure4.

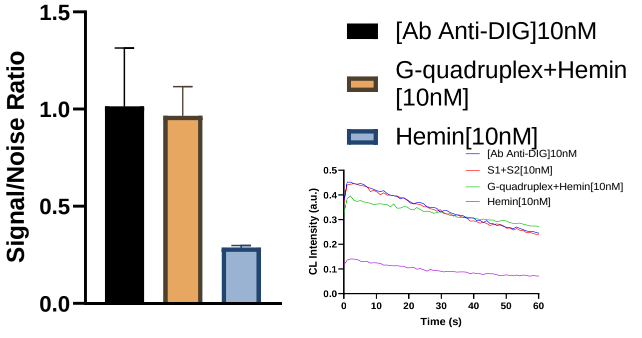
[DNA NoBridge] 10nM

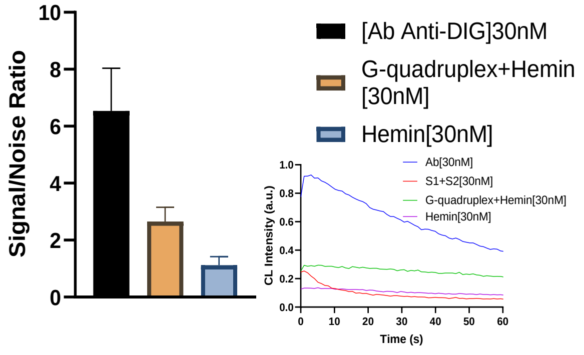
[DNA NoBridge] 30nM

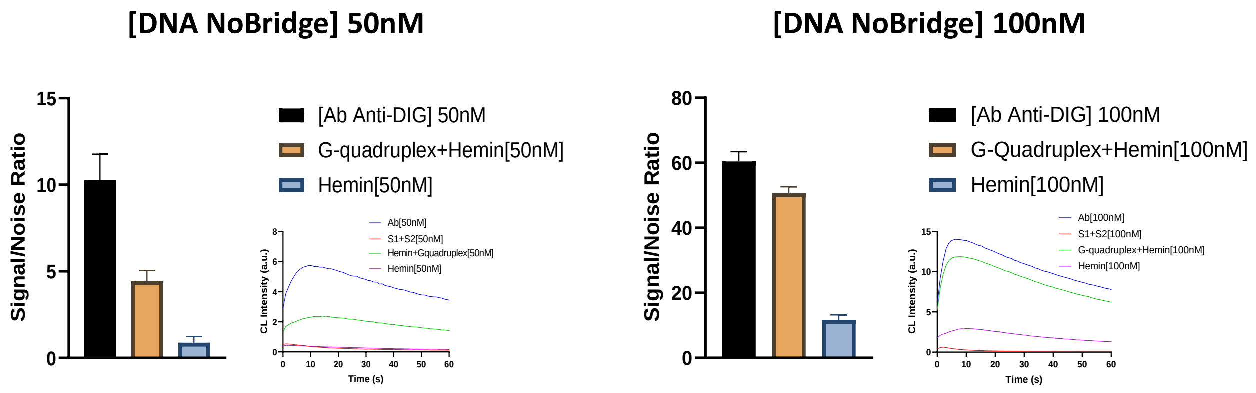

Figure4. NoBridge Strands with 0 oligonucleotides in the stem domain was tested to study the effect of the Antibody on the interaction between hemin and the split G-quadruplex configuration. Chemiluminescence raw signal obtained in the presence of Strand-1 and Strand-2 mixed with equimolar concentrations of both Anti-Dig antibody (10, 30, 50, 100 nM) and hemin (10, 30, 50, 100 nM), incubated for 25 minutes. The experiments were carried out t 25 °C in PBS 1x buffer pH 7.2.

As shown by the measurements in Fig4a, “NoBridge” showed a low background signal noise in the absence of the target, probably due to lack of the stem domain accountable for switching the equilibrium toward the spontaneous hybridization of strand-1 and strand-2. The affinity observed towards the antibody of “NoBridge” Strand1-Strand-2 shown in Fig5b (Kd = 2.4 ± 0.7nM) was calculated fitting data by a “One site - Specific binding with Hill slope model” following the equation Y=B_{max}*X^h/(Kd^h + X^h), where Y represent the CL signal that is proportional to bound ligand, B_{max} is the maximum specific binding in the same units as Y (B_{max} =183 ± 15 auc) and h is the Hill Slope (h = 0,7 ± 0.2) and describes the steepness of the family of curves. The value of Kd calculated, not only is influenced by the dissociation constant between antigen and antibody, but also takes into account to the proximal interaction strength between the complementary DNA sequences, the non-covalent forces involved in the intercalation of hemin between the purine bases of the G-quadruplex and the bond between the H_2O_2 and the porphyrin center which in turn catalyzes the oxidation of luminol and triggers the emission of photons.

In order to further investigate the specificity of our DNA nanosystem, the “NoBridge” probe was selected. As shown by the graph in Fig5d, no significant cross-reactivity has been observed, enabling the detection of specific antibodies.

Apart from the sensitivity and high specificity discussed above, the approach is also extremely versatile and could be easily adapted to the detection of any antibody, antigen and bivalent macromolecular targets.

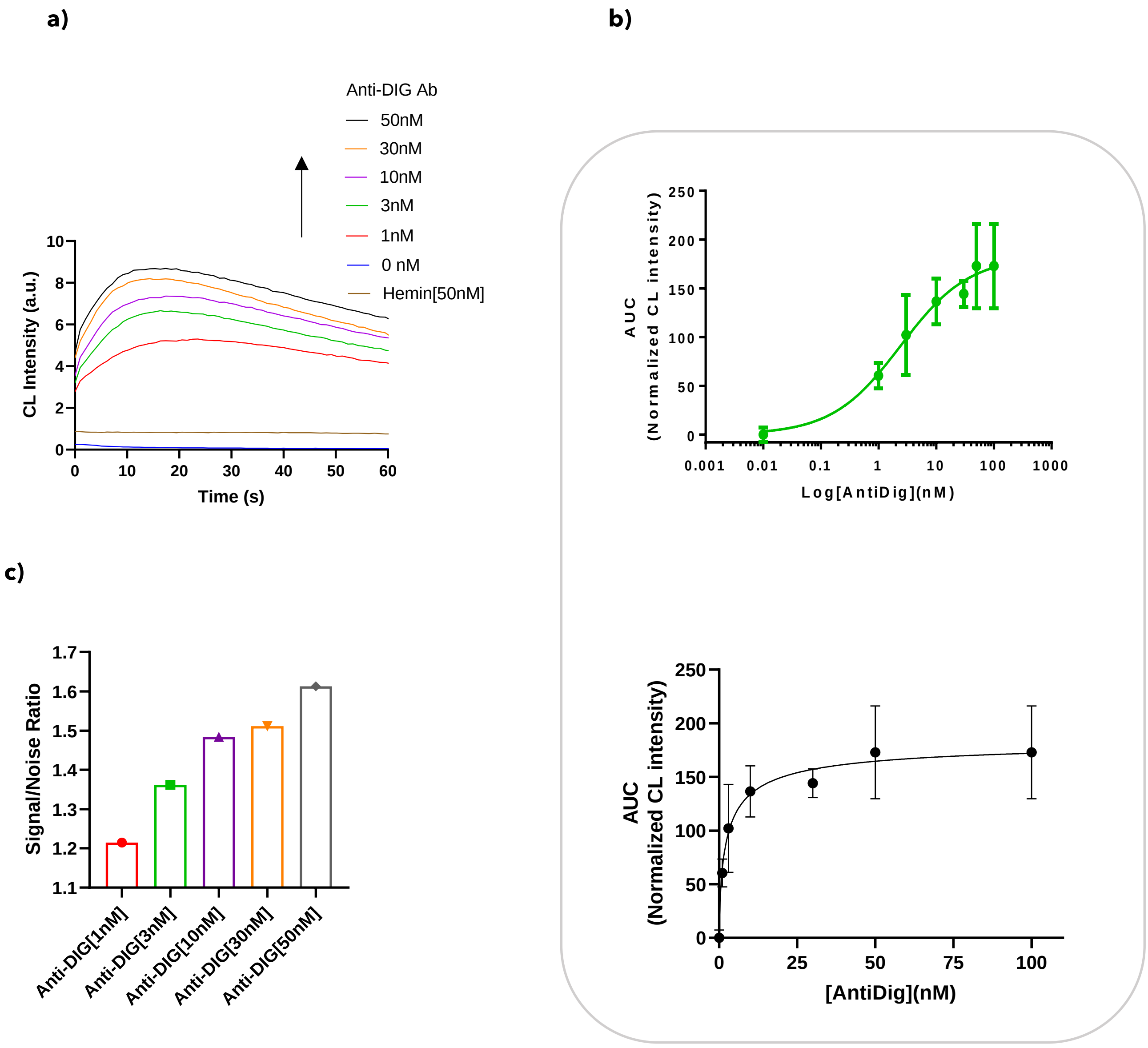

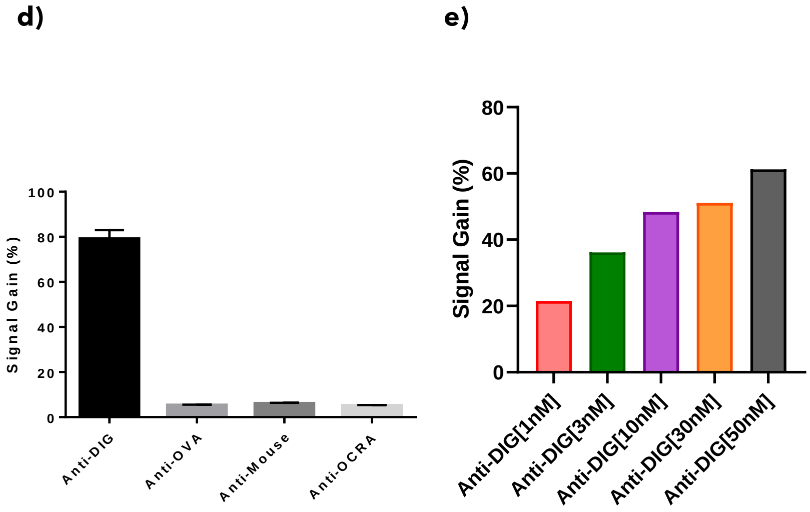

Figure5. Split G-quadruplex NoBridge for Anti-DIG detection. (A) Raw Chemiluminescence kinetic profiles of re-folded G-quadruplex structure, using Digoxigenin (Dig) conjugated DNA sequences, as a function of the concentration of the Anti-DIG antibody target. (B) Binding curve of NoBridge Strands (50 nM) obtained by plotting the integral of area under the curve of CL kinetic profiles in the presence of increasing concentrations of Anti-Dig antibody (1,3,10,30,50,100 nM) expressed as normalized chemiluminescence intensity. (C) Signal/noise ratio of NoBridge Strands (50 nM) in the presence of increasing concentrations Anti-Dig antibody (1,3,10,30,50,100nM). (D) Evaluation of method selectivity: using variant NoBridge, chemiluminescent signal occurs only in the presence of the specific antibody (Ab Anti-DIG) and no significant cross reactivity is observed in the presence of other non-specific antibodies (at 100 nM). (E) Chemiluminescence % signal gain in the presence of Anti-Dig antibody (50 nM) obtained at different Anti-DIG concentrations. Unless otherwise noted the experiments are obtained in phosphate buffer saline PBS buffer, pH 7.4, T = 25 °C, using an equimolar concentration of the split strands ([split 1] = [split 2] = 50 nM) and a concentration of DFHBI of 10 µM. Results are reported as mean value of three independent measurements and the error bars reflect the standard deviations.

3.4 CONCLUSIONS

We have investigated a bio-supramolecular mechanism in which a split G-quadruplex DNAzyme is able to reassemble into the functional native G-quadruplex structure as a consequence of a spatial proximity effect [26]. We demonstrated the applicability of this approach using antibodies as template biomolecules that induce colocalization of split G-quadruplex halves. Looking forward, alternative design may be explored to improve the chemiluminescence background of split G-quadruplex. Some improvements can be reached introducing different split points, modifying the length of the thymine tails, or different base pairing in the stem region. We also believe the same mechanism might be translated to some of the available alternative formats of the Split G-quadruplex DNAzyme [27]. The demonstrated colocalization mechanism may be extended to other DNA or RNA aptamers and sequences, allowing the construction of programmable supramolecular DNA or RNA-based nanostructures with binding-responsive properties [28-29]. A similar mechanism could be explored in the future in order to investigate new sets of colocalization-based probes. The strategy proposed may be valid for a wide range of substrates, in particular all those proteins that display bi- or multivalency and are then able to assist colocalization assembly.

REFERENCES

1 S.Ranallo, M. Rossetti, K. W. Plaxco, A. Vall¦e -B¦lisle, F. Ricci, Angew. Chem., 2015, 127, 13412 –13416

2 A. Porchetta, R. Ippodrino, B. Marini, A. Caruso, F. Caccuri, F. Ricci, J. Am. Chem. Soc., 2018, 140, 3, 947–953

3 H. Zhang, F. Li, B. Dever, C. Wang, X.F. Li, X.C. Le, Angew Chem Int Ed Engl., 2013, 52,10698-705

4 A. Roda, M. M. Calabretta, D. Calabria, C. Caliceti, L. Cevenini, A. Lopreside, M. Zangheri, Compr. Anal. Chem., 2017, 77, 237-286

5 M. M. Calabretta, M. Zangheri, A. Lopreside, E. Marchegiani, L. Montali, P. Simoni, A. Roda, Analyst, 2020,145, 2841-2853

6 G.Y. Gao, B. Li, Anal Chem., 2013,85,11494-500

7 I. Willner; M. Shlyahovsky; B. Zayats, B. Chem. Soc. Rev.,2008,37, 1153−1165

8 X. H. Zhao, L. Gong,; Zhang, X. B.; Yang, B.; Fu, T.; Hu, R.;Tan, W. H.; Yu, R., Q. Anal. Chem., 2013,85, 3614−3620

9 Y. Huang, J. Chen; S. Zhao; M. Shi; Z.F. Chen; H. Liang, Anal. Chem., 2013,85, 4423−4430

10 M. Luo; x. Chen; G. Zhou; X. Xiang; L. Chen; Z. Ji He, Chem. Commun., 2012,48, 1126−1128

11 T.Li, E. Wang, S. Dong, Anal. Chem., 2010,82, 1515−1520

12 Y. Zhang; B. Li; Y. Jin, Analyst, 2011,136, 3268−3273

13 M. Zhou; Y. Liu; Y. Tu, G. Tao Yan, J.Biosens. Bioelectron., 2012,35, 489−492

14 Y. P Zeng.; J. Hu; Y. Long; C.Y. Zhang, Anal. Chem., 2013,85,6143−6150

15 H. Dong; C. Wang; Y. Xiong; H. Lu; H. Ju.; X. Zhang, Biosens.Bioelectron.2013,41, 348−353

16 X. Liu, R. Freeman, E. Golub, I. Willner, ACS Nano, 2011,5,7648−7655

17. D.M. Kolpashchikov, J. Am. Chem. Soc., 2008, 130:2934–2935

18. M.P Stumpf, T. Thorne, E. de Silva, R. Stewart, H.J. An, M. Lappe, Proc NatlAcad Sci USA, 2008,105, 6959-6964.2

19 S. Fields, O. Song, Nature,1989,340:245-246.3.

20 E.J. Licitra, O.J. Liu,Proc Natl Acad Sci USA, 1996,93:12817-1282

21 J. Zhang, R.E Campbell, A. Ting, R.Y. Tsien, Nat Rev Mol Biol, 2002,3,906-918.

22 S.S. Shekhawat, I. Ghosh, Curr Opin Chem Biol.,2011;15, 789-9724.

23 L. Cevenini, M. M. Calabretta, A. Lopreside, G. Tarantino, A. Tassoni, M. Ferri, A. Roda, E. Michelini, Anal Bioanal Chem.,2016;408, 8859-8868

24. D. A. Uhlenheuer, K. Petkau, L. Brunsveld, Chem. Soc. Rev., 2010,39, 2817-2826

25 S. Ranallo, M. Rossetti, K. W. Plaxco, A. Vallee-Belisle, F. Ricci. 2015., Angew Chem Int Ed Engl, 54, 13214-8.

26 J. Zhu, L. Zhang, S. Dong, E. Wang, Chem Sci., 2015;6, 4822-4827

27 B. L. Pellejero, M. Mahdifar, G. Ercolani, Jonathan Watson2, Tom Brown Jr 2 & Francesco RiccNat Commun,2020, 11, 6242

28 Y. J. Chen, B. Groves, R. A. Muscat, G. Seelig, Nat. Nanotech., 2015, 10, 748-760

29 A. Bertucci, A. Porchetta, F. Ricci, Anal. Chem. 2018, 90, 1049−1053

30. J. N. Zadeh, C. D. Steenberg, J. S. Bois, B. R. Wolfe, M. B. Pierce, A. R. Khan, R. M. Dirks, N. A. Pierce.,J Comput Chem, 32,170–173, 2011

4

CHEMI/BIO-LUMINESCENT BASED STIMULUS-RESPONSIVE BREAKABLE ORGANOSILICA NANOCAPSULES FOR PHOTODYNAMIC THERAPY APPLICATIONS

4.1 INTRODUCTION

The efficient delivery of native, functional proteins or enzymes, in an active conformation localized into cell section of interest, still remains a challenge. Under physiological conditions, proteins and peptides can undergo proteolytic degradation and, in addition, higher-molecular-weight proteins, if recognized by neutralizing antibodies, can be the cause of the rising of the consequent risk for immunogenicity [1].

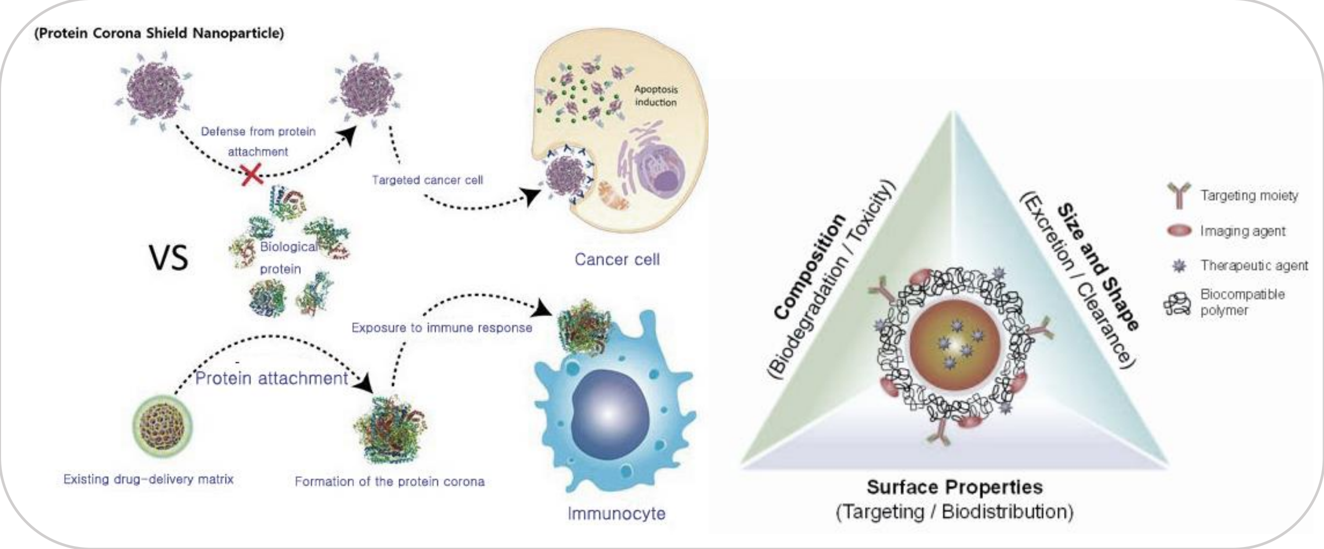

Fig 1. Schematic illustration of a theranostic NP and its physicochemical properties that regulate in vivo pharmacokinetics, biodistribution and toxicity.

To overcome these limitations, proper delivery systems must be able to shield and to protect the bioactive molecules in order to preserve their functional nature and their native biological activity [2]. The ability of the NPs to enter the cell is determined by both physicochemical parameters and biological barriers. Due to the high surface area to volume ratio (small size), they are able to cross cell membranes and deliver the drug inside them [3]. Moreover, the absorption of NPs within cell membranes and their distribution in biological systems depend on the nature of their building-blocks [4]. By changing the chemical composition and the time-depending protocol of synthesis of NPs, it is possible to modulate the dimensions and the surface charges that play an important role in the NP-cell interactions

(Fig.1). Nevertheless, a major challenge in current protein-based therapy is to develop highly effective intracellular protein delivery strategies providing rapid cell uptake and minimal endolysosomal trapping [5]. Enzymes with high catalytic activity and distinct substrate selectivity have also been utilized as clinical diagnostic tools to detect pathological markers. However, the lack of lasting stability and the difficulty in permeating through biological membranes of free enzymes have often limited their applications in complex biological milieu. In order to overcome this issue, Yuan and coworkers report the delivery of native proteins and antibodies to the mitochondria using biodegradable silica nanoparticles (BS–NPs) [6]. [7]. Indeed, the cytosol has a low redox potential due to the abundance of reduced glutathione (GSH) in the millimolar concentration range, whereas the extracellular glutathione concentration falls in the micromolar range [8]. To utilize this redox potential difference, a variety of protein delivery systems based on the dissociation of disulfide bonds have been reported [9] (Fig.2).

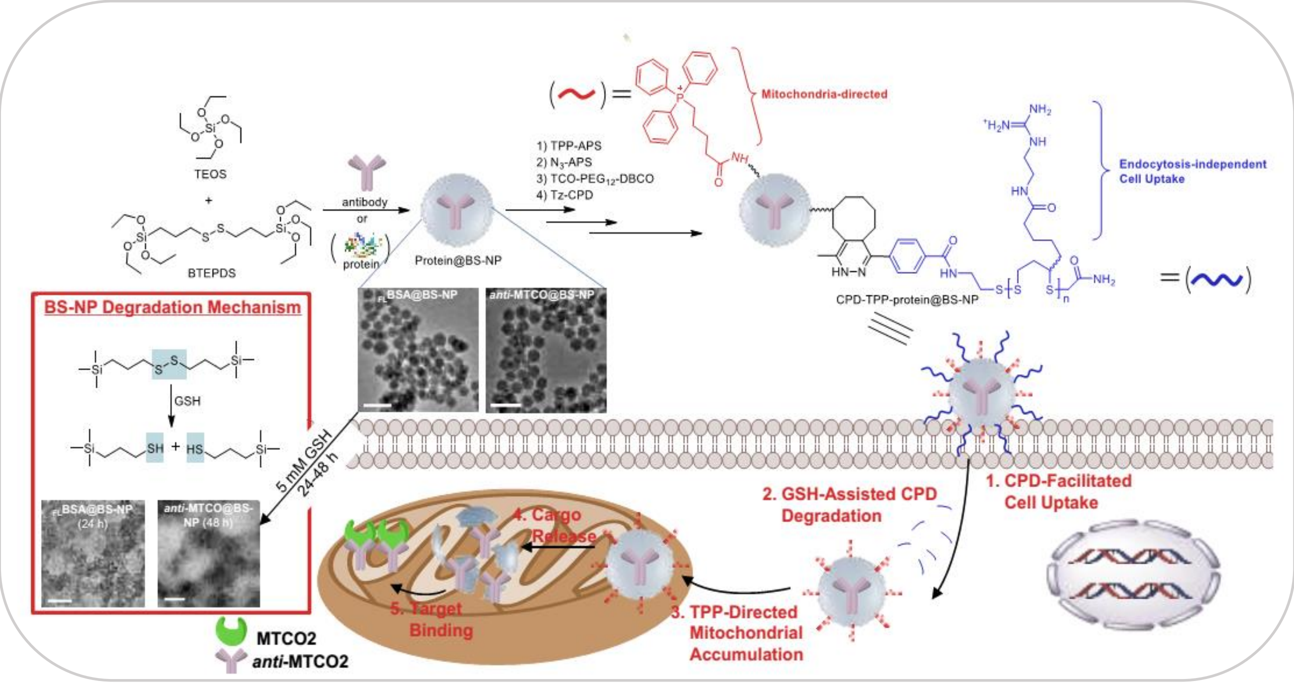

Reprinted with permission from: P. Yuan, X. M. Xiaofeng W. S. S. Liew, L. Li, S. Q. Yao, Angew. Chemie., 2019, ***131,*** *7739-7743)*

Fig.2 Schematic representation of the preparation of cell-permeable breakable silica nanocapsules protein loaded (CPD-TPP-protein@BS-NP), in which CPD-facilitated endocytosis-independent cell uptake (Step I), cytosolic GSH-assisted CPD depolymerization (Step II), TPP-directed mitochondrial accumulation (Step III), mitochondrial cargo release (Step IV), and finally target binding/engagement (Step V).TEM images (scale bar =100 nm) show the morphological changes of FLBSA@BS-NP and anti-MTCO@BS-NP before and after 5 mM GSH treatment (24-48 h).

Similarly, we tried to encapsulate horseradish peroxidase (HRP) enzyme inside breakable silica nanocapsules. HRP is used extensively in biochemistry applications, because of its capability to catalyse the oxidation of various organic substrates in the presence of hydrogen peroxide. Indeed, when HRP is incubated with a proper substrate, it produces a coloured [9] or luminescent derivative, allowing it to be detected and quantified. In the colorimetric assay, 3,3′,5,5′-Tetramethylbenzidine (TMB) cab be used, which acts as a reducing agent for hydrogen peroxide (H_2O_2), the reaction being catalyzed by HRP. The diimine product accumulation results in a rising blue colour of the solution and the progress of the reaction can be monitored by absorbance measurements at the wavelengths of 370 and 650 nm. After the addition of stop reaction reagent, commonly a H_2SO_4 2 N solution, the colour of mixture changes its tint toward the yellow, showing a maximum wavelength of absorbance at 450 nm [10]. The colorimetric assay can be used to test if the enzyme is still active after the release. More sensitive alternative detection methods are the luminescence-based techniques. In particular, chemiluminescence (CL) is the emission of light (luminescence), as the result of a chemical reaction catalysed by HRP. In presence of H_2O_2 and luminol, HRP catalyses the oxidation of luminol to 3-aminophthalate in its excited state, which emits a photon as it decays to a lower energy level. The reaction is accompanied by emission of low-intensity light at 428 nm [11]. Chemiluminescence can be used to generate light inside the cell and this approach could be employed in bioimaging and photodynamic therapy (PDT) applications, overcoming the well-known limitations of fluorescence-based method [12].

Over the past few decades, nanoprobes have been developed and applied to molecular imaging of inflammation [13,15]. Luminescence imaging is a low-cost, rapid, and highly sensitive approach that enables real-time detection of a wide variety of cellular, subcellular, or molecular events during an inflammatory response [13, 14]. Several nanoparticles have been extensively investigated in targeted cancer therapy. Despite their great success, clinical translation of most existing photosensitizers is hindered by the limited penetration depth of external light required for their activation [12, 16]. To overcome this barrier, self-illuminated PDT has been proposed for tumor therapy in the absence of external excitation [17–20]. In this modality, the photosensitizer is triggered by the microenvironment, producing cytotoxins such as singlet oxygen (O_2) to kill cancer cells, resulting in internal chemiluminescence (CL) or bioluminescence (BL). Indeed, the aim of the project consists in the synthesis of the breakable shell around the enzyme that can be released from the stimulus-responsive container once internalized into cells [21]. The natural reducing environment of cancer cells, due to the presence of high concentration of glutathione, is used to induce the disruption of the shell of silica nanoparticles, which release the enzyme for carrying out the luminescent reaction, with a consequent generation of light. (Fig3).

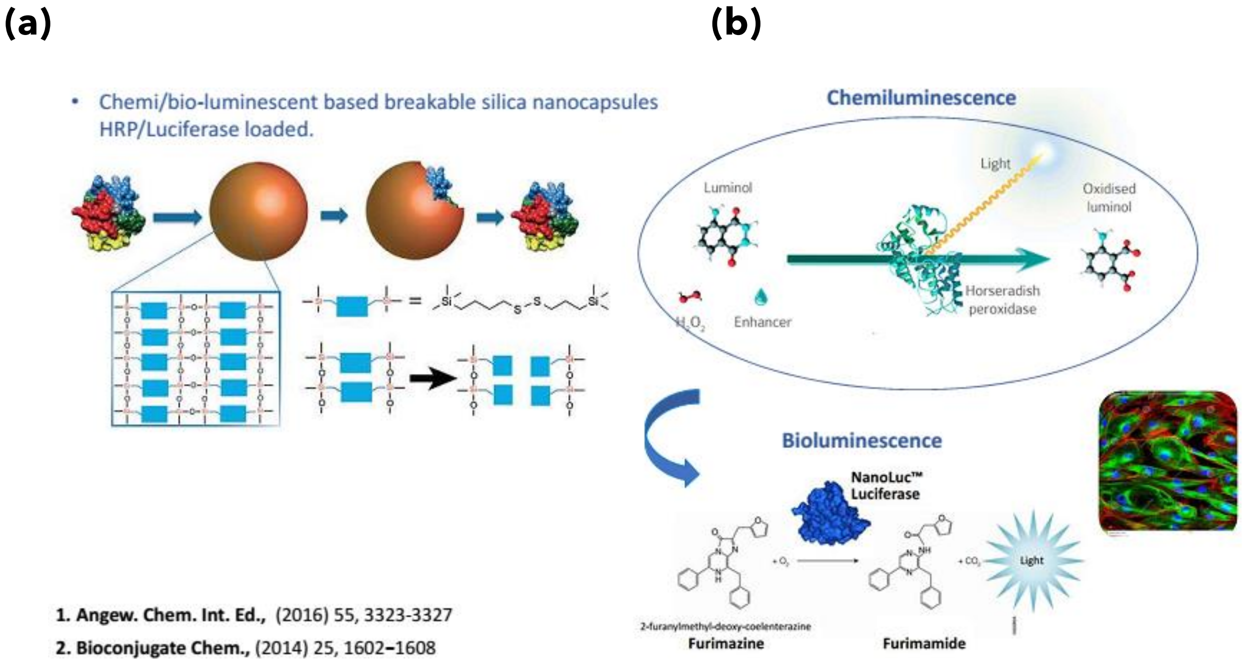

1. **Angew. Chem. Int. Ed.,** (2016) 55, 3323-3327
2. **Bioconjugate Chem.,** (2014) 25, 1602–1608

Fig3. Scheme of loading mechanism of enzymes in breakable silica nanoparticles (BNCPs).(A) Synthesis of the breakable shell around HRP enzyme that can be released from the stimulus-responsive container once internalized into cells. (B) Mechanism of Bio/Chemiluminescence reaction after the intracellular stimuli-induced break of BNCPs and following internal release of HRP or NanoLuc Luciferase.

4.2 SYNTHESIS AND CHARACTERIZATION

4.2.1 Synthesis of Breakable Silica Nanocapsules

Breakable Silica Nanocapsules (BNCPs) were synthesized by a reverse microemulsion procedure. Typically, 7.5 mL of cyclohexane as the oil phase, 1.77 mL of CA-520 as a surfactant, and 1.8 mL of n-hexanol as a co-surfactant were mixed as well as magnetically stirred with a stir bar at 350 rpm. After that, 300 μL of D.I. water and tetraethyl orthosilicate (TEOS) (40 μL) as silica agent mixed with 60 μL of bis[3-(triethoxysilyl)propyl] disulfide (BTEPDS) were added to the mixture at room temperature, generating a water-in-oil (w/o) microemulsion system. Next, 50 μL of aqueous ammonia (35 wt%) was introduced into the system and stirred overnight at room temperature. After, 95% ethanol was added to destabilize the microemulsion system and the breakable silica nanoparticles (BNCPs) were collected by centrifugation at

40,000 rcf for 20 min and washed with 95% ethanol and water several times. Finally, the BNCPs were suspended and kept in 99.5% ethanol.

4.2.2 Synthesis of HRP Peroxidase loaded Breakable Silica Nanocapsules

The synthesis HRP Breakable Silica Nanocapsules (HRP@BNCPs) is slightly modified replacing 300 μL of D.I. water with 300 μL of HRP aqueous solution (1.5 mg/mL). After synthesis, HRP@BNCPs were kept in D.I. water at 4 °C (Fig4).

4.2.3 Synthesis of HRP+Luminol loaded Breakable Silica Nanocapsules

The synthesis HRP+Luminol Breakable Silica Nanocapsules (HRP+LUM@BNCPs) is slightly modified replacing 300 μL of HRP aqueous solution with 150 μL of HRP (1 mg/mL) and 150uL of luminol aqueous solution (1 mg/mL). After synthesis, HRP+LUM@BNCPs were kept in D.I. water at 4 °C.

4.2.4 Synthesis of No Breakable Silica Nanocapsules

No Breakable Silica Nanocapsules (NoBNCPs) were synthetized modifying slightly the above procedure: 300 μL of D.I. water was mixed with TEOS (100 μL) as silica agent instead of bis[3-(triethoxysilyl)propyl] disulfide.

4.2.5 Synthesis of HRP Peroxidase loaded No Breakable Silica Nanocapsules

The synthesis protocol of HRP loaded No Breakable Silica Nanocapsules (HRP@NoBNCPs) was slightly modified mixing 300 μL of HRP aqueous solution (1.5 mg/mL) with TEOS (100 μL) as silica agent, in place of bis[3-(triethoxysilyl)propyl] disulfide.

4.2.6 Synthesis of NanoLuc Luciferase loaded Breakable Silica Nanocapsules

The synthesis NanoLuc Breakable Silica Nanocapsules (NanoLuc@BNCPs) was carried out replacing 300 µL of D.I. water with 300 µL of NanoLuc aqueous solution (1.5 mg/mL). After synthesis, NanoLuc@BNCPs were kept in D.I. water at 4 °C

4.2.7 Synthesis of NanoLuc Luciferase loaded No Breakable Silica Nanocapsules

The synthesis protocol of NanoLuc loaded No Breakable Silica Nanocapsules (NanoLuc@NoBNCPs) consists in mixing 300 µL of NanoLuc aqueous solution (1.5 mg/mL) with TEOS (100 µL) as silica agent, in place of bis[3-(triethoxysilyl)propyl] disulfide.

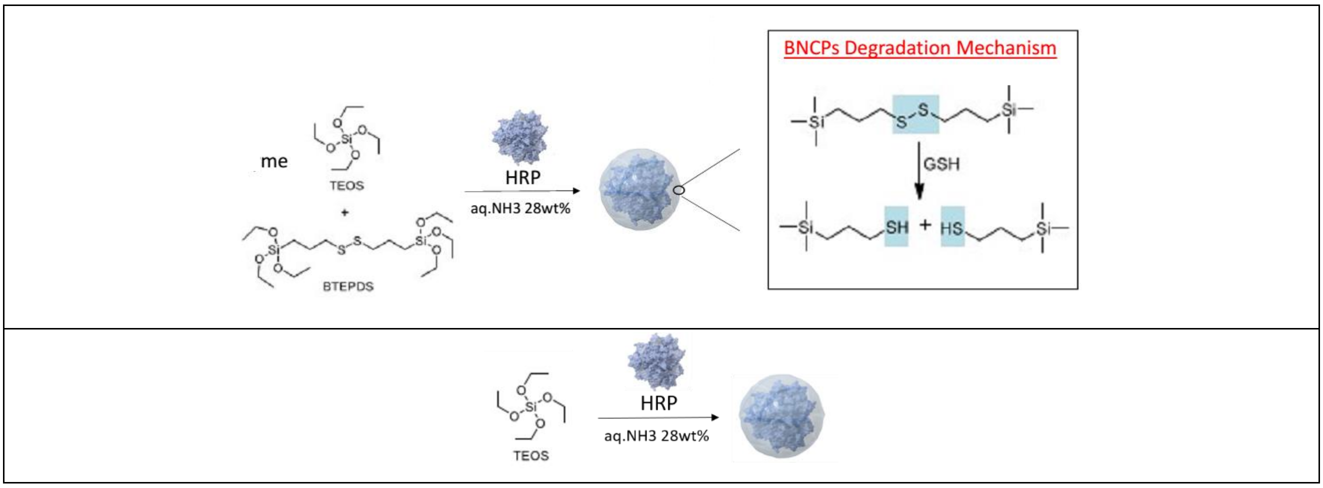

Fig4. (Top) Synthesis of the breakable silica nanocapsules. The enzyme is encapsulated within a breakable hybrid shell that comprises disulfide bridges embedded in a silica network. (Bottom) Synthesis of the No breakable silica nanocapsules, loaded with HRP peroxidase.

4.2.8 Characterization

HRP loaded breakable organosilica nanocapsules (HRP@BNCPs) as shown in the SEM pictures (Fig5) are well defined, uniform in size, possessing a diameter around 100 nm. A similar size (150 nm) was measured by dynamic light scattering measurements on a suspension of the capsules in water.

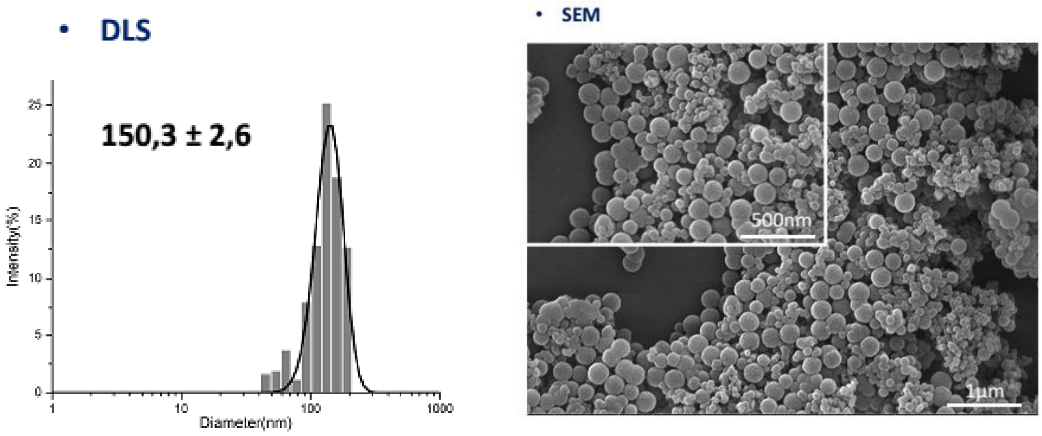

- **Zeta Potential**

HRP@BNCPs	-40,25 ± 0,43 mV
Blank@BNCPs	-18,65 ± 1,66 mV

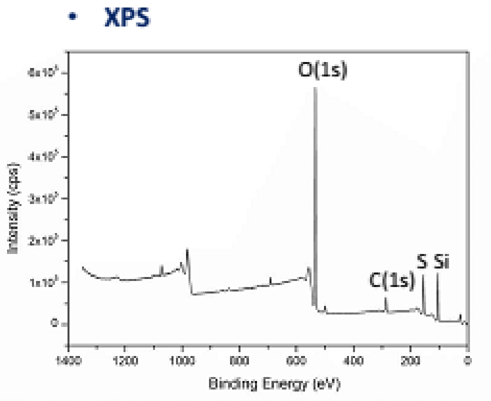

Fig5. (Top, left**)** Size distribution profile in deionized water, scanning electron microscope (SEM) image (top, right) (bottom, left) Zeta potential and X-ray photoelectron spectroscopy (XPS) of HRP@BNCPs.

Zeta potential analyses performed at room temperature are shown in Table "Zeta Potential" reported in Fig5. Also, the zeta potential measurements put in evidence the encapsulation of HRP, performed in water (pH ~ 6.5), which showed successful charge conversion of the negatively charged enzyme HRP@BNCPs, as compared with Blank@BNCPs control nanoparticles. The effective incorporation of the disulfide linker was proven by X-ray photoelectron spectroscopy (XPS). XPS survey spectra showed the presence of C(1s) and S(1s) signals at 285 and 187 eV.

4.3 RESULTS AND DISCUSSION

4.3.1 Enzyme Efficiency Encapsulation

As can be seen from FT-IR spectra of samples Blank@BNCPS (filled just with water), HRP@BNCPs (loaded with the enzyme) and free HRP enzyme, the C=O stretching vibration peak appears at 1548 cm^{-1} and 1657cm^{-1}. This peak is probably due to the presence of the enzyme, as shown by free HRP enzyme spectra. An overlap occurs between BNCPs@HRP and free HRP spectra, indicating that enzyme was successfully loaded. The stretching vibration peaks of Si–O–Si appear at 1089 cm^{-1} and 1190 cm^{-1}, respectively. The symmetric stretching vibrational peak of Si–OH appears at 970 cm^{-1} and the characteristic peak of Si–O bond appears at 455 cm^{-1}. TGA analysis was employed to calculate the content of HRP inside breakable silica nanocapsules (HRP@BNCPs). HRP@BNCPs degradation occurred in two steps. The first degradation step (at 98 °C) can be attributed to the disulfide linker aliphatic chains evaporation combined with the degradation of the enzyme absorbed on the external polymeric network. The second thermal event, with a weight loss of 10%, can be assigned to the degradation of the HRP enzyme encapsulated inside the nanoparticles (Fig.6).

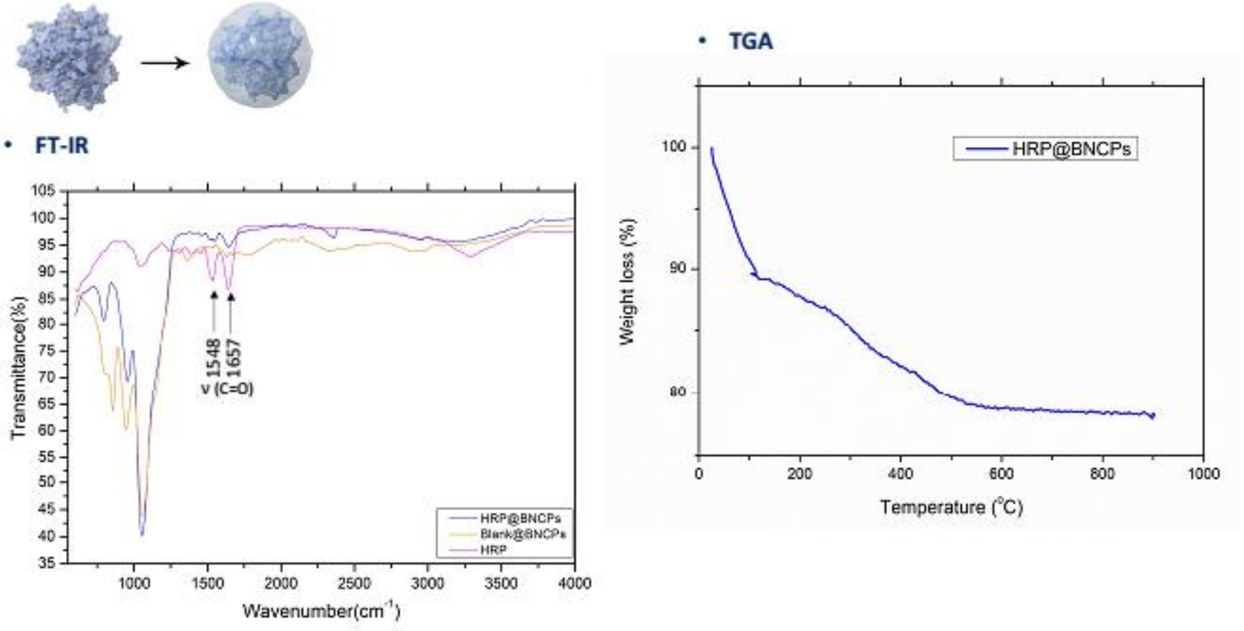

Fig.6. Infrared (FT-IR) characterization of Blank@BNCPs (filled just with water), HRP@BNCPs (loaded with the enzyme) and free HRP enzyme. TGA analysis of HRP breakable nanocapsules (HRP@BNCPs).

In order to investigate the efficiency of HRP loading, fluorescent dye (RITC)-labeled HRP was prepared. First, a mixture comprised of HRP (6 mg in 500 µL of D.I. water) and Rhodamine B isothiocyanate (RITC, 3 mg in 350 µL of DMSO) was stirred under dark conditions for 24 h at 4 °C. After that, the mixture was transferred to a dialysis membrane composed of regenerated cellulose with a molecular weight cut-off of 20 kDa. Then, to remove the unreacted RITC, the dialysis bag was dialyzed against 1 L of D.I. water and gently stirred for 3 days. Finally, the RITC-labeled HRP (designated RITC-HRP) was used to synthesize RITC-HRP@BNCPs. The absorbance intensity of the RITC-HRP@BNCPs was measured by suspending the nanoparticles in 2M NaOH for 20 minutes at room temperature, and the amount of encapsulated RITC-HRP released (0,6mg/mL) (Fig. 7a) was determined according to a calibration curve established by plotting the absorbance versus the concentration of native RITC-HRP under the same conditions (Fig. 7b) and Encapsulation efficiency was calculated using below formula:

$$Encapsulation\ Efficiency(\%) = \frac{mass\ of\ HRP@RITC\ in\ BNCPs}{initial\ mass\ of\ HRP@RITC} = 20$$

a)

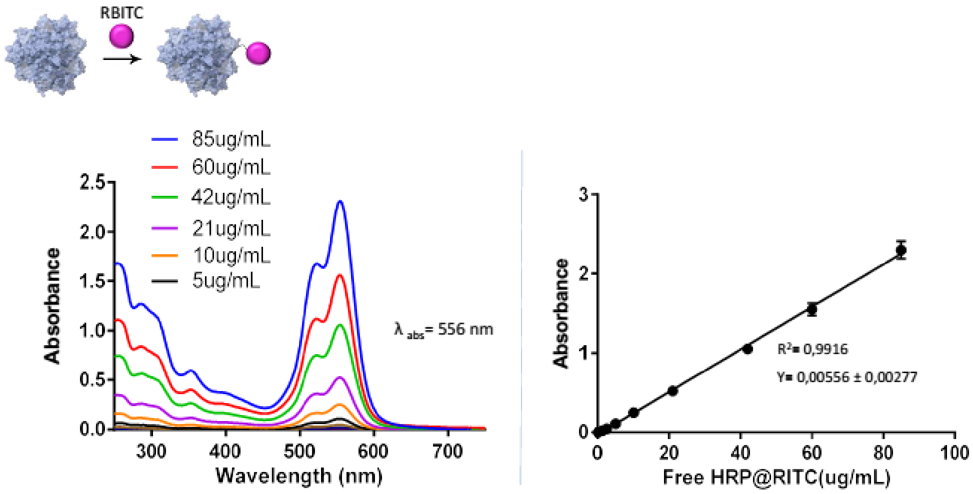

b)

Enzyme Encapsulation Efficiency

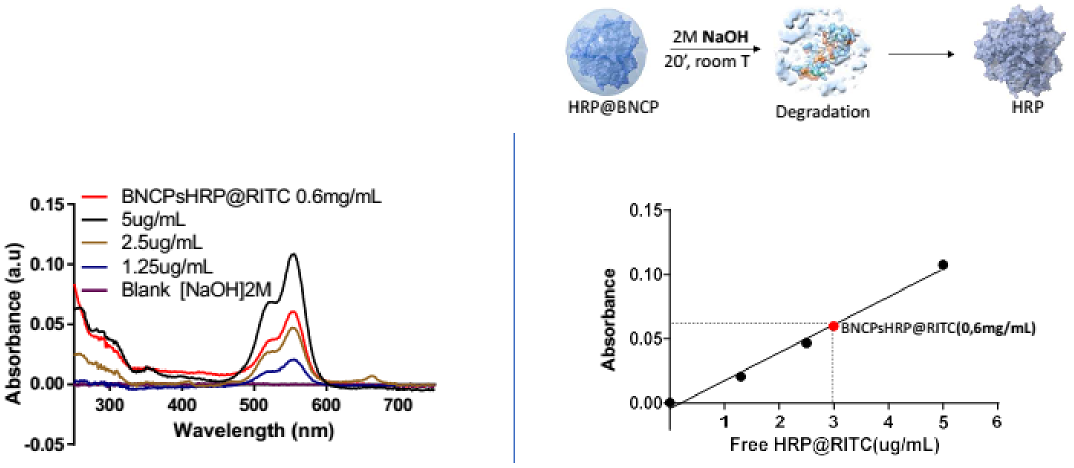

$$\text{Encapsulated Efficency (\%)} = \frac{\text{mass of HRP@RITC in BCNPs}}{\text{initial mass of HRP@RITC}} = 20$$

Figure7. Calibration curve of absorbance versus rhodamine B isothiocyanate (RITC)-horseradish peroxidase (HRP). (A) On the left, absorbance spectra of different concentrations of RITC-HRP in 2M NaOH. On the right, the plot of absorbance intensity versus the concentration of RITC-HRP. (B) The amount of encapsulated RITC-HRP@BNCPs was measured by suspending the nanoparticles in 2 M NaOH, for 20 minutes at room temperature, and determined according to the previous calibration curve. Encapsulation efficiency was calculated.

4.3.2 Breakability Assay

4.3.2.1 STEM Analysis

In order to evaluate the release kinetics of the enzyme from the breakable nanocapsules upon their destruction, we used two samples: breakable silica nanocapsules loaded with HRP (HRP@BNCPs) and unbreakable (obtained using TEOS, without disulfide linker) silica nanocapsules loaded with HRP (HRP@NoBNCPs) as blank. Both samples were dispersed in PBS buffer solution (137 mM NaCl, 2.7 mM KCl, 10 mM Na_2HPO_4, and 1.8 mM KH_2PO_4, pH 7.4) and incubated with glutathione 5 mM at 37°C; mimicking a living cell environment. Analysis of the supernatant was performed using three approaches: Scanning Transmission Electron microscopy (STEM) analysis to investigate the morphological changes of the nanoparticles at different time treatments, colorimetric assay in order to evaluate if the enzyme was still active after the release and UV/Vis spectroscopy for the absorption of RITC-HRP released from the destroyed particles. As shown by the STEM images (Fig.8), both breakable and unbreakable HRP nanocapsules at time 0 showed uniform and well-dispersed NP formation, but after 24h hours of treatment in the presence of GSH, the HRP@BNCPs were significantly degraded whereas HRP@NoBNCPs still showed uniform size and morphology.

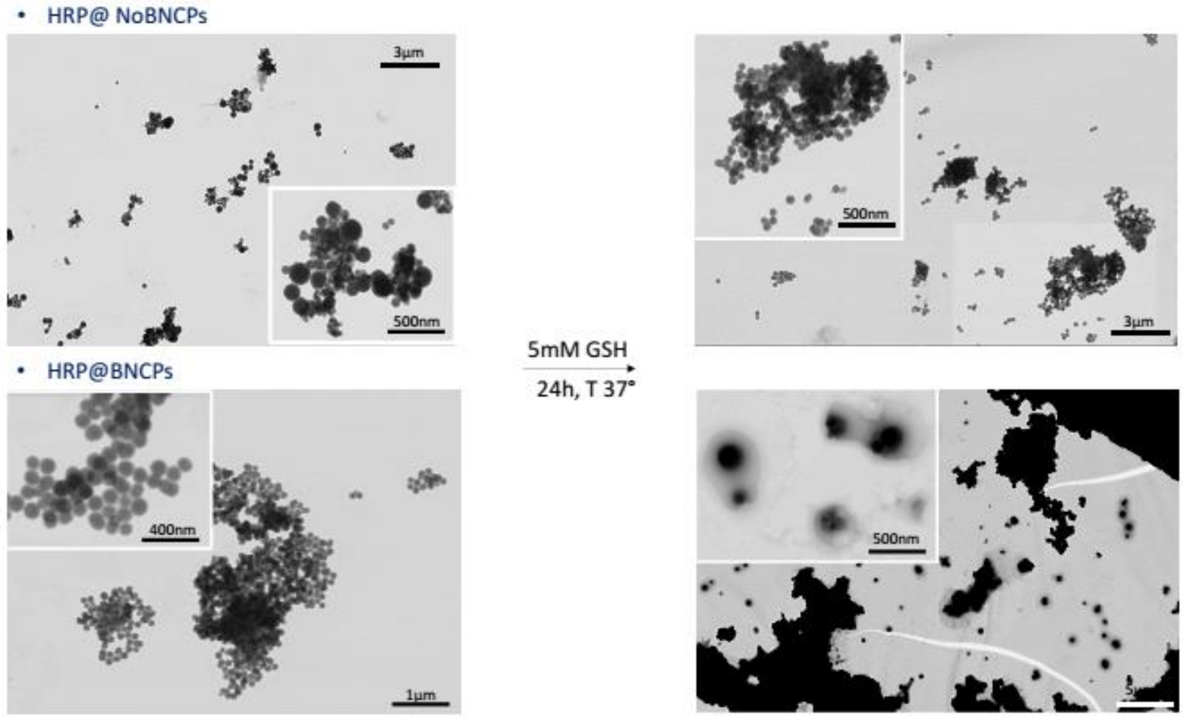

Figure8. STEM images show the morphological changes of HRP@BNCPs and HRP@NoBNCPs before and after treatment with 5 mM GSH, T 37°C (0-24 h).

4.3.2.2 Colorimetric Assay

To detect the activity of the peroxidase enzyme, a chromogenic substrate, 3,3′5,5′-Tetramethylbenzidine (TMB), was used. TMB can be converted into a coloured product when oxidized by HRP using hydrogen peroxide as oxidizing agent. First, in order to obtain the HRP calibration curve, various concentrations of native HRP were prepared in PBS buffer (137 mM NaCl, 2.7 mM KCl, 10 mM Na_2HPO_4, and 1.8 mM KH_2PO_4, pH 7.4) and citrate buffer (0,05M; pH 5.2). Then, each sample (20µL) was supplemented with 40 µL of the TMB solution (10 mM in DMSO) and 40 µL of H_2O_2 (10 mM in D.I. water). After 30 minutes the colorimetric reaction was stopped using sulfuric acid (2M). In order to test the HRP native structure stability in presence of GSH (5 mM), a colorimetric kinetic measurement was performed, following the same conditions as indicated above. The reaction was monitored by measuring the absorbance at 450 nm using a microplate reader (Fig 9a).

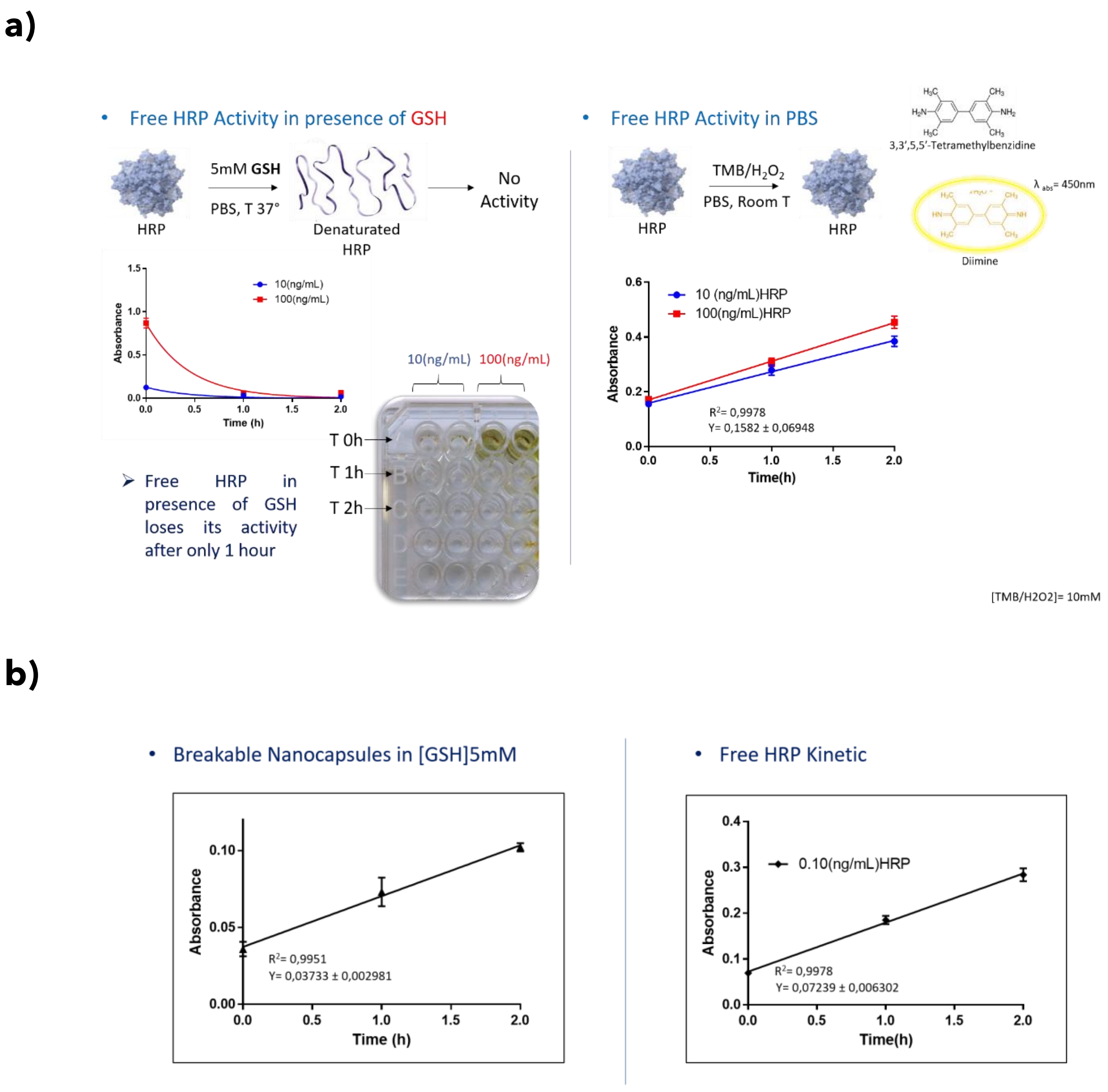

- Free HRP in presence of GSH loses its activity after only 1 hour

$$\text{Enzyme Activity (mUI/mL)} = \frac{\Delta Abs \times V \times 1000}{\min \times \varepsilon \times d \times v}$$

Relative Enzyme Activity (%) = 30 %

Fig.9 (A) Colorimetric kinetic curves of the free HRP enzyme in the presence of 5 mM GSH and in PBS buffer. **(B)** Colorimetic enzyme activity of native HRP (on the right) and HRP released from breakable silica nanocapsules after GSH [5 mM] treatment.

As shown in Figure 9a, a maximum enzymatic activity of a HRP solution (100 ng/mL) was monitored. Upon addition of glutathione, after one hour, a dramatical signal decrease was detected, probably due to enzyme degradation. After two hours, the signal reached a plateau, thus suggesting that almost of the overall enzyme was inactivated. As control experiment, a colorimetric kinetic measurement was performed using the same amount of the native enzyme (10 and 100 ng/mL) in PBS buffer (137 mM NaCl, 2.7 mM KCl, 10 mM Na_2HPO_4, and 1.8 mM KH_2PO_4, pH 7.4). As shown by the graph, the enzyme is still active even after two hours. The encapsulated enzyme, upon GSH treatment, maintains 30% of native activity compared with HRP in standard conditions. This value is probably due to the presence of glutathione which might interfere with the oxidation colorimetric reaction.

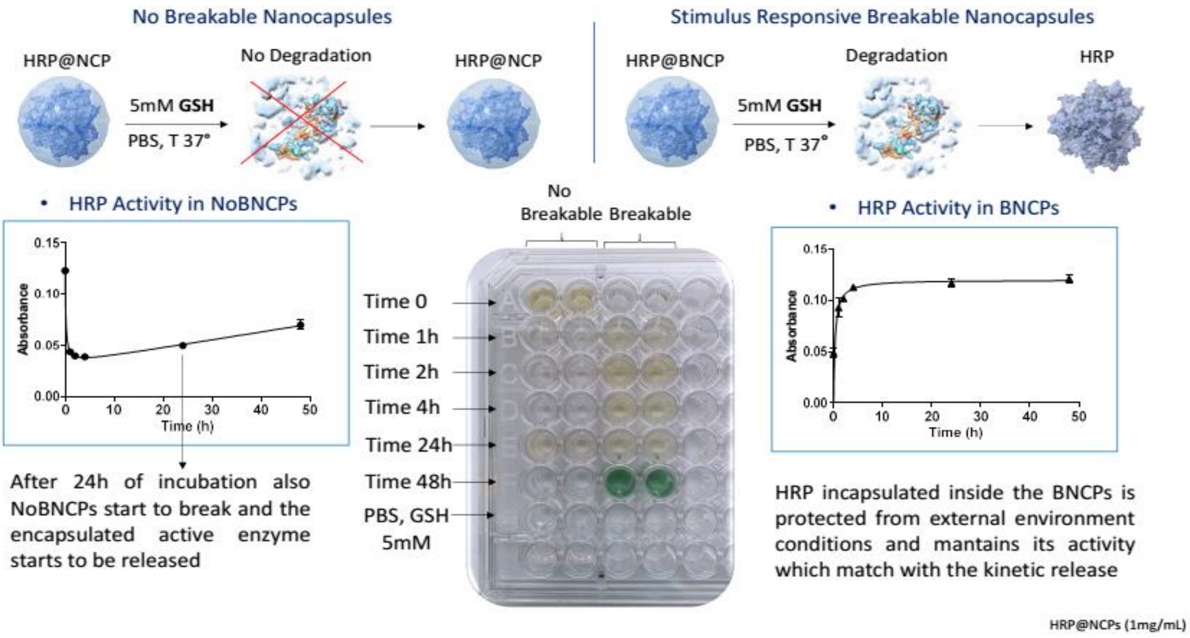

After 24h of incubation also NoBNCPs start to break and the encapsulated active enzyme starts to be released

HRP incapsulated inside the BNCPs is protected from external environment conditions and mantains its activity which match with the kinetic release

Fig.10 Kinetic profiles of HRP released from No Breakable silica Nanocapsules (HRP@NoBNCPs) (on the left) in presence of GSH [5 mM], dispersed in PBS buffer solution (137 mM NaCl, 2.7 mM KCl, 10 mM Na2HPO4, and 1.8 mM KH2PO4, pH 7.4) and incubated at 37°C with glutathione [5mM] and Stimulus Responsive Breakable Nanocapsules (HRP@BNCPs) (on the right).

To evaluate the release kinetics of enzyme from the HRP@BNCPs and HRP@NoBNCPs, upon their destruction, the particles were dispersed in PBS buffer solution (137 mM NaCl, 2.7 mM KCl, 10 mM Na_2HPO_4, and 1.8 mM KH_2PO_4, pH 7.4) and incubated at 37° C with glutathione (5 mM) mimicking a concentration present in living cells. The absorbance measurement of supernatant revealed the presence of the HRP amount released from the destroyed particles. The results summarized in Figure10 show that at time=0 there is no signal corresponding to an amount of the enzyme released from

HRP@BNCP to solution. The signal observed at time 0, before the addition of glutathione, of the control sample HRP@NoBNCPs (in which we encapsulated the same amount of HRP used for HRP@BNCPs) show a nonspecific adsorption of the enzyme on the external shell network which is not shown in HRP@BNCPs. In HRP@NoBNCPs after 1hour, a dramatically signal decrease appeared probably due to the proteolysis of the adsorbed enzyme, degraded by the GSH in the environment. On the contrary, HRP@BNCPs starts to show a faint colorimetric signal generated by the enzyme released from the disruption of silica shell. The signal then increased overtime, as the HRP left the broken capsules and dissolved into solution. After 24h, the signal reached a plateau, thus suggesting that almost the overall enzyme release took place in one day (Figure10). The non-breakable capsules (HRP@NoBSNPs) did not show any release of enzyme amount in solution even after 48h treatment (Figure10). According to the results obtained, the encapsulation strategy provides additional protection for HRP against external environment conditions, while preserving its functional nature without compromising the biological activity. Furthermore, the excellent physical rigidity and chemical stability of BNCPs could provide protection to the encapsulated proteins/antibodies and minimize their undesired cytosolic release.

4.3.3 Chemiluminescence Assay

We examined the luminescence properties of HRP@BNCPs and HRP+Lum@BNCPs (0.6 mg/mL) under the same conditions. As expected, upon addition of the commercial chemiluminescent substrate (mixture 1:1 of H_2O_2+Luminol), HRP+LUM@BNCPs showed higher chemiluminescent signal than HRP@BNCPs, probably due to the presence of encapsulated luminol. The luminescence intensity of the HRP@BNCPs/ HRP+Lum@BNCPs was measured by suspending the nanoparticles in 2 M NaOH for 20 minutes at room temperature, and the activity of encapsulated HRP released was determined adding the substrates. (Fig.11).

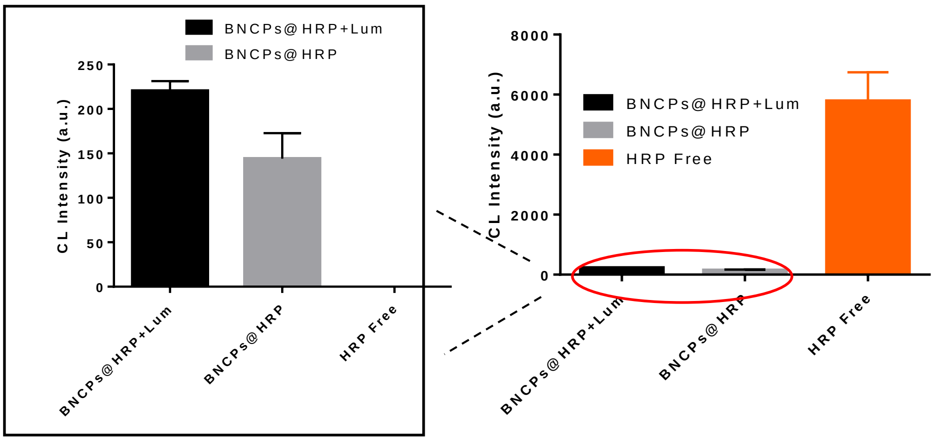

Fig11. Chemiluminescence intensities histogram of breakable silica nanocapsules loaded with HRP (HRP@BNCPs) and breakable silica nanocapsules loaded with HRP and luminol (HRP+Lum@BNCPs) in the presence of Thermo Scientific chemiluminescent substrates.

In order to investigate if small molecules, like luminol and H_2O_2, were able to cross the silica shell and carry out chemiluminescent reaction, we performed the "permeability measurement" using unbroken HRP@BNCPs and HRP+Lum@BNCPs nanocapsules in the presence of luminol plus H_2O_2, and H_2O_2 only, respectively. Unexpectedly, we observed no chemiluminescent signal of HRP+Lum@BNCPs in the presence of saturated concentration of hydrogen peroxide, whereas the HRP@BNCPs (in the presence of equimolar concentrations of H_2O_2 and luminol) showed high chemiluminescent intensity, as shown in figure 12. According to results obtained, the kinetic profile of HRP encapsulated in BNCPs resulted constant over time and calibration curve for H_2O_2 was performed.

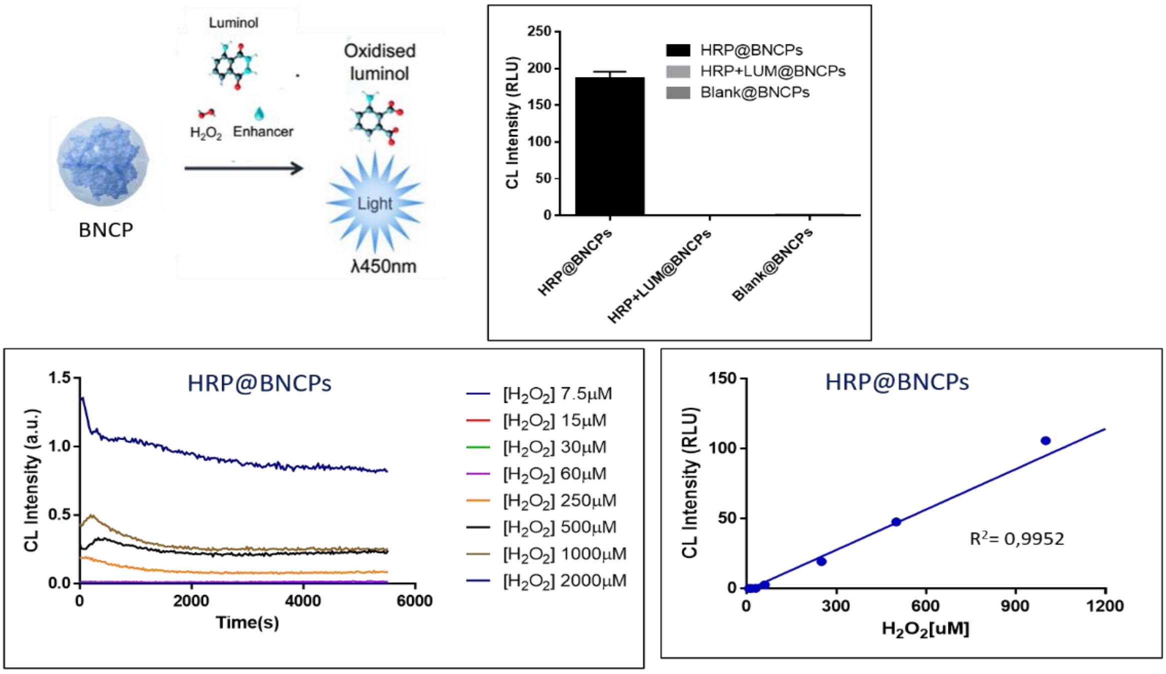

BNCPs (0,6mg/mL)
Luminol (5mM)

Figure12. (Top, left) Sketch of permeability measurement. CL reaction of unbroken HRP@BNCPs and HRP+Lum@BNCPs nanocapsules in the presence of mix 1:1 of luminol/ H_2O_2, and H_2O_2 only. Top, on the right, chemiluminescent signal collected for all different types of breakable silica nanocapsules (HRP@BNCPs, HRP+Lum@BNCPs, Blank@BNCPs). Bottom, on the left, kinetic profile of HRP@BNCPs, on the right the calibration curve obtained using HRP@BNCPs for H_2O_2 detection

4.3.4 Bioluminescence Assay

Assuming that small molecules are able to cross silica shell, we investigated if encapsulated NanoLuc luciferase was still active after breakable silica nanocapsules synthesis process and if it was still able to carry out the bioluminescence reaction. According to the results shown in figure 14, in the presence of the furamizine substrate both encapsulated NanoLuc and native NanoLuc showed the same bioluminescent signal and stable catalytic activity over time. Bioluminescence measurements were performed using 0.6 mg/mL of breakable silica nanocapsules loaded with NanoLuc (NanoLuc@BNCPs) 20 μL in the presence of furimazine (80μL).

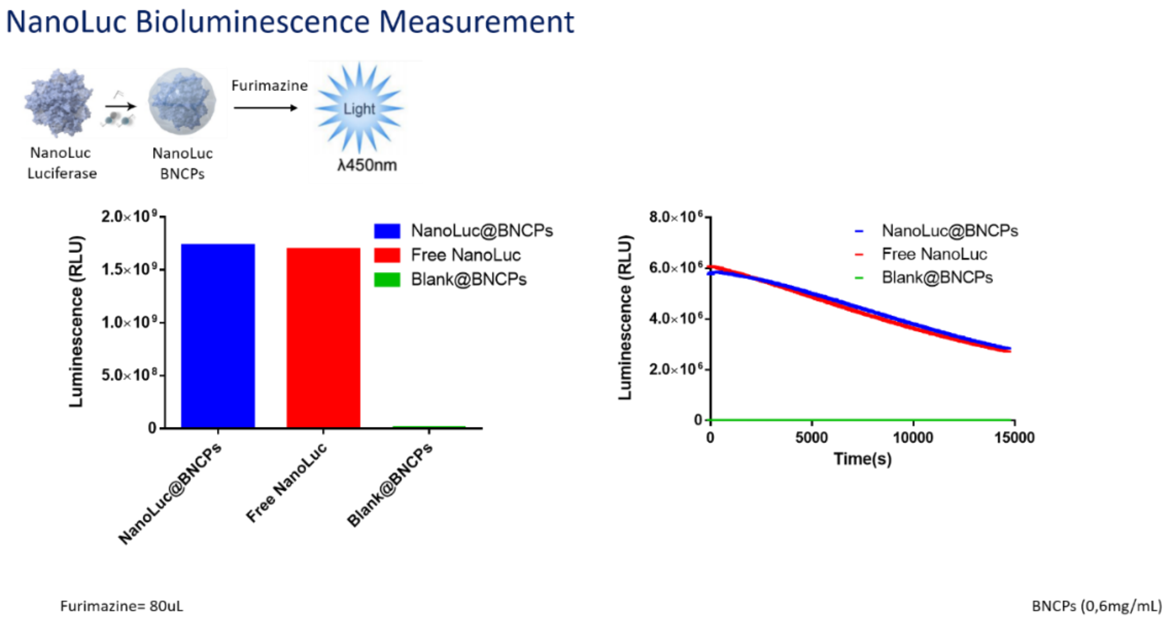

Fig.14. Schematic representation of bioluminescence reaction. Breakable silica nanocapsules loaded with NanoLuc luciferase (NanoLuc@BNCPs) in the presence of the substrate, furimazine, showed the same bioluminescent signal of the native NanoLuc. The kinetic profile showed the same catalytic activity over time.

As shown in Figure 14, the synthesis procedure has not affected NanoLuc enzyme catalytic activity, which preserves its native functionality comparable with the catalytic activity of the free enzyme resuspended in PBS buffer solution (137 mM NaCl, 2.7 mM KCl, 10 mM Na_2HPO_4, and 1.8 mM KH_2PO_4, pH 7.4).

4.4 CONCLUSIONS

In conclusion, we have proposed a general method for the encapsulation of proteins within a stimulus-responsive breakable hybrid organosilica shell and the released enzymes retained their activity. The shells of silica HRP@NCPs are permeable to small molecules, such as the enzyme substrates, which allows them to react with large enzyme payloads in the cavity of the nanocapsules. Because the concentration and location of H_2O_2 in eukaryotic cells strongly rely on the types of cells, and cellular compartments (hollow nanosilica), specific targeting of tumor cells or organelles could further be achieved by surface modification of HRP@BNCPs with monoclonal antibodies or peptides.

REFERENCES

1 H. Kang, S. Mintri, A. Menon, H. Y. Lee, H. S. Choi, J. Kim, Nanoscale, 2015, 45, 18848–18862

2 P. Yuan, X. Mao, X. Wu, S. S. Liew, L. Li, S. Q. Yao, Angew. Chem., 2019, 131, 7739-7743

3 C. Yu, L. Qian, J. Ge, J. Fu, P. Yuan, S. C. L. Yao 1, S.Q. Yao, Angew. Chem. Int. Ed., 2016, 55, 9272-9276

4 C. C. Wu, Y.Hu, M. Miller, R. V. Aroian, M. J. Sailor, ACS Nano, 2015,9, 6158-6167

5 P. Khan, D. Idrees, M. A Moxley, J. A Corbett, F. Ahmad, G. V. Figura, W. S. Sly, A. Waheed, M.D.I. Hassan, Appl Biochem Biotechnol., 2014, 173, 333–355.

6 L.S.A. Busa, M. Maeki, A. Ishida, H. Tani, M. Tokeshi, Sensor Actuat B.chem., 2016, 236, 433-441

7 L. R. Domingo, M. R. Gutiérrez, P. Pérez, Molecules, 2018, 259, 748-750

8 D. E. J. G. J. Dolmans, D. Fukumura, R. K. Jain, Nat. Rev. Cancer, 2003, 3, 380–387

9 F. Song, Y. Li, S. Wang, L. Zhang, Q. L. Chen, New J. Chem., 2019, 43, 17284-17297

10 D. A. Hammoud, J.Nucl. Med., 2016, 57, 1161–1165

11 H. Chen, W. Zhang, G. Zhu, J. Xie, X. Chen, Nat. Rev. Mater., 2017, 2, 17024

12 S. Wilhelm, A. J. Tavares, Q. Dai, S. Ohta, J. Audet, H. F. Dvorak, W. C. W. Chan, Nat. Rev. Mater., 2016, 1, 16014

13 S. S. Lucky, K. C. Soo, Y. Zhang, Chem. Rev., 2015, 115, 1990–2042

14 A. Master, M. Livingston, A. S. Gupta, J.Control. Release, 2013, 168, 88–102

15 Y. Shen, A. J. Shuhendler, D. Ye, J. J. Xua, H. Y. Chen, Chem. Soc. Rev., 2016, 45, 6725–6741

16 N. M. Idris, M. K. Gnanasammandhan, J. Zhang, P. C Ho, R. Mahendran, Y. Zhang, Nat. Med., 2012, 18, 1580–1585

17 J. He, Y. Wang, M. A Missinato, E. Onuoha, L. A Perkins, S. C. Watkins, C. M. St. Croix, M. Tsang, M. P. Bruchez, Nat. Methods, 2016, 13, 263–268

18 H. Yuan, H. Chong, B. Wang, C. Zhu, L. Liu, Q. Yang, F. Lv, S. Wang, J.Am. Chem. Soc., 2012, 134, 13184–13187

19 Y. R. Kim, S. Kim, J. W. Choi, S. Y. Choi, S. H. Lee, H. Kim, S. K. Hahn, G. Y. Koh, S. H. Yun, Theranostics, 2015, 5, 805–817

20 C. Y. Hsu, C. W. Chen, H. P. Yu, Y. F. Lin, P. S. Lai, Biomaterials, 2013, 34, 1204–1212

21 E. A. Prasetyanto, A. Bertucci, D. Septiadi, R. Corradini, P. Castro-Hartmann, L. De Cola, Angew Chem Int Ed Engl., 2016,55, 3323-7

5

A CHALLENGE IN BIOSENSORS: IS IT BETTER TO MEASURE A PHOTON OR AN ELECTRON FOR ULTRASENSITIVE DETECTION?

Reproduced from: "A challenge in biosensors: Is it better to measure a photon or an electron for ultrasensitive detection?"
Aldo Roda, Fabiana Arduini, Mara Mirasoli, Martina Zangheri, Laura Fabiani, Noemi Colozza, Elisa Marchegiani, Patrizia Simoni, Danila Moscone
Biosensors and Bioelectronics, 2020,155, 112093
Reproduced by permission of The Royal Society of Chemistry
https://www.sciencedirect.com/science/article/pii/S0956566320300907

5.1. INTRODUCTION

Nowadays basic research in biosensors is oriented to achieve ultrasensitive detection combined with fast response time, cost-effectiveness, and portability. The WHO has established that an effective diagnostic test shall fulfil the ASSURED criteria, where ASSURED means: Affordable (by those at risk of infection), Sensitive (low false-negatives), Specific (few false-positives), User-friendly (simple to perform and requiring minimal training), Rapid (to give useful information at first visit) and Robust (do not require refrigerated storage), Equipment-free, Delivered to those who need it. In the attempt to reach these goals, many incredible advances in the field of biosensors have been achieved over the past decade, underpinned by a variety of solutions to boost sensitivity and selectivity. From the commercial and diagnostic point of view, two fantastic successes have boosted the market penetration of biosensors, paving the way for point-of-care testing (POCT). In 1980, miniaturised electrochemical glucose biosensors, such as Glucopen or similar devices, opened a new era in the diabetes management, enabling for the first time the patient to autonomously measure at home his glucose in blood, with high impact on his quality of life and on cost in charge of the National Health Service. Another biosensor playing a leading role in POCT market is the lateral flow immunoassay (LFIA)-based pregnancy test, first released by Clearblue in 1988, which employs nanoparticles for a color-based visual readout. While for glucose detection high assay sensitivity was not the main issue, being glucose present in blood at millimolar levels, high detectability for urinary human chorionic gonadotropin was fundamental to early establish pregnancy (Campbell et al., 1987).

In the subsequent decades, there has been an explosion of biosensing related technologies, taking advantages of new (nano)materials, advanced protein chemistry and molecular biology, protein immobilisation procedures and modern approaches to signal transduction, associated with any kind of electronics and microfluidics to assist the biosensor format. A large number of papers have been published in the last twenty years, exploiting different transduction principles, from electrochemical (such as conductometric, voltammetric, potentiometric, amperometric, and impedimetric detection), through optical (including absorbance/reflectometry, photoluminescence, bio-chemiluminescence (BL/CL), and thermochemiluminescence), hybrid photon-electron systems (such as electrogenerated chemiluminescence (ECL) and photoelectrochemistry), up to label-free formats (including for example surface plasmon resonance principle, magnetic, calorimetric, acoustic, and mass sensitive detection principles). Surprisingly, many biosensor principles just represent elegant proof of concept approaches, while they are not able to achieve a wide diffusion in the market: few commercially biosensors are so far available in the market or limited to small-scale distribution by start-up high-tech companies. The main barriers are not only related to the biosensor per se, but mainly to problems in managing quality control of the data, robustness of the devices and all the related certified procedures requested in the clinical chemistry field. We are in a sort of stagnant situation: many small size enterprises already developed new biosensors but with problems to enter in the medical market, thus hampering the urgent need of diagnosis of many pathologies requiring the sub-picomolar detection of specific biomarkers and the therapeutic monitoring of pharmacological therapies, particularly in the era of precision medicine. This is the emerging field that should stimulate new commercial opportunities for the near future of biosensing technologies already established and optimized, but still orphan. If we enter in more details in the transduction technologies, electrochemistry dominated in the early years, and the biosensors world was often identified with the electrochemical ones. Moreover, this principle is still the most used in basic and applied research. In the research field, second to electrochemical biosensors are those based on optical/luminescence transduction and particularly on chemical luminescence including ECL and CL, which potentially combine high detectability with instrumental simplicity and low cost. The competition among various transducing principles is very strong in terms of detectability and analytical format, and the different claims reported by the authors do not allow understanding which transduction technologies offer the best potential analytical performance to achieve the highest detectability combined with device simplicity/robustness often requested for new generation biomarker detection assays. Indeed, the intercomparison between different detection principles described in the literature is often affected by differences in the assay format regarding the molecular recognition elements (such as antibody affinity and specificity, enzyme kinetics and catalysis) and assay conditions involving biomolecules immobilisation, materials, microfluidic-based formats, etc. To achieve a realistic and accurate evaluation of the potentiality of electrochemistry and CL (i.e., is it better to "measure an electron or a photon"?), we engaged a collaboration between two research groups, well-recognized experts respectively in electrochemistry and CL-based biosensing. With this aim, biosensors were built up by the two groups in the same analytical format, sharing the same biospecific reagents and protocols. For a wide range and accurate comparison, the challenge was carried out using some biosensor formats widely employed in analytical chemistry, from enzymatic to immunological based biosensors. Horseradish peroxidase (HRP) activity and hydrogen peroxide concentration were measured, being these two molecules used in many coupled enzymatic reactions, and the enzyme often used as a label for affinity binding biosensors. Glucose was also included in the comparative study, since the only well-established widely commercially available biosensor is the electrochemistry-based one for glucose detection in blood; however, paper-based sensors were utilised, in order to realize new sustainable devices. Finally, we set up a model sandwich-type immunoassay for rabbit immunoglobulin G (IgG) detection using a specific antibody immobilized on magnetic beads and a secondary HRP-labeled antibody. Each assay was evaluated employing two biosensor device apparatuses: a bench-top instrumentation and a portable miniaturised format. The obtained results should allow to accurately establish the "winner transduction technology" between the two competitors, which provides the lowest detection limit and highest sensitivity and dynamic range, combined with simplicity and amenability for miniaturization and short analysis time. A suggested allocation of the two principles in different complementary application areas according to their analytical performance will be also reported and discussed. The final goal was to define the potentiality of the two approaches, offering a useful tool to the scientific community for driving the choice in selecting a most suitable biosensor format for the introduction in the market for a given specific need.

5.2. AN UPDATE ON FUNDAMENTALS OF ANALYTICAL CHEMILUMINESCENCE AND ELECTROCHEMISTRY

5.2.1. Fundamental Update In Analytical Chemiluminescence

Chemiluminescence (CL) is the light emission generated by a chemical reaction, in which a singlet chemi-excited (intermediate) product emits a photon (or undergoes energy transfer to a fluorescent acceptor in indirect CL) while decaying to the electronic ground state. Since the first luminol-based CL system was reported (Albrecht, 1928), several CL substrates, such as lucigenin, lophine, acridinium/acridan esters, peroxyoxalates, and 1,2-dioxetanes, have been proposed and employed for developing ultrasensitive bioassays. Many known CL systems rely on oxidation-dependent mechanisms, in which a four-membered ring peroxide intermediate (1,2-dioxetane or 1,2-dioxetanone) is formed. These are intrinsically unstable strained heterocyclic compounds bearing the relatively weak O─O bond, which decomposition is exergonic enough to produce carbonyl compounds in the electronic singlet excited state. In other CL systems, first introduced by Schaap in 1987, light emission is chemically- or enzymatically triggered by removal of a phenol-protecting group from a stable adamantylene-dioxetane derivative. The resulting phenolate decomposes via an intramolecular chemically initiated electron exchange luminescence (CIEEL) with photon emission (Schaap et al., 1987). Chemiluminescence-based biosensors can also rely on the CL resonance energy transfer (CRET) principle, which involves a non-radiative (dipole-dipole) energy transfer occurring between a CL donor and an energy acceptor (either a fluorophore or a quencher). As this phenomenon only occurs when donor and acceptor are in close proximity (<10 nm), it provides a powerful tool for the sensitive detection of molecular binding events, similarly to the more common fluorescence RET phenomenon. Compared with fluorescence, probably the most diffused luminescence-based detection approach, CL shares the same S1–S0 radiative decay, but generally yields much weaker signals and therefore it requires sensitive light detectors, such as photomultiplier tubes (PMT) or cooled back-illuminated charge-coupled device (CCD) cameras. Nevertheless, CL is characterized by a higher signal/noise ratio, being the background only due to the detector thermal and electronic noise. Indeed, the background phenomena affecting photoluminescence, such as excitation of matrix components or scattering of excitation light, are absent in CL detection. Recently, various detectors characterized by an adequate sensitivity combined with portability have been proposed, thus solving the main limitation of the relatively weak CL signal and leading to the development of ultrasensitive POCT assays. For example, BL/CL biosensors were designed exploiting new generation of (thermally cooled) back illuminated (BI) CCD (Mirasoli et al., 2018) and smartphone BI-CMOS camera (Li et al., 2019) or thin film photosensors, such as single photon avalanche photodiodes (Iinuma et al., 2016) or amorphous silicon (a-Si:H) photosensors (Zangheri et al., 2016). In addition to the fact that CL-based detection, differently from photoluminescence, cannot rely on a signal increase obtained by increasing the intensity of the photoexcitation source, the weakness of the CL emissions is due to the low CL quantum yields (ΦCL). For example, the oxidation of luminol, one of the most established CL reactions, gives rise a flash-type emission and displays under optimal conditions a ΦCL of about 1% or less in aqueous solutions. On the contrary, in the case of natural CL, i.e. bioluminescence of the well known luciferase/luciferin system, the ΦBL is higher, reaching almost 50% in optimized condition. The luminol CL reaction mechanism involves the reaction of molecular oxygen with the enol-form of luminol anion; the latter is oxidized to a cyclic peroxide which decomposes to yield 3-aminophthalate (3-amino-1,2-benzenedicarboxylic acid) in an excited state, along with a nitrogen molecule. Although the spontaneous oxidation of luminol in aqueous solution is very slow, it can be catalyzed by peroxidase enzymes, such as HRP, or other one-electron oxidants, such as metals, free radicals and a variety of nanomaterials. Due to the intrinsic advantages of CL detection in biosensing, continuous work is performed to overcome the poor efficiency of CL reactions and to produce new CL compounds with improved characteristics. Because peroxidases are poor catalysts in luminol oxidation, enhancers are added to the substrate mixture to increase light output and extend the kinetics of the reaction to a glow-type emission. The enhancer acts as a redox mediator that exchanges electrons between the peroxidase enzyme and luminol. Various molecules have been employed, such as substituted phenols, substituted boronic acids, indophenols, and N-alkyl phenothiazine derivatives. The ability of the enhancer to increase the intensity of light emission is due to two effects: increased rate of HRP turnover and reversible electron transfer between enhancer radicals and luminol. In addition to these species (primary enhancers), co-enhancers (or secondary enhancers) can significantly boost the light output by synergistic effect, probably by facilitating the action of the primary enhancer as electron transfer mediator (Sakharov and Vdovenko, 2013). Currently the most effective enhancer/co-enhancer system is 3-(10′-phenothiazinyl)propane-1-sulfonate (SPTZ) in the presence of 4-morpholinopyridine (MORP), that pushed the limit of detection for HRP down to few amol (Marzocchi et al., 2008). In recent years, some chemical indicators, such as bromophenol red or bromophenol blue, have demonstrated enhancing properties towards the HRP-luminol-H2O2 reaction. With the addition of bovine serum albumin (BSA), which may act as a secondary enhancer by stabilizing HRP, the detectability of the system has been further improved. As alternative CL systems, acridinium esters are successfully used in automated clinical chemistry immunoanalyzers offering tremendous potentiality, however they are still unexplored for biosensing applications (Nakazono et al., 2017; Ma et al., 2017). Recently, Shaap's adamantylene-dioxetane derivatives have been revisited to solve their main limitation, which is poor emission in water environment. For this purpose, new probes have been produced in which signal amplification was obtained by exploiting two approaches. In one case, the amantylidene−dioxetane was conjugated with a fluorescent acceptor that would significantly amplify the CL emission through an energy transfer mechanism, also providing shift of the emission wavelength to higher values. Alternatively, to achieve direct amplification, an electron-withdrawing group (EWG) was introduced in the molecule to increase the emissive nature of the benzoate species obtained during the chemiexcitation pathway of the probe. The efficiency of the probe was increased of more than 3 orders of magnitude with respect to standard, commercially available adamantylidene−dioxetane probes (Hananya et al., 2016). Exploiting the adamantylidene−dioxetane molecular structure, thermochemiluminescent (TCL) compounds have been recently revisited as promising labels for biosensors. In these molecules, the introduction of a fluorescent acridane moiety gave rise to self-luminescent molecules, in which light emission is simply triggered by heating (Di Fusco et al., 2015).

5.2.2. Fundamental Update In Analytical Electrochemistry

A common definition of electrochemical sensing is the measurement of an electrically measurable signal generated by the redox reaction of an electroactive substance; in case of biosensors, the substance to detect is not electroactive di per se, but can produce or be associated to another electroactive specie by means of a biological element. The reaction generally happens on the surface of a so-called working electrode, which operates in conjunction with other two electrodes, the reference and auxiliary ones, forming an electrochemical cell where the redox reaction occurs as consequence of an electric potential applied to the electrodes. The signal magnitude of the resulting current is normally associated to the analyte concentration. The principles of the electrochemistry using an electrochemical cell constituted of classical bulk electrode (e.g. platinum, gold) and Ag/AgCl/Cl− reference electrode are well known, while the most modern miniaturised and nanomaterial-based sensors can show a different electrochemical behaviour. In the frame of miniaturised sensor, screen-printing technology has revolutionized the electrochemical sensors area because of its simplicity, cost-effectivity and versatility, being able to print, in a highly reproducible manner, many materials on a variety of substrates, and making possible the production of electrodes with different geometries, even custom-made. The technology consists of printing diverse conductive and non-conductive inks on alumina and plastic substrates, but the most attractive characteristic of these sensors is the possibility to easily modify the working electrode in order to enhance its electroanalytical performances (Kadara et al., 2009; Wang et al., 1998). Passing from solid metal electrodes to the printed ones, the electrochemical performance of these latter can be not the same. From the composition point of view, the SPEs are more similar to the carbon paste electrodes, being both constituted by a carbon powder with an organic binder (Fanjul-Bolado et al., 2008). Both components can affect the properties of the electrode: the binder, being non-conductive, can decrease the effective electron transfer rate constant due to the increase in polymeric domains and the reduction in conductive pathways (Choudry et al., 2010). On the other hand, the nature and amount of the carbonaceous particles and their size (nanodimensions such as for carbon nanotubes, graphene, carbon black, etc.), the roughness factor, the presence and accessibility of graphitic edge planes also strongly affect the electrochemical behaviour of SPEs, as demonstrated by numerous papers in literature (Wang et al., 1998, 2014; Kadara et al., 2009; Wang and Musameh, 2004; Lin et al., 2004; Guan et al., 2005; Choudry et al., 2010). These characteristics, however, can be modified using several surface electrochemical or chemical pretreatment methods. These latter can increase the surface functionalities through the formation of new carbon–oxygen bonds that enhance the charge transfer, can provoke cracks that increase the roughness of the surface, can improve the wettability, reduce the extend of the organic layer and can promote a better exposure of graphite edges, improving the faradaic current. Lastly, also the printing process, especially the inks curing temperature, and the chosen electrochemical technique, can affect the performance of the SPEs (Setford et al., 1999; Morrin et al., 2003; Wang et al., 1996; Cui et al., 2001; Wei et al., 2007; Ghamouss et al., 2007). Another critical part of the SPEs is the printed reference electrode (RE). The RE is an important component of any electrochemical cell; to be efficient, a reference electrode should have a stable potential. A traditional RE is isolated from the bulk solution by a glass frit or salt bridge (Ives and Janz, 1961). In the SPEs, the reference electrode is also printed using inks containing silver and/or silver chloride and is directly exposed to the measuring solution. Because of the absence of a liquid electrolyte containing Cl−, the printed RE is considered as a pseudo-reference electrode and should be used in solutions with a fixed ionic strength, in order to avoid a shift of the working electrode potential. This phenomenon is more critical for potentiometric screen-printed sensors, however also in voltammetric techniques the stability of the reference electrode can affect the performance of the sensors. Thus, KCl should be added to the measuring solution in order to stabilise the potential of the RE (Inzelt et al., 2013). In order to obtain the best analytical performances, all the above-mentioned characteristics should be studied and tuned for the particular analyte to be detected, but the advantages of easy handling, cost-effectiveness, need for very small sample volumes often without pretreatment, portability (even wearability), of these sensors (and related instrumentation) are worth to go forward with these studies.

5.3. RECENT TECHNOLOGICAL ADVANCEMENTS TO BOOST BIOSENSORS ANALYTICAL PERFORMANCES AND PORTABILITY

During the last decades, biosensors have dramatically progressed through the introduction of novel (nano)materials and technologies, which provided new assay formats, improved figures of merit and miniaturised portable devices. Nanoscale materials such as nanoparticles (NPs), nanocluster, nanocomposites, quantum dots (QDs), carbon dots, graphene and graphene oxide (GO), as well as several nanocomposites, supply key elements for fine-tuning (bio)sensors, acting as signal amplification structures, catalysts, reductants, luminophores, energy acceptors, or bioreceptor immobilisation platforms, and also fostering the sensitivity, selectivity and stability of the developed biosensors. The trends of the last 10 years highlight graphene as the rising star in the plethora of nanomaterials employed in (bio)sensing (Cinti and Arduini, 2017). Indeed, carbon nanomaterials offer several attractive features, such as easy and efficient surface grafting and other special physical properties deriving from the unique π-π surface conjugation ability, as well as by the high number of defect sites. Graphene and its derivatives, including GO and reduced GO (rGO), are considered among the most promising materials in the twenty-first century, thanks to their astonishing features such as large surface area, thermal conductivity, room-temperature electron mobility, mechanical strength, and ease tailorability. Beyond carbon-based nanomaterials, metal NPs, such as Au NPs, Ag NPs, bimetallic NPs, and metal oxide NPs have demonstrated the capability to furnish peculiar features to biosensors, allowing for a smart detection. For instance, in case of CL detection, metallic NPs have shown to possess peroxidase-like activities enhancing the CL emission from the luminol/H2O2 system (Li et al., 2014). Moreover, they encompass their treasured electrochemical and optical properties as well as the suitability to act as labels in immunoassays, to immobilise the biocomponent, and to increase the storage stability by creating a favourable environment in both photon and electron-based biosensors. Parallel developments in microelectronic, microfluidic and printing technologies have allowed for the creation of disposable, miniaturised devices that combine various assay steps into a compact space for delivering both electrochemical and CL miniaturised biosensors with attractive features for market entry (Mazzaracchio et al., 2019; Nascetti et al., 2019). Herein, we highlight the most promising technological advancements in CL and electrochemical biosensors capable to improve the analytical features of the devices in terms of low detection limit, wide linear range, and improved robustness. In the following paragraphs, the main recent trends are highlighted, reporting several examples of CL and electrochemical biosensors, which main features are also summarized in Table 1. Examples of recently reported applications of CL and electrochemical biosensors are displayed in Fig. 1 and Fig. 2, respectively.

Table 1. Analytical performances of selected recently reported CL and electrochemical biosensors.

Analyte	Biosensing principle	Detection	Analytical features	Reference
CL-based biosensors				
Organic compounds containing hydroxyl (OH), amino (NH_2), or mercapto (SH) groups	Analytes interact with gold nanoparticles leading to a change in CL intensity	Laboratory-built flow injection CL system.	LOD: 10^{-10} mol L^{-1} Linear range: 3 orders of magnitude.	Zhang et al. (2005)
Human IgG and other proteins.	Label-free immunoassay based on multifunctionalized gold nanoparticles (MF-GNPs), obtained by successive assembly of ABEI-GNPs with antibody, bovine serum albumin (BSA) and Co^{2+}.	Microplate luminometer.	LOD: 0.13 fmol L^{-1} Dynamic range: 1.0 fmol L^{-1} to 1.0 nmol L^{-1}.	Huang et al., 2018a, Huang et al., 2018b
Cancer cells	Aptamer-based assay employing Cu/Co bimetallic manomaterials with enhanced catalytical ability as nanocatalysts for the CL reaction.	Flow injection CL system equipped with a photomultiplier.	LOD: 270 cells mL^{-1}	Li et al. (2018)
Copeptin, a surrogate marker for acute myocardial infarction.	Turn-off CRET-based sandwich immunoassay exploiting TiO_2 NPs functionalized with a porphyrin derivative and N-(4-aminobutyl)-N-ethylisoluminol and AuNPs as the CL emitter and energy acceptor, respectively.	Microplate luminometer	LOD: 1.54×10^{-12} g mL^{-1}. Dynamic range: 5×10^{-12} - 1×10^{-9} g mL^{-1}	Shu et al. (2019)
Glucose in human urine	2D-MOF nanosheet with peroxidase activity functionalized with luminol and glucose oxidase	Not reported	LOD: 10.667 µg L^{-1}. Dynamic range: 32–5500 µg L^{-1}	Zhu et al. (2019a)

	(GOD), to yield a Co-TCPP(Fe)@luminol@GOD composite material able to generate a CL signal upon simple addition of the sample.			
Parvovirus B19 DNA	Solid-phase DNA hybridization reaction performed in a transparent microfluidic device, followed by antibody-HRP-based CL detection.	Lensless contact imaging on an ultrasensitive cooled charge-coupled device (CCD) camera.	LOD: 0.05 µmol L^{-1}, corresponding to 50 fmol of DNA amplification product.	Roda et al. (2011)
Cortisol in saliva	Lateral flow immunoassay (LFIA) with CL detection, performed in a 3D-printed cartridge containing a sealed fluidic element.	Lensless contact imaging on an ultrasensitive cooled charge-coupled device (CCD) camera.	LOD: 0.2 ng mL^{-1}	Zangheri et al. (2019)
Valproic acid in blood and saliva.	One-step competitive vertical flow immunoassay (VFIA), employing silica nanoparticles doped with a thermochemiluminescent (TCL) 1,2-dioxetane derivative as a label.	By 3D printing, simple accessories were produced to turn a smartphone into a biosensing device that provides a power source for the heat shock required to trigger the TCL reaction and a sensitive camera for measuring emitted photons.	Blood: LOD 4 µg mL^{-1}; Dynamic range 4–300 µg mL^{-1}. Saliva: LOD 0.05 µg mL^{-1}; Dynamic range 0.05–20 µg mL^{-1}	Roda et al. (2019)
Ochratoxin A (OTA), aflatoxin B1 (AFB1) and deoxynivalenol (DON) in food and feedstock.	Microfluidic multiplexing methodology based on the concept of micromosaic immunoassays for mycotoxins immunodetection.	Microfabricated a-Si:H photoconductors	LOD: 0.1, 0.3 and 1 ng mL^{-1} for AFB1, DON and OTA, respectively.	Soares et al. (2017)
Carcinoembryonic antigen.	ELISA kit based on CL immunoassay	Miniaturised photosensor obtained by *in situ* synthesis of	LOD: 3.2 ng mL^{-1}	Im et al. (2017)

		cadmium sulphide nanowires on the gold surface of an interdigitated electrode		
Glucose, lactate, cholesterol, choline.	Multiplex CL enzyme assay performed on a double-layered three-dimensional (3D) microfluidic network, exploited for temporizing reagents delivery	Photomultiplier tube.	LOD: glucose 8 µmol L^{-1}, lactate 15 µmol L^{-1}, choline 6 µmol L^{-1}, and cholesterol 0.07 µmol L^{-1}. Dynamic ranges: glucose 0.01–1.0 mmol L^{-1}, lactate 0.02–5.0 mmol L^{-1}, cholesterol 0.01–0.4 mmol L^{-1}, and choline 0.001–1.0 mmol L^{-1}.	Li et al. (2019)
Human chorionic gonadotropin (hCG).	CL LFIA employing Pt NPs with catalytic activity as enzyme-mimic label.	Ultrasensitive CCD-based imaging.	LOD: 1 mIU mL^{-1}	Park et al. (2015)
IgG	TCL semiconducting polymer dots (TCL-Pdots) as luminescent nanolabels for immunobiosensors.	TCL signal was acquired through a portable CCD camera.	LOD: 13 nmol L^{-1} Dynamic range: up to 230 nmol L^{-1}	Andronico et al. (2018)
Electrochemical biosensors				
Glucose.	Electrochemical biosensing platform using electrochemically reduced graphene oxide (ER-GNO) and ionic liquid doped screen-printed electrode (ER-GNO/IL-SPE) modified with glucose oxidase electrode.	CHI 440 electrochemical workstation.	LOD: 1.0 µM Linear range: 5–12 mM.	Ping et al. (2011)
Phosphorylated p53 (S392).	Electrochemical immunosensor for ultrasensitive detection of	CHI 440 electrochemical workstation.	LOD: 0.01 nM Linear range: 0.02–2 nM	Du et al. (2011)

	phosphorylated p53 at Ser392 (phospho-p53^{392}) based on graphene oxide (GO) as a nanocarrier in a multienzyme amplification strategy.			
Single nucleotide polymorphism.	Graphene oxide nanoplatelets (GONPs) as electroactive labels for DNA analysis.	Autolab PGSTAT302 potentiostat.	The e limit of detection was 500 pM. The differentiation between the wild-type and mutant was detectable at 10 nM.	Bonanni et al. (2012)
Catechol.	Sol–gel based composite of polivinilpirrolidone (PVP) stabilised gold nanoparticles as matrix for tyrosinase in an amperometric biosensor	CHI-Instruments Model 660	LOD: 0.3 µM. Linear range: 1.0–6 µM	Singh et al. (2013)
Hg (2+).	Label-free electrochemical sensor based on the catalytic formation of Au nanoparticle accelerated by Hg^{2+} and detected by stripping voltammetry.	CHI760D electrochemical analytical system.	LOD: 0.06 nM. Linear range: 0.5–120 nM.	Tang et al. (2014)
S. aureus.	Aptamer-conjugated silver nanoparticles for electrochemical dual-aptamer-based sandwich bioassay.	µAutolab type III	LOD: 1 CFU mL^{-1}. Dynamic range: 10–10^6 CFU mL^{-1}.	Abbaspour et al. (2015)
Telomerase activity in cell.	Platinum nanoparticles encapsulated in metal–organic frameworks (MOFs) used for telomerase activity evaluation following the Pt NP electrocatalysis	CHI 660D electrochemical workstation.	LOD: 1×10^2 cells mL^{-1}. Dynamic range: 5×10^2–1×10^7 cells mL^{-1}. Activity calculated in a single cell: 2×10^{-11} IU.	Ling et al. (2016)

(ssDNA) and (dsDNA).	Miniaturised Paper-based electrochemical sensor modified with gold nanoparticles utilizing triplex forming oligonucleotides (TFO) tagged with methylene blue (MB) as the recognizing probes.	Portable potentiostat PalmSens equipped with a multiplexer for 8 cells and connected to a laptop	LOD: 3 and 7 nM, for (ssDNA) and (dsDNA) sequences, respectively.	Cinti et al. (2018)
B. cereus spore.	Gold screen-printed electrode modified with DNA-based aptamer for an impedimetric label-free sensor.	Portable potentiostat PalmSens$_{3}$.	LOD: 3×10^{3} CFU mL^{-1} . Linear range: 10^{4} - 5×10^{6} CFU mL^{-1}	Mazzaracchio et al. (2019)
Organophosphorus pesticide.	A graphite screen-printed electrode modified with carbon black-cobalt phthalocyanine nanocomposite and immobilized Butyrylcholinesterase enzyme	Portable potentiostat PalmSens.	LOD: 18 nm. Linear range up to 110 nM.	Cinti et al. (2016a)
Nerve agent.	Microfluidics biosensor chip with integrated screen-printed electrodes modified with acetylcholinesterase	DY2000 Series Multi-Channel Potentiostat	Not reported	Yoon et al. (2014)
Nerve agent.	Screen-printed electrodes modified with butyrylcholinesterase integrated in microfluidic chip.	Portable potentiostat PalmSens	LOD: 20 ppb. Linear range up to 60 ppb	Arduini et al. (2012a)
Glucose, lactate, and uric acid.	Coupling of electrochemical detection and paper microfluidics to provide rapid quantitative measurement of critical health markers in serum	CHI 1207A potentiostat	Glucose: LOD 0.21 mM, linear range 0–100 mM Lactate: LOD 0.36 mM, linear range 0–50 mM Uric acid: LOD 1.38 mM, linear range 0–35 mM	Dungchai et al. (2009)

Nerve agent.	Fully integrated ready-to-use paper-based electrochemical biosensor	Portable potentiostat PalmSens	LOD: 3 µgL^{-1}. Linear range up to 25 µgL^{-1}.	Cinti et al. (2017)
Paraoxon, 2,4-dichlorophenoxyacetic acid, and atrazine	3D paper-based origami reagentless device for electrochemical measurement of 3 pesticides.	Portable potentiostat PalmSens.	Paraoxon: LOD 2 ppb, linear range up to 20 ppb. 2,4-dichlorophenoxy acetic acid: LOD 50 ppb, linear range up to 600 ppb Atrazine: LOD ppb, linear range 10–100 ppb.	Arduini et al. (2019)
Butyrylcholinesterase.	A reagent-free paper-based printed sensor embedded in a 3D printing device.	Portable EmStat Instrument.	LOD: 0.5 IU/mL. Linear range up to 12 IU/mL.	Scordo et al. (2018)

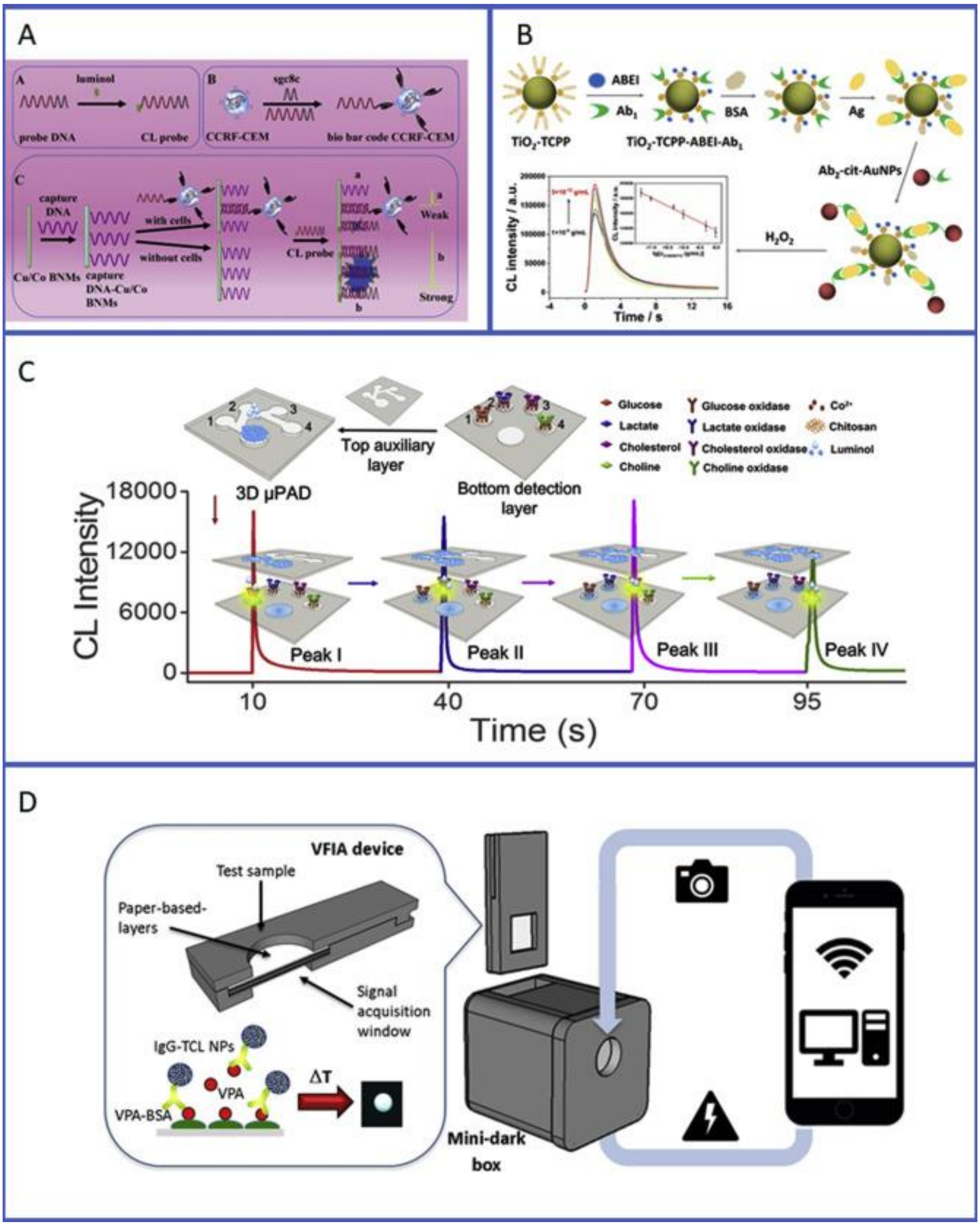

Figure1. Examples of different strategies for improving luminescence quantum yield and innovative CL-based analytical formats. A) Cu/Co bimetallic manomaterials, employed as the nanocatalysts for the CL reaction, enabling detection of cancer cells down to 270 cells mL−1 in an aptamer-based assay (Li et al., 2018); B) Turn-off CRET-based sandwich immunoassay exploiting TiO2 NPs functionalized with a porphyrin derivative and N-(4-aminobutyl)-N-ethylisoluminol (TiO2-TCPP-ABEI nanoluminophores) as CL emitter and AuNPs as energy acceptor (Shu et al., 2019); C) a double-layered three-dimensional (3D) microfluidic network was exploited for temporizing reagents delivery, thus developing a multiplex CL enzyme assay for detecting glucose, lactate, choline, and cholesterol (Li et al., 2019); D) Smartphone-based thermochemiluminescent immunosensor for valproic acid detection (Roda et al., 2019).

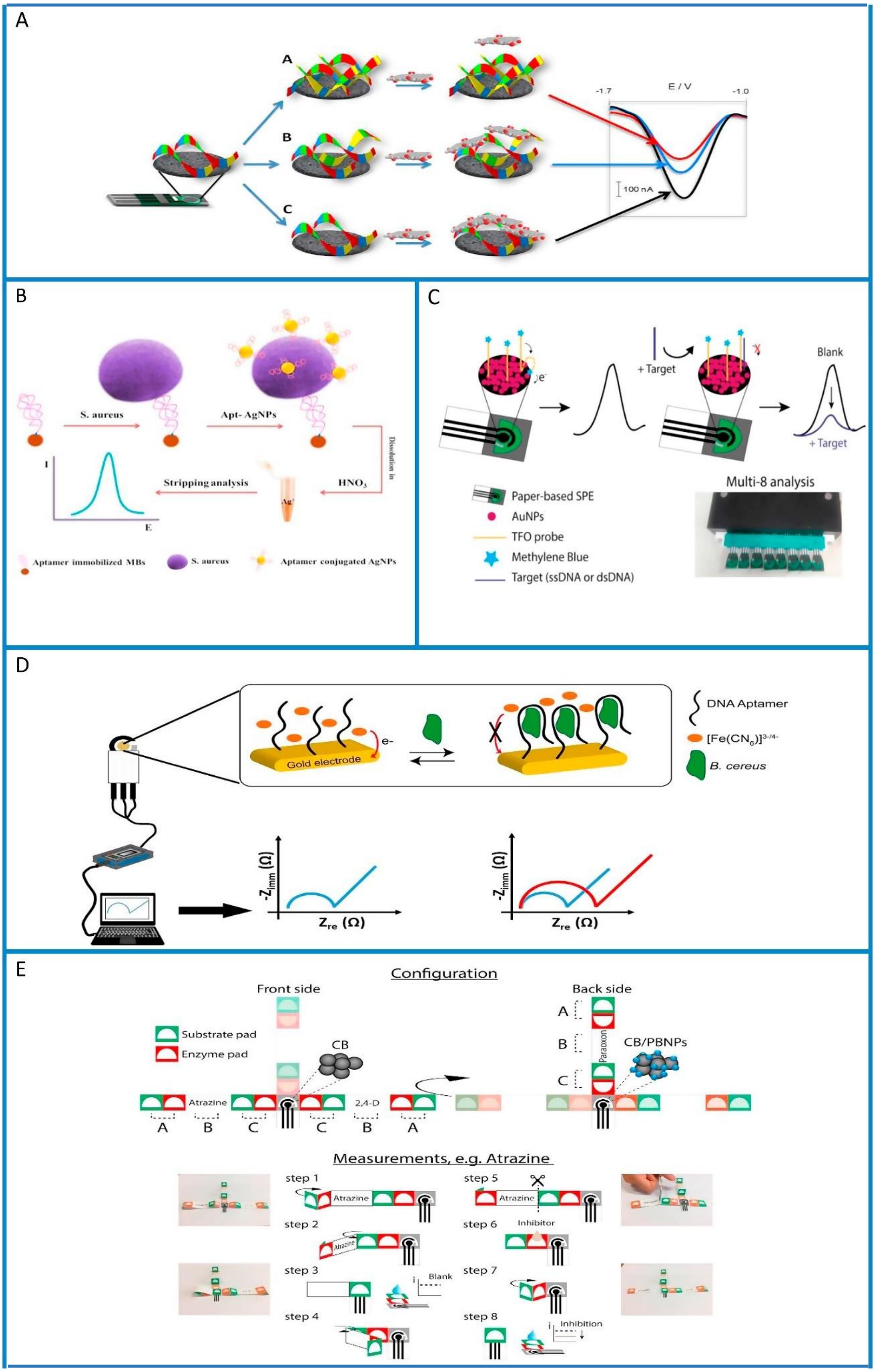
A
A
B
C
E / V
-1.7
-1.0
100 nA
B
S. aureus
Apt- AgNPs
Dissolution in
HNO3
Ag+
Stripping analysis
I
E
Aptamer immobilized MBs
S. aureus
Aptamer conjugated AgNPs
C
e-
+ Target
Blank
+ Target
Paper-based SPE
AuNPs
TFO probe
Methylene Blue
Target (ssDNA or dsDNA)
Multi-8 analysis
D
DNA Aptamer
[Fe(CN6)]3-/4-
B. cereus
Gold electrode
e-
-Zimm (Ω)
Zre (Ω)
-Zimm (Ω)
Zre (Ω)
E
Configuration
Front side
Back side
Substrate pad
Enzyme pad
CB
CB/PBNPs
Paraoxon
Atrazine
2,4-D
A
B
C
C
B
A
A
B
C
Measurements, e.g. Atrazine
step 1
Atrazine
step 2
Atrazine
step 3
i
Blank
step 4
step 5
Atrazine
step 6
Inhibitor
step 7
step 8
i
Inhibition

Figure2. Examples of different cutting-edge technologies used for the development of miniaturised and smart electrochemical biosensors. A) Exploitation of inherently electroactive graphene oxide nanoplatelets for the detection of single-nucleotide polymorphism by following the interactions between graphene oxide nanoplatelets and DNA strands (Bonanni et al., 2012). B) Aptamer and silver nanoparticles combined with magnetic beads for electrochemical determination of S. aureus (Cinti et al., 2018). C) Sensor arrays for the detection of single and double stranded DNA targets using a multi-8 reader (Cinti et al., 2018) D) Portable potentiostat and gold screen-printed electrode modified with selected aptamer for B. anthracis spore simulant (B. cereus) detection (Mazzaracchio et al., 2019). E) An origami paper-based device for a fast and cost-effective multianalysis of several classes of pesticides (Arduini et al., 2019). (For interpretation of the references to color in this figure legend, the reader is referred to the Web version of this article.)

5.3.1. Technological Advancements In Chemiluminescent Biosensors

The main challenge in CL is to improve the relatively low luminescence quantum yield by developing new CL reagent cocktails and catalysts, emitting in different parts of the visible spectrum. Nanomaterials are being extensively employed to improve CL-based bioassays, acting as catalyst, emitter, or energy acceptor (Li et al., 2014; Tiwari and Dhoble, 2018). Starting with the pioneering work showing the ability of metal NPs to catalyze CL reactions (Zhang et al., 2005), nanoluminophores with excellent emission properties were developed by grafting CL reagents on the surface of AuNPs (Zhang et al., 2013), with further improved CL efficiency obtained upon additional functionalization with metal complexes (Huang et al., 2018b). With this approach, immunoassays for human IgG and other proteins have been developed, reaching LODs down to subfemtomolar levels. In addition to metal NPs, other nanomaterials, such as QDs and carbon-based nanomaterials, have been exploited as catalysts or emitters for improved CL biosensing strategies, although their mechanism of action is still under investigations in many cases (Wang et al., 2019). Composite nanomaterials have recently attracted much attention, owing to their superior CL properties over their monomaterial counterparts. For example, Cu/Co bimetallic manomaterials, which provided enhanced catalytical ability thanks to the two metals synergistic effect, were employed as nanocatalysts for the CL reaction, enabling detection of cancer cells down to 270 cells mL−1 in an aptamer-based assay (Li et al., 2018). Graphene oxide-based composite materials (e.g., metal-GO or bimetallic-GO) have also been prepared to improve the GO catalytic activity towards CL reactions. With this approach, a dramatic enhancement of the luminol−H2O2 and lucigenin−H2O2 CL reactions was obtained by coupling Co2+ and GO. Theoretical studies revealed that the coupling between metal ions and GO induced effective polarization charges, facilitating the generation of several radicals that drive the CL reaction. However, applicability in biosensors has not been demonstrated yet (Wang et al., 2017). Nanotechnology can bring a significant progress in CRET, which has been poorly exploited due to the small energy transfer efficiency and to the limited number of effective CL donors and energy acceptors. For example, a turn-off CRET-based sandwich immunoassay was developed for copeptin, a surrogate marker for acute myocardial infarction, exploiting TiO2 NPs functionalized with a porphyrin derivative and N-(4-aminobutyl)-N-ethylisoluminol (TiO2-TCPP-ABEI nanoluminophores) as CL emitter, while AuNPs were employed as energy acceptor. The assay provided a wide dynamic range (5 × 10−12 - 1 × 10−9 g mL−1) with a LOD of 1.54 × 10−12 g mL−1, which was superior to previously reported CL-based immunoassays. (Shu et al., 2019). Other novel materials, such as metal-organic frameworks (MOFs) and layered double hydroxides (LDHs) have very recently appeared on the scene of CL biosensing, opening a new perspective for further improved analytical performance. As an example, Zhu et al., developed a CL-based biosensor for one-step and rapid detection of glucose in human urine down to 50 nM, exploiting a 2D-MOF nanosheet with peroxidase activity functionalized with luminol and glucose oxidase (GOD), to yield a Co-TCPP(Fe)@luminol@GOD composite material able to generate a CL signal by simple addition of the sample (Zhu et al., 2019a). In parallel with advances in nanomaterial science that boosted CL-based biosensors sensitivity, great advancements towards their point-of-need applicability have been achieved thanks to technological innovation, providing miniaturised ultrasensitive photon detectors and novel portable analytical formats (Roda et al., 2011; Mirasoli et al., 2014a). Indeed, CL is particularly suited for miniaturization, as it does not require wavelength selection of the acquired signal, nor specific geometries for the measurement cell (Roda et al., 2016). The only main requirement is maximizing photon collection efficiency, which is easily obtained in "contact" geometries, in which the measurement cell is in direct contact with the photodetector (Roda et al., 2011). The fast innovation in electronics has enhanced the development of miniaturised transducers for point-of-need CL biosensors, such as cooled slow-scan or intensified CCD sensors (Zangheri et al., 2019), a smartphone CMOS sensor (Rezazadeh et al., 2019; Roda et al., 2019) and thin film photosensor arrays (Soares et al., 2017; Mirasoli et al., 2014b). Also in this field, nanotechnology could open the door for novel opportunities. Recently, a miniaturised photosensor was obtained by in situ synthesis of cadmium sulphide nanowires on the gold surface of an interdigitated electrode. The photosensor provided a LOD of 3.2 ng mL−1 in a CL immunoassay for carcinoembryonic antigen, which is similar to that obtained with a commercial photomultipler tube-based luminometer (Im et al., 2017). Apart from the photodetector miniaturization, the biosensor analytical format plays a crucial role for its point-of-need applicability. The main critical point of CL biosensors is the requirement for a complex set of ancillary equipment for handling reagents and washing steps in the microfluidic network. The cheapest and most affordable approach is based on cellulose-based supports, such as micro paper-based analytical devices (µPAD) and lateral-flow immunoassay (LFIA), which has deservedly become a current trend in the field of real-time analysis (Zhu et al., 2019b). Several CL paper-based biosensors have been developed, exploiting various solutions to provide multiplex analysis. For example, a double-layered three-dimensional (3D) microfluidic network was exploited for temporizing reagents delivery, thus Developing A Multiplex CL Enzyme Assay For Detecting Glucose, Lactate, choline, and cholesterol with LODs of 8 µmol L−1, 15 µmol L−1, 6 µmol L−1, and 0.07 µmol L−1, respectively (Li et al., 2019). Furthermore, to overcome the shortcomings of natural enzymes as labels, Pt NPs with catalytic activity were employed as enzyme-mimic labels in a CL LFIA, providing a far higher thermal stability than HRP at room temperature, and displaying a LOD of 1 mIU mL−1 for human chorionic gonadotropin (hCG) (Park et al., 2015). As an alternative, thermochemiluminescent (TCL) silica- and polymer-based NPs are promising labels for miniaturised biosensor formats, as they combine high detectability of CL with reagentless trigger of the light emission, which is simply elicited by heat (Andronico et al., 2018; Roda et al., 2019).

5.3.2. Technological Advancements In Electrochemical Biosensors

The advanced technologies such as nanomaterial, printing and microfluidic technologies boosted the electroanalysis towards a true Renaissance, conferring new features to the electrochemical (bio)sensors (Escarpa et al., 2012) including low detection limit, high sensitivity, miniaturization, and low sample volume. In the field of electrochemical biosensor, the use of graphene has allowed to design smart electrochemical biosensors thanks to the polyedric features of this nanomaterial, such as the tailorability of the electrochemical properties of the developed biosensor. Indeed, the metallic impurities present in graphene as well its structure, i.e. single or multi layers, are able to affects the electroanalytical response (Ambrosi et al., 2012a, 2012b; Kampouris and Banks, 2010; Goh and Pumera, 2010). In addition, the amount of oxygen and the number of defect sites have a high effect on the electrochemical behaviour, improving e.g. electron transfer and allowing for low detection limit of the target analyte (Ambrosi et al., 2014). Furthermore, the 2D structure of graphene has been exploited to use graphene as label or as loading agent for biomolecules and inorganic nanomaterials thanks to its high surface area and easy functionalization. One of the first enzymatic graphene-based biosensors has been reported by Ping et al., which developed a glucose biosensor by the electrodeposition of reduced graphene-oxide and immobilisation of glucose oxidase via cross-linking method (Ping et al., 2011). The presence of graphene demonstrated the detection of enzymatic by-product hydrogen peroxide at low negative applied potential (−0.2 V vs Ag/AgCl), allowing for glucose quantification with a wide linear range up to 12 mM and detection limit equal to 1.0 µM. In the immunosensor field, graphene was exploited for its double function: i) improvement of the electrochemical performances and ii) loading of antibodies/enzymes for the enhancement of a signal output. For instance, graphene oxide was used as substrate to immobilise the enzyme horseradish peroxidase and the antibody p53392Ab2 for the detection of the tumour suppressor and transcriptor factor p53 (392) with a range up 2 nM and low detection limit equal to 0.01 nM, which is 10-fold lower in respect to the detection limits of established sensors using peroxidase-streptavidin-biotin-p53392Ab2 (Du et al., 2011). The characteristic of graphene oxide nanoplatelets, namely inherently electroactive, was exploited to design an interesting DNA sensor for the detection of single-nucleotide polymorphism by following the interactions between graphene oxide nanoplatelets and DNA strands. The strategy of the detection relays on the different binding ability of single-stranded and double-stranded DNA towards graphene oxide nanoplatelets and the stronger ability of graphene to conjugate ssDNA with respect to dsDNA. As results, the non-complementary target yielded a higher voltammetric signal than the complementary target (Bonanni et al., 2012), with a detectable difference between the wild-type and mutant at 10 nM. Beyond graphene, gold nanoparticles are the most employed nanoparticles also in the realization of electrochemical biosensors, followed by Silver- and Platinum-NPs. As an example, gold nanoparticle-based sol-gel stabilised with polyvinylpyrrolidone was utilised as matrix for tyrosinase enzyme immobilisation for the detection of catechol under µM level with improved storage stability up to 6 weeks (Singh et al., 2013). Metallic nanoparticles were also used as label to evaluate the reaction between the biocomponent and the target analyte. For instance, the specific interaction between thymine and Hg2+ was exploited for the Hg2+ detection, forming the complex thymine-Hg2+-thymine together with gold nanoparticles synthesized in loco as signal reporter, and using stripping voltammetry as detection technique (Tang et al., 2014). Silver nanoparticles have been adopted in an aptamer assay for S. aureus, by using a biotinylated primary anti-S. aureus aptamer onto streptavidin-coated magnetic beads as the capture agent, and a second anti-S. aureus aptamer conjugated to AgNPs as the detection agent. The binding between the aptamer and bacteria was quantified by anodic stripping voltammetry of Ag ions, reaching a detection limit of 1 CFU mL−1 (Abbaspour et al., 2015). Platinum nanoparticles encapsulated in metal–organic frameworks have used for telomerase activity evaluation following their electrocatalysis, observing a linear range from 500 to 107 cells mL−1, with the activity calculated in a single cell equal to 2 × 1011 IU (Ling et al., 2016). Gold nanoparticles have been also exploited as anchor points for the attachment of the thiol-extremity of DNA probes, as well as to improve the electrochemical performances as in the case of ss- and ds-DNA sequence detection of HIV in serum samples. The configuration of a miniaturised sensor combined with DNA probe and gold nanoparticles allowed detection limits of 3 and 7 nM, for ss and ds sequences, respectively (Cinti et al., 2018). One of the main features of electrochemical biosensor relies on the delivery of highly cost-effective devices thanks to the use of printing technology for their production. In the continuously growing of 2D printing technology field, screen-printing, ink-jet, roll-to-roll, sheet-to-sheet are the main types selected for device production. If the ink-jet printing is the most used in printed electronics, screen-printing remains the preferred one in manufacturing process of electrochemical sensor, being able to fabricate a huge number of sensors in few hours. Screen-printed electrodes have been widely used in the environmental, biomedical, and agrifood sectors for the detection of several analytes including pesticides, chemical and biological warfare agents, toxins, glucose, lactate, in a plethora of samples. For instance, gold screen-printed electrode has been modified with DNA-based aptamer for a single-step detection of B. anthracis spore simulant (B. cereus spore) using an impedimetric label-free approach. Under the optimized conditions, B. cereus spores were detected with a linear range between 104 CFU/ml and 5 × 106 CFU/ml and a detection limit of 3 × 103 CFU/mL, providing an aptasensor combined with a portable instrument for an on-site label-free measurement of B. anthracis spore simulant (Mazzaracchio et al., 2019). In the case of gold printed electrodes, the self-assembled monolayer technique is used to immobilise the biocomponent thanks to the thiol-gold bonding; in the case of graphite-based screen-printed electrode, cross-linking based-immobilisation is often chosen. As an example, a graphite screen-printed electrode was modified by drop casting with a nanocomposite constituted of cobalt phthalocyanine and carbon black followed by the immobilisation of butyrylcholinesterase enzyme using glutaraldehyde, Nafion, albumin bovine serum, allowing for organophosphorus pesticide detection at ppb level (Cinti et al., 2016a). The possibility of using miniaturised sensor with low volume sample has also furthered the development of lab on a chip combining microfluidic with electrochemical miniaturised biosensors. Screen-printed electrodes modified with acetylcholinesterase (Yoon et al., 2014) or butyrylcholinesterase (Arduini et al., 2012a) were integrated in microfluidic chip to identify the presence of nerve agents in liquid solution or in vapour phase. However, the designed microfluidic devices required the addition of solution containing the reagents, external pump or the intervention of the operator. In the era of sustainability, the electrochemical printed biosensors have rediscovered an old material, i.e. paper, which has opened a new research line delivering electrochemical paper-based analytical devices (ePADs). These sustainable analytical tools are able to treat the sample, store the reagent, make the measurement, being the electrochemical cell printed directly on paper, without any external pump. ePADs have initially attracted a huge attention in biomedical field, being able to match the ASSURED criteria has been reported by Henry group, which designed microfluidic channels on filter paper by using photolithography, and electrochemical cells on filter paper by using the screen-printing technology. For selective quantification of glucose, lactate and uric acid, glucose oxidase, lactate oxidase, and uricase enzymes were entrapped in three different zones of filter paper to detect these analytes, by easily adding the biological liquid sample in the centre zone of the device (Dungchai et al., 2009). In this case, an external pump is not required because the solution flow is driven by the capillarity properties of the paper, and the reagents are not added by the operator, but previously entrapped in the cellulosic network of the paper. For ePADs, both lateral and vertical flow microfluidic have been exploited, thanks to the capability of the electrochemical sensors to work in different configurations. Furthermore, the wax-printing to create the paper-based microfluidic, combined with the screen-printing technique to print the electrochemical cell, are capable to deliver a paper-based analytical tool characterised by low cost and easiness to use, where only the addition of the few μL of the sample is the task required to the operator. As an example of lateral flow, an integrated paper-based screen-printed electrochemical biosensor device able to quantify nerve agents was reported. In detail, a paper-device with dual electrochemical measurements of butyrylcholinesterase activity was designed to evaluate the response in presence and in absence of polluted water samples. By just adding few μL of the sample on a dedicate zone that wets both the strips, it is possible to detect a nerve agent simulant down to 3 μg L−1, delivering a fast and easy to use analytical tool (Cinti et al., 2017). The foldability of the paper combined with the flexibility of the electrochemical measurement has allowed the design of an attractive origami paper-based device. To this regard, a three-dimensional origami paper-based device for the detection of several classes of pesticides by combining different enzyme-inhibition biosensors was developed. By combining different office paper-based screen-printed electrodes with multiple filter paper-based pads, and folding, cutting and unfolding them, it is possible to measure different classes of pesticides at ppb level just directly adding the sample without any previous sample treatment and exploiting the vertical microfluidic of the eco-designed device (Arduini et al., 2019). Furthermore, the combination of different technologies such as screen, wax and 3D-printing, allowed the delivery of smart point of care devices for biomedical application. For instance, Scordo et al. reported the first example of a rapid and easy to use paper-based printed sensor embedded in a 3D printing device for the measurement of butyrylcholinesterase activity in serum samples. This analytical tool encompasses paper-based microfluidic using wax printing, screen-printing to print the electrodes, and stereolithography using 3D printing technology for a customised fabrication of the holder. Butyrylcholinesterase activity was measured in serum with a linear range up to 12 IU/mL and a detection limit of 0.5 IU/mL, demonstrating its suitability as a point of care, being normal value range of comprised between 5.9 and 13.2 IU/mL (Scordo et al., 2018).

5.4. ELECTRON-BASED VS PHOTON-BASED BIOSENSORS: AN EXPERIMENTAL CHALLENGE

In the previous scenario we have highlighted the major trends in CL and electrochemical biosensor field, demonstrating how the cutting-edge technologies impact the dimension, the cost, the sample volume and treatment, and the analytical performances of these devices. However, the reported literature demonstrated the relevant features of both CL and electrochemical biosensors, without revealing the best transducer for highly sensitive, cost-effective and on-site measures. To face this challenge, a direct comparison in the same working condition is needed. Herein, we report the experimental results related to H2O2, HRP, IgG, and glucose measurements by using some of the above technologies, and sharing the same reagents to give a correct competition between photons and electrons. Protocol schemes are depicted in Fig. 3.

Once added the reagents in the microwell, CL acquisition were immediately performed (1s Varioskan Flash reader, 120s CCD camera)

Incubation time of 10 min, followed by amperometric measurement (60 s)

Once added the reagents in the microwell, CL acquisition were immediately performed (1s)

Amperometric measurement (60 s)

CL measurements (120s)

Amperometric measurement (300 s)

CL measurements (120s)

Amperometric measurement (60 s)

Figure.3. Layout of experimental protocols employed for biosensing measurements in this work.

5.4.1. Materials and methods

5.4.1.1. Reagents

Peroxidase from horseradish Type VI-A (1080 U mg−1) was purchased from Sigma-Aldrich. For HRP electrochemical measurement, a supersensitive solution ready to use containing TMB + hydrogen peroxide in buffer was used (Sigma Aldrich). For HRP CL measurement, black (with clear bottom for contact imaging) 96-multiwell plate (Thermo Fisher Scientific) and the CL substrate Super Signal ELISA Femto (Thermo Fisher Scientific) were employed. Magnetic beads (MBs) coated with Goat Anti-Rabbit IgG were supplied as a suspension containing 3.65 × 1010 beads mL−1 by New England Biolabs (Ipswich, MA, UK). Hydrogen peroxide standard solution was purchased from WWR Prolabo Chemicals.

5.4.1.2. Instrumentation And Sensors For CL Measurements

For CL measurements in a benchtop configuration, a PMT based microtiter reader (Varioskan Flash multimode reader, Thermo Fisher Scientific, Waltham, MA, USA) was employed, which displays a sensitivity of <7 amol ATP/well and a dynamic range >7 decades, as measured by flash ATP reaction in a 384-well plate. As a portable device, a thermoelectrically cooled portable ATIK 11000 CCD camera (ATIK Cameras, New Road, Norwich) connected to a light-tight dark box was employed. The CCD camera, which is equipped with a large format, high resolution monochrome CCD sensor (Kodak KAI 11002, sensor size 37.25 × 25.70 mm) cooled by a two-stage Peltier element to reduce thermal noise, was either coupled with an objective (Computar 2/3 in. 8 mm, f1.4, obtained from CBC AMERICA Corp., Commack, NY), or employed in contact imaging approach, employing a polymethylmethacrylate fiber optic faceplate (size 26 × 26 × 13 mm, Edmund Optics, Barrington, NJ), as previously reported (Zangheri et al., 2019).

In all measurements, data were subtracted of the blank signal.

The contact lensless imaging CCD-based device has been designed to maximize the photon collection efficiency, as previously reported (Roda et al., 2011). A theoretical evaluation of the detectability of a model analyte, such as luminol, can be performed. Considering that in a back-illuminated cooled CCD camera each pixel is characterized by an electronic readout noise of about 10 electrons, that thermal noise is negligible when the sensor is cooled down to −20 °C, and that the quantum efficiency (i.e., the ratio of generated electrons over impinging photons) is at least 50%, about 60 photons are necessary for obtaining a signal-to-noise ratio of 3. Assuming a 180° light collection angle typical for a contact imaging configuration, the number of photons doubles to 120. As the luminol/H2O2 CL system displays a ΦCL of about 1% in aqueous solutions, about 1,2 × 104 luminol molecules should undergo oxidation to produce this photons output. Therefore, if we consider a 1-mm2 sensing area (corresponding to 12000 pixel for a pixel size of 9 × 9 μm), 200 amol of CL products can be detected in 1s.

5.4.1.3. *Instrumentation And Sensors For Electrochemical Measurements*

For electrochemical measurements, a laboratory potentiostat Autolab electrochemical system equipped with PGSTAT-12 and GPES software (Eco Chemie, Utrecht, The Netherlands) or a portable potentiostat equipped with PS Trace 3.0 software (Palm Sens, The Netherlands) were employed. Polyester-based screen-printed electrodes (SPEs) were produced with a 245 DEK (Weymouth, UK) screen-printing machine. Graphite-based ink (Electrodag 423 SS) from Acheson (Milan, Italy) was used to print both the working and auxiliary electrode. Silver/silver chloride ink (Electrodag 477 SS) was used to print the pseudo-reference electrode. The substrate has been a flexible polyester film (Autostat HT5) purchased from Autotype Italia (Milan, Italy). The diameter of the working electrode was 0.3 cm resulting in a geometric area of 0.07 cm2. SPEs were then modified by drop casting with 6 µl of Carbon Black (CB) dispersion 1 mg/mL (Arduini et al., 2012b) (for HRP and IgG measurement) or with dispersion 1 mg/ml of Carbon Black + Prussian Blue nanoparticles (CB/PBNPs) for H2O2 measurement (Cinti et al., 2014). For the CB/PBNPs powder production, we followed our previous procedure (Moscone et al., 2001), where graphite was substituted by CB. CB/PBNPs powder was finally used to produce dispersion at a concentration of 1 mg in 1 mL of a dimethylformamide:water (1:1) mixture used as solvent, and then sonicated for 60 min at 59 kHz. The dispersion was used for modifying bare SPEs via drop-casting. In detail, a small volume (6 µL) of the CB/PBNPs dispersion was cast onto the working electrode surface in three steps of 2 µL each (CB/PBNPs-SPE).

5.4.1.4. Horseradish Peroxidase Measurement

Peroxidase was serially diluted in the range 2 × 10−15 to 6 × 10−12 mol L−1 in 0.1 M phosphate buffered saline (PBS) pH 8 and analysed by CL or electrochemical detection. For CL detection, 20 µL of HRP solution was dispensed in the wells of the multiwell plate, then 80 µL of Super Signal ELISA Femto was added. Photon emission was measured with the Varioskan Flash reader or the CCD camera with a signal integration time of 1 s or 120 s, respectively. For HRP electrochemical measurement, 125 µL of supersensitive solution (TMB + hydrogen peroxide in buffer) and 10 µL of HRP enzyme at different concentration were added on the surface of the SPE.

After 10 min 25 µL of NaN3 0.024 M was added to stop the reaction and the current was measured in chronoamperometry using SPE modified with CB and the following conditions: applied potential = −100 mV, duration time = 60 s, interval time = 0.1 s. The current was measured at 60 s.

5.4.1.5. Hydrogen Peroxide Detection

Calibration curves for H2O2 were prepared in the range 1 × 10−8 – 1,25 × 10−3 M in 0.1 M phosphate buffered saline (PBS) pH 8. Hydrogen peroxide was detected by CL employing HRP as a catalyst. In particular, 20 µL of HRP solution (1 × 10−6 g mL−1 in PBS) and 40 µL of the Super Signal ELISA Femto kit (only the Luminol component) was dispensed in the wells of a 96-well plate. Upon addition of 40 µL of the H2O2 solution, photon emission was measured in the Varioskan Flash reader or the CCD camera with a signal integration time of 1 s or 120 s, respectively. Hydrogen peroxide was electrochemically detected by direct reduction. Briefly, 70 µL of hydrogen peroxide standard solution was added on the surface of a SPE modified with CB/PBNPs. The current was chronoamperometrically measured using the following conditions: applied potential = −100 mV, duration time = 60 s, interval time = 0.1 s. The current was measured at 60 s.

5.4.1.6. Paper-Based Enzyme Biosensor For Glucose Detection

A Paper-based Analytical Device (PAD) was designed employing Labor (67 g/m2) filter paper, purchased from Cordenons (Italy), as a substrate. ColorQube 8580 office printer from Xerox (USA) was used to print a specific hydrophobic pattern on paper, previously designed using a drawing software (Adobe Illustrator). The wax-printed paper was then placed in an oven for 2 min at 100 °C, allowing the printed wax to penetrate the substrate producing a hydrophobic boundary around hydrophilic areas. Glucose Oxidase enzyme (GOx) was immobilized onto wax-modified filter paper, in which a hydrophobic pattern was exploited to entrap the GOx solution into the desired area. 4 µL of GOx solution (50 U $mL{-1}$ in 0.05 M phosphate buffer pH = 6 containing 0.1 M KCl) were drop-cast onto the PAD hydrophilic area and solvent was let evaporate. Only for electrochemical measurements, GOx-containing PADs were fixed by means of a common glue onto CB/PBNPs-modified office paper sensors, produced as follows: conductive inks were used to print a three-electrode system onto the wax-modified office paper sheets, as previously described (Cinti et al., 2016b, 2019), then the working electrode surface was modified with 6 µL of a CB/PBNPs (1 mg/mL m/v), by drop-casting 2 µL for three times. For assay execution, 40 µL of glucose solution (concentration range 5 × 10−6 – 2,50 × 10−4 M in phosphate buffer) was added and the CL or electrochemical detection was achieved. For CL detection 40 µL of Super Signal ELISA Femto was added and photon emission was measured employing the CCD camera with a 120-s signal integration time. Electrochemical detection was carried out by recording the amperometric signal. Applied potential = 0 mV, duration time = 300 s, interval time = 0.1 s. The current was measured at 300 s.

5.4.1.7. Immunoassay for IgG detection

A model non-competitive sandwich type immunoassay for IgG quantitative detection was set up. Goat Anti-Rabbit IgG magnetic beads were used as a solid phase. For the assay, 10 µL of magnetic beads suspension and 200 µL of solution containing Rabbit IgG at different concentrations were added in different tubes and incubated for 30 min. Upon washing, 200 µL of Goat Antirabbit-HRP diluted 1:400 v/v were added to each tube and incubated for

30 min. After the washing step, magnetic beads were re-suspended in 50 µL of phosphate buffer, and either CL or electrochemical detection was performed. For CL detection, 20 µL of MBs suspension was dispensed in the wells a multiwell plate and, upon addition of 60 µL of Super Signal ELISA Femto, photon emission was measured in the Varioskan Flash reader or the CCD camera with a signal integration time of 1 s or 120 s, respectively. For electrochemical detection, 20 µL of MBs suspension were transferred onto the surface of a CB- modified SPE using the magnetic support for concentrate the beads onto the working electrode. The sandwich-complex was revealed by adding 70 µL of the substrate supersensitive solution TMB + hydrogen peroxide ready-to-use. The product was chronoamperometrically measured using the following conditions: applied potential = −100 mV, duration time = 60 s, interval time = 0.1 s. The current was measured at 60 s.

5.5 RESULTS AND DISCUSSION

A series of experiments were carried out to directly compare the performance of CL and electrochemical detection in different bioassay formats, employing the same reagents and when possible, the same experimental conditions. The optimal conditions for each detection principle were in fact established, in each experiment, based on the expertise of the two research groups, taking advantage of the availability of optimized protocols and of state-of-the-art instrumentation available in their laboratories, in order to challenge each detection principle while operating at its best possibility. With this approach, it was possible to highlight for both methods their strengths and weaknesses in biosensing. In HRP assay, two types of instrumentation were employed: a state-of-the-art laboratory benchtop instrumentation and a portable instrumentation suitable for Point-of-need applications, with the aim of evaluating the performances of the portable and laboratory benchtop instrumentation with the same transduction principle. In all the experiments, the limit of detection (LOD) was calculated as the analyte concentration corresponding to the mean blank signal plus three times its standard deviation; the limit of quantification (LOQ) was similarly calculated employing ten times the blank standard deviation, while the linear range was evaluated by applying the analysis of variance (ANOVA). Table 2 reports the summary of calculated values.

Table 2. Analytical performances of CL and electrochemical sensing tools.

LOD	LOQ	DYNAMIC RANGE	ASSAY TIME	LOD	LOQ	DYNAMIC RANGE	ASSAY TIME
CL H2O2 measurements				**EC H_2O_2 measurements**			
1×10^{-7} mol l^{-1} (4×10^{-12} mol/well)	4×10^{-7} mol L^{-1} (1.6×10^{-11} mol/well)	up to $1{,}25 \times 10^{-3}$ mol L^{-1} (5×10^{-8} mol/well)	No incubation time. Measurement time: 1s (Varioskan Flash Reader); 120s (CCD camera)	3×10^{-6} mol L^{-1} (2.1×10^{-10} mol/well)	7×10^{-6} mol L^{-1} (5.0×10^{-10} mol/well)	up to 5×10^{-4} mol L^{-1} (3.5×10^{-8} mol/well)	No incubation time. Measurement time: 60 s, using bench-top (Autlab) instrument.
CL HRP measurements				**EC HRP measurements**			
2×10^{-15} mol l^{-1} (4.5×10^{-20} mol/well)	9×10^{-15} mol L^{-1} (2.0×10^{-19} mol/well	up to 1×10^{-9} mol L^{-1} (3×10^{-14} mol/well)	No incubation time. Measurement time: 1s (Varioskan Flash Reader); 120s (CCD camera).	2×10^{-15} mol L^{-1} (2.0×10^{-20} mol/well)	$3{,}5 \times 10^{-15}$ mol L^{-1} (3.5×10^{-20} mol/well)	up to 1.9×10^{-11} mol L^{-1} (1.9×10^{-16} mol (well)	10 min as incubation time. Measurement time: 60 s, using both bench-top (Autlab) and portable (Palm

							Sens) instruments.
CL GLUCOSE measurements				**EC GLUCOSE measurements**			
1.7 × 10^{-5} mol l^{-1}	2.3 × 10^{-5} mol L^{-1}	2 × 10^{-3} mol L^{-1}	No incubation time. Measurement time: 120s (CCD camera).	4 × 10^{-5} mol L^{-1}	1.3 × 10^{-4} mol L^{-1}	1 × 10^{-2} mol L^{-1}	No incubation time. Measurement time: 300 s, using portable (Palm Sens) instrument
CL IgG measurements				**EC IgG measurements**			
1.2 × 10^{-14} mol l^{-1}	1.6 × 10^{-13} mol L^{-1}	up to 1.3 × 10^{-12} mol L^{-1}	Incubation time: 30 min. Measurement time: 1s (Varioskan Flash Reader); 120s (CCD camera).	1.2 × 10^{-13} mol L^{-1}	2.7 × 10^{-13} mol L^{-1}	up to 6.7 × 10^{-12} mol L^{-1}	No incubation time. Measurement time: 60 s, using portable (Palm Sens) instrument.

5.5.1. HRP measurement

HRP is one of the most frequently employed enzyme label in biosensors, its detectability being strictly related to the achievement of a low LOD, keeping a reasonable linear range. The calibration curves were constructed for HRP enzyme, to evaluate detectability and linear dynamic range for the enzyme detection. The HRP concentration detection involves of course the measurement of its activity under a fixed incubation time, working in a substrate excess; however, the best choice should be an enzyme with high purity and high specific activity, thus producing an adequate signal in a short time using a small amount of label. For CL-based detection (Fig. 4A), the calibration curve obtained at the Varioskan showed a LOD of 2 × 10−15 mol L−1 (corresponding to 4.5 × 10−20 mol/well), a LOQ of 9 × 10−15 mol L−1, with a linear range extending up to 1 × 10−9 mol L−1. Employing portable instrumentation, a very slight increase of the LOD value was observed (7 × 10−15 mol L−1 for contact imaging, 1 × 10−14 mol L−1 for optics-based imaging, corresponding to 13 × 10−20 mol/well and 23 × 10−20 mol/well, respectively), thus confirming high HRP detectability also in POCT configuration. Interestingly, the CCD-based imaging approach provided the highest signal-to-noise values at each HRP concentration, thus providing higher assay sensitivity, owing to the higher calibration curve slope.

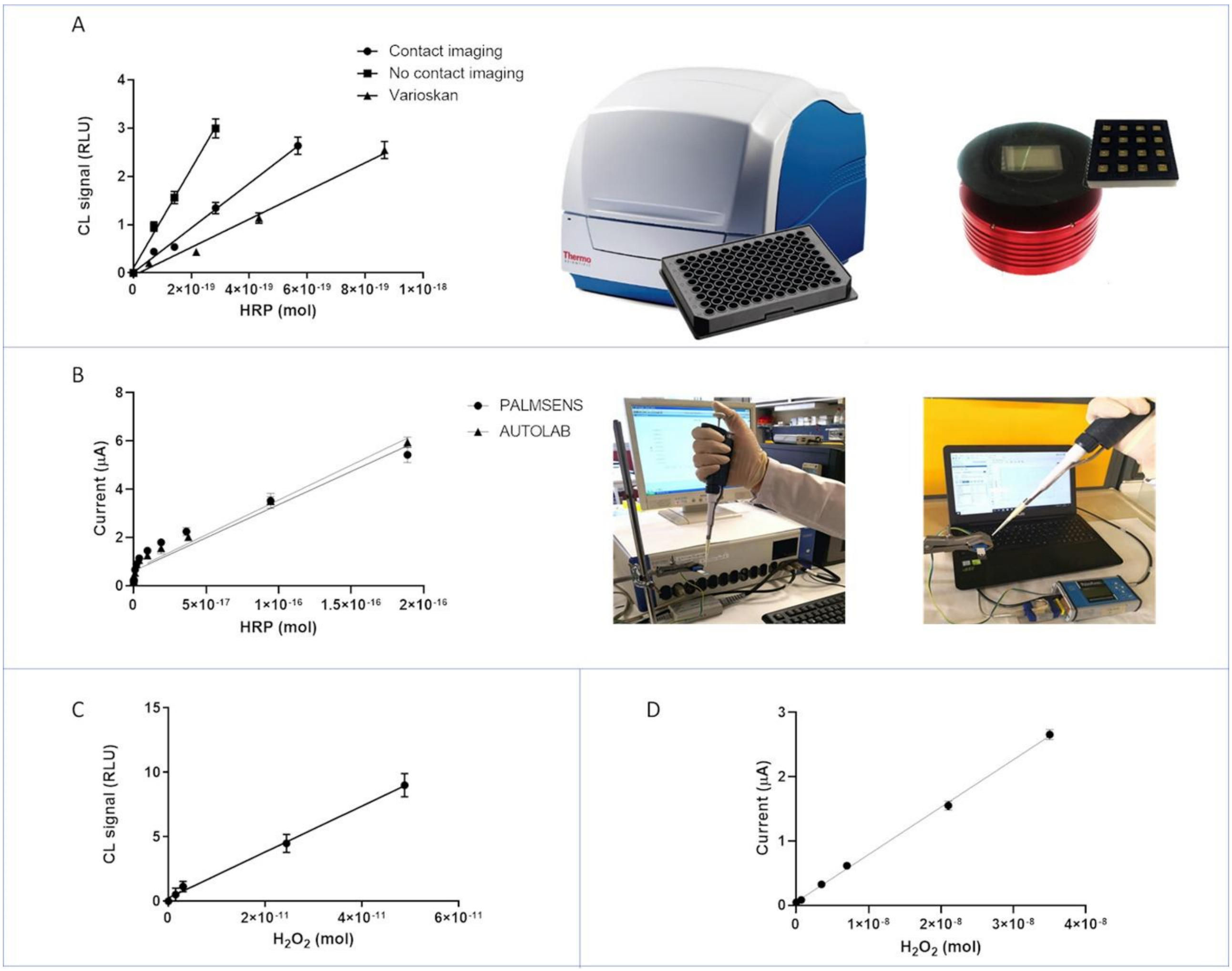

Figure4. A) Calibration curve of HRP by CL-based detection, employing the Varioskan bench-top instrumentation (triangles) or the cooled CCD-based portable device employed in the contact (circle) or optics-based (squares) configuration. B) Calibration curve of HRP using electrochemical sensor based on SPE

modified with CB and portable instrument (blue line) or laboratory benchtop instrumentation (black line). C) CL calibration curve of H2O2 using laboratory benchtop Varioskan instrumentation. D) Calibration curve of H2O2 using laboratory benchtop instrumentation and SPE modified with CB/PBNPs. (For interpretation of the references to color in this figure legend, the reader is referred to the Web version of this article.)

One peculiar feature for CL detection is the possibility to extend the dynamic range of the assay by changing the signal integration time, particularly when imaging is performed. Indeed, by using high integration times for low HRP concentrations and gradually decreasing the integration times at higher HRP concentration, pixel saturation effects can be avoided, thus maintaining low LOD values, while further extending the dynamic range of the assay. The electrochemical calibration curve obtained, reported in Fig. 4B, showed a LOD of 2 × 10−15 mol L−1 (corresponding to 20 zmol) and a LOQ of 3,5 × 10−15 mol L−1, with a first linear range extending from 0.34 up to 3.5 × 10−14 mol L−1 and a second linear range extending from 0.45 up to 19 × 10−12 mol L−1. Employing the portable instrumentation, a slight increase of the LOD (3 × 10−15 mol L−1) and LOQ (9 × 10−15 mol L−1) values was observed (corresponding to 3.0 × 10−20 and 9.0 × 10−20 mol/well, respectively). The laboratory instrument provided the higher sensitivity at the lower concentration range. This behaviour is ascribed to the presence of additional electronic components in laboratory benchtop instrumentation able to filter the noise at nA signal output, giving higher signal/noise ratio. To evaluate the ability of CL or electrochemical measurements to distinguish between slightly different analyte concentrations, i.e. their sensitivity, the slope of the calibration curve was divided by the average standard deviation measured in the points of the curve. For CL detection performed with the Varioskan instrumentation a value of 3000 mol−1 was obtained, while electrochemical measurements performed with the Autolab provided a value of 21000 mol−1 in the first part of the curve and 30 mol−1 in the second linear range. Therefore, electrochemical measurements provided higher discrimination ability at lower analyte concentration, while CL was superior in the higher concentration range.

5.5.2. Hydrogen Peroxide Detection

Hydrogen peroxide is involved in many coupled enzymatic reactions, being the enzymatic by-product of the oxidase enzymes; therefore many analytes have been detected via its measurement with different approaches. The results obtained using CL sensor (Fig. 4C), show a LOD of 1 × 10−7 mol L−1 and a LOQ of 4 × 10−7 mol L−1 (corresponding to 4 × 10−12 mol/well and 16 × 10−12 mol/well, respectively), with a linearity extending up to 1,25 × 10−3 mol L−1. Results obtained using laboratory benchtop instrumentation and SPE modified with CB/PBNPs (Fig. 4D) demonstrated a lower detectability (i.e., LOD equal to 3 × 10−6 mol L−1 and LOQ equal to 7 × 10−6 mol L−1, corresponding to 210 × 10−12 mol/well and 500 × 10−12 mol/well, respectively) with a narrower linear range up to 5 × 10−4 mol L−1. However, the higher detectability observed with the CL device required the use of a biocomponent, i.e. HRP enzyme, while the electrochemical detection can be considered more sustainable and robust, since only phosphate solution is necessary for the measurement. Furthermore, the absence of biocomponent delivers a sensor characterized by high storage stability. This latter is a key feature for the market, because a low storage stability is very often the reason of the gap between the research field and the market: a sensor that requires low temperature for maintaining its performances and it is stable just for few days is not suitable for market entry.

5.5.3. Paper-Based Glucose Oxidase Biosensor

As reported in the introduction, glucose biosensor is without any doubts the most investigated biosensor type for its high analytical performances in terms of detectability, high working and storage stability, as well as for his utility in diabetes management. Herein, we compare sustainable paper-based devices using CL or electrochemical transduction with portable instrumentation, with the main idea that paper-based devices should be able to fit the ASSURED criteria established by WHO. Using CL configuration, the calibration curve reported in Fig. 5A showed a LOD 1.7 × 10−5 mol L−1 and linearity up to 2 × 10−3 mol L−1.

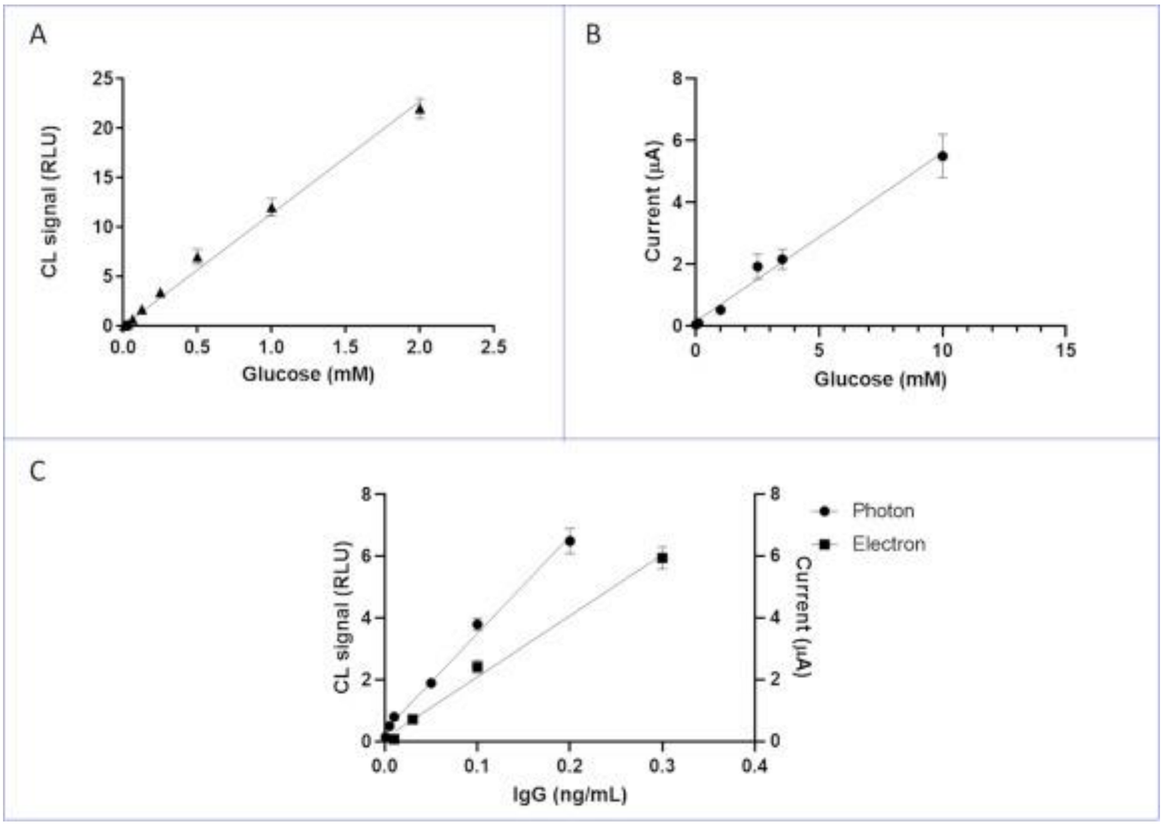

Figure5. A) Calibration curve for glucose by CL detection employing a paper-based GOx sensor and portable CCD-based instrumentation. B) Calibration curve of glucose using SPE printed on office paper and modified with CB/PBNPs combined with filter paper pad and portable instrument. C) IgG measurement by using a sandwich immunoassay with magnetic beads and CL detection D) IgG measurement by using a sandwich immunoassay with magnetic beads and SPE modified with CB.

In case of electrochemical detection, a wider linear range up to 1 × 10−2 mol L−1 was observed, described by the equation y = (0.55 ± 0.02)x + (0.2 ± 0.1), with a r2 = 0.966 and a LOD equal to 4 × 10−5 mol L−1 (Fig. 5B).

5.5.4. IgG Quantification

Being IgG the primary response of the immune system, the IgG detection furnishes a well-established analytical tool to measure infection. To enlarge the competition between photons and electrons, a typical sandwich immunosensor was designed for IgG measurement using magnetic beads as solid support for the immunological sandwich. A typical calibration curve obtained for CL detection (Fig. 5C) displays a linear portion at lower analyte concentrations, with a saturation effect at higher concentrations. From this curve, a LOD of 1.2 × 10−14 mol L−1 and a LOQ of 1.6 × 10−13 mol L−1 were calculated. In case of electrochemical detection, a LOD of 1.2 × 10−13 mol L−1 and a LOQ of 2.7 × 10−13 mol L−1 were calculated, demonstrating similar results using the same measurement time.

5.6. CONCLUSIONS

The experimental measurements performed in this paper have been carried out employing the same reagents, and, in almost all circumstances, the same conditions. In some cases, however, the optimal conditions were chosen in order to allow both methods to operate at their best possibility, according to the background of the research groups, of the availability of optimized protocols and of the instrumentation existing in their laboratories. The obtained results demonstrated that biosensors based on amperometric and CL detection principles, despite offering similar detectability and comparable analytical performance, display subtle differences in some practical experimental aspects, permitting to indicate them in complementary application fields. Generally, CL is characterized by slightly lower LOD values and wider dynamic ranges, even though this is not always confirmed, and, in all experiments, quite small differences have been observed. In particular, while comparable detectability was observed when comparing the two transduction principles in HRP detection and in enzyme- and immuno-based biosensors, significantly lower LOD and LOQ values were obtained with CL-based detection of hydrogen peroxide with respect to amperometric detection. This could be ascribed to the fact that enzyme catalysis was employed in CL-based assay, while H2O2 was directly detected at the electrode. One peculiar characteristic of CL is the higher assay sensitivity i.e. slope of the dose-response curve observed with portable devices with respect to benchtop instrumentation, as well as the possibility to extend the assay dynamic range by varying the signal acquisition time. Nevertheless, as high detectability in CL imaging is obtained at increasing acquisition times, in the order of minutes, with slow-scan cooled CCD cameras, this is a disadvantage with respect to amperometric measurements that can reach comparable LODs with shorter acquisition times. Nevertheless, this limitation will probably be soon overcome with technological advancements for enhanced CCDs, complementary metal oxide semiconductor (CMOS) and thin-film photosensors. The shorter analysis time will allocate electrochemical biosensors in the real-time monitoring such as wearable biosensors. On the other hand, CL based biosensors should be more devoted to POCT for clinical biomarkers where the detectability is more important (Roda et al., 2018). Although not explored in our experiments, multiplexing ability is also an important feature for biosensors market penetration, especially in the view of their application in personalized medicine and companion diagnostics. With this respect, both electrochemical and CL biosensors, that can be arranged in arrays (or, for CL, also exploit imaging), are suitable (Zangheri et al., 2015; Li et al., 2019). The challenge reported here from analytical point of view demonstrated that these biosensors have competitive and similar analytical features, and between photons and electrons the challenge is still open, especially when comparison is performed on the same target analyte and biosensing principle. On the contrary, significant differences can be evidenced in other applications, in which each transduction technology offers unparalleled features. Indeed, optical methods, and particularly BL/CL detection, offer unique possibilities for in vivo and ex-vivo imaging, a powerful tool for monitoring of several physiological and pathological processes, such as inflammation, tumour growth, and drug delivery. Furthermore, although still in their infancy, CL-based theragnostics could represent a relevant tool, solving the main problem of approaches heavily relying on external light, i.e. shallow tissue penetration of UV light, by exploiting CL reactions as an inner light source. On the other hand, the detection of electrons combined with printed electronics has established electrochemical biosensors as the leading technology for the delivery of wearable sensors applied in biomedical field. To this regard, the huge attention in this research field during last years is due to the endearing features of these analytical tools, which encompasses the closeness of the point of care to the patients, the smart transmission data, the cost-effectiveness, and the on line monitoring of health parameters. Hybrid amperometric and CL based biosensors could be developed taking advantages of the best analytical performance of the two principles, according to the expected analyte concentration and matrix complexity. Moreover, the electrogenerated chemiluminescence (ECL) and biosensors based on this principle are very potent analytical tools in the portable area after the tremendous success of ECL in clinical chemistry analysed using Ruthenium complexes, (which releases a photon at ~620 nm) regenerating with excess of the co-reactant tripropylamine (Babarniri et al., 2019). Therefore, we use an electrochemical process to trigger the light emission by generating a molecule its singlet excited state and we measure the photon emitted with a simple CCD or CMOS. Surprisingly ECL combines both electrons and photons in a different way but offers high potentiality in terms of simplicity and applicability in new generation of biosensors. Of course, the extraordinary detectability of ECL using the co-reactant derived from the cyclic amplification due to the excess of tripropylamine. Other ECL systems using for example luminol and platinum-gold alloy hybrid functionalized zinc oxide nanocomposites present similar analytical performance of the CL Systems (Huang et al., 2018a). In conclusion, electrochemisty and CL based biosensors offer similar performance in terms of sensitivity that are superior to other transduction principles such as for example optical and photoluminescence. Differences among them often reported are related mainly to the optimization of the assay conditions, reagents used and analytical procedure.

REFERENCES

A. Abbaspour, F. NorouzSarvestani, A. Noori, N. Soltani,Biosens.Bioelectron., 68 (2015), pp. 149-155

H.O. Albrecht, Chemical, 136 (1928), pp. 321-330

A. Ambrosi, C.K. Chua, B. Khezri, Z. Sofer, R.D. Webster, M. Pumera, Proc. Natl. Acad. Sci. Unit. States Am., 109 (2012), pp. 12899-12904

A. Ambrosi, S.Y. Chee, B. Khezri, R.D. Webster, Z. Sofer, M. Pumera, Angew. Chem., Int., 51 (2012), pp. 500-503

A. Ambrosi, C.K. Chua, A. Bonanni, M. Pumera, Chem. Rev., 114 (2014), pp. 7150-7188

L.A. Andronico, L. Chen, M. Mirasoli, M. Guardigli, A. Quintavalla, M. Lombardo, C. Trombini, D.T. Chiu, A. Roda, Nanoscale, 10 (29) (2018), pp. 14012-14021

F. Arduini, S. Cinti, V. Caratelli, V. Amendola,Biosens.Bioelectron., 126 (2019), pp. 346-354

F. Arduini, D. Neagu, S. Dall'Oglio, D. Moscone, G. Palleschi,Electroanalysis, 24 (3) (2012), pp. 581-590

F. Arduini, F. DiNardo, A. Amine, L. Micheli, G. Palleschi, D. Moscone,Electroanalysis, 24 (4) (2012), pp. 743-751

B. Babarniri, D. Bahari, A. Salimi, Biosens. Bioelectron., 142 (2019), p. 111530

A. Bonanni, C.K. Chua, G. Zhao, Z. Sofer, M. Pumera,ACSNano, 6 (10) (2012), pp. 8546-8551

R.L. Campbell, D.B. Wagner, J.P. O'Connel, Solid-phase Assay with Visual Readout(1987), US Pat. 4,703,017

N.A. Choudry, D.K. Kampouris, R.O. Kadara, C.E. Banks,Electrochem.Commun., 12 (1) (2010), pp. 6-9

S. Cinti, F. Arduini, G. Vellucci, I. Cacciotti, F. Nanni, D. Moscone,Electrochem. Commun., 47 (2014), pp. 63-66

S. Cinti, D. Neagu, M. Carbone, I. Cacciotti, D. Moscone,Electrochim.Acta, 188 (2016), pp. 574-581

S. Cinti, D. Talarico, G. Palleschi, D. Moscone, F. Arduini,Anal.Chim.Acta, 919 (2016), pp. 78-84

S. Cinti, E. Proietti, F. Casotto, D. Moscone, F. Arduini, Anal.Chem., 90 (22) (2018), 13680-13686

S. Cinti, D. Moscone, F. Arduini, Nat. Protoc., 14 (8) (2019), pp. 2437-2451

G. Cui, J.H. Yoo, J.S. Lee, J. Yoo, J.H. Uhm, G.S. Cha, H. Nam, Analyst, 126 (2001), pp. 1399-1403

M. DiFusco, A. Quintavalla, M. Lombardo, M. Guardigli, M. Mirasoli, C. Trombini, A. Roda, Anal. Bioanal. Chem., 407 (2015), pp. 1567-1576

D. Du, L. Wang, Y. Shao, J. Wang, M.H. Engelhard, Y. Lin, Anal. Chem., 83 (2011), pp. 746-752

M. Di Fusco, A. Quintavalla, M. Lombardo, M. Guardigli, M. Mirasoli, C. Trombini, A. Roda, Anal. Bioanal. Chem., 407 (2015), pp. 1567-1576

D. Du, L. Wang, Y. Shao, J. Wang, M.H. Engelhard, Y. Lin, Anal. Chem., 83 (2011), pp. 746-752

W. Dungchai, O. Chailapakul, C.S. Henry, Anal. Chem., 81 (14) (2009), pp. 5821-5826

A. Escarpa, Chem. Rec., 12 (2012), pp. 72-91

P. Fanjul-Bolado, D. Hernández-Santos, P. José Lamas-Ardisana, A. Martín-Pernía, A. Costa-García, Electrochim. Acta, 53 (2008), pp. 3635-3642

F. Ghamouss, P.Y. Tessier, M.A. Djouadi, M.P. Besland, M. Boujtita, Electrochem. Commun., 9 (7) (2007), pp. 1798-1804

M.S. Goh, M. Pumera, Anal. Chem., 82 (2010), pp. 8367-8370

W.J. Guan, Y. Li, Y.Q. Chen, X.B. Zhang, G.Q. Hu, Biosens. Bioelectron., 21 (2005), pp. 508-512

N. Hananya, A. Eldar Boock, C.R. Bauer, R. Satchi-Fainaro, D. Shabat, J. Am. Chem. Soc., 138 (2016), pp. 13438-13446

X. Huang, X. Deng, W. Qi, D. Wu, Sensor. Actuator. B Chem., 273 (2018), pp. 466-472

Y. Huang, L. Gao, H. Cui, ACS Appl. Mater. Interfaces, 10 (20) (2018), pp. 17040-17046

M. Iinuma, Y. Kadoya, A. Kuroda, Methods Mol. Biol., 1461 (2016), pp. 299-310

J.H. Im, H.R. Kim, B.G. An, Y.W. Chang, M.J. Kang, T.G. Lee, J.G. Son, J.G. Park, J.C. Pyun, Biosens. Bioelectron., 92 (2017), pp. 221-228

G. Inzelt, A. Lewenstam, F. ScholzHandbook of Reference Electrodes, Springer (2013)

D.J. Ives, G.J. JanzReference Electrodes, Academic Press, New York (1961), p. 179

R.O. Kadara, N. Jenkinson, C.E. Banks, Electrochem. Commun., 11 (2009), pp. 1377-1380

D.K. Kampouris, C.E. Banks, Chem. Commun., 46 (2010), pp. 8986-8988

F. Li, J.C. Liu, L. Guo, J.H. Wang, K.Q. Zhang, J.B. He, H. Cui, Biosens. Bioelectron., 141 (2019), p. 111472

N. Li, D. Liu, H. Cui, Anal. Bioanal. Chem., 406 (23) (2014), pp. 5561-5571

X. Li, B. Liu, X. Hun, Sensor. Actuator. B Chem., 277 (2018), pp. 510-516

Y. Lin, F. Lu, J. Wang, Electroanalysis, 16 (2004), pp. 145-149

P. Ling, J. Lei, L. Jia, H. Ju, Chem. Commun., 52 (6) (2016), pp. 1226-1229

T. Ma, M. Zhang, Y. Wan, Y. Cui, L. Ma, Micromachines, 8 (5) (2017), p. 149

E. Marzocchi, S. Grilli, L. Della Ciana, L. Prodi, M. Mirasoli, A. Roda, Anal. Biochem., 377 (2) (2008), pp. 189-194

V. Mazzaracchio, D. Neagu, Al Porchetta, E. Marcoccio, A. Pomponi, G. Faggioni, N. D'Amore, A. Notargiacomo, M. Pea, D. Moscone, G. Palleschi, F. Lista, F. Arduini, Biosens. Bioelectron., 126 (2019), pp. 640-646

M. Mirasoli, F. Bonvicini, N. Lovecchio, G. Petrucci, M. Zangheri, D. Calabria, F. Costantini, A. Roda, G. Gallinella, D. Caputo, G. de Cesare, A. Nascetti, Sensor. Actuator. B Chem., 262 (2018), pp. 1024-1033

M. Mirasoli, M. Guardigli, E. Michelini, A. Roda, J. Pharmaceut. Biomed. Anal., 87 (2014), pp. 36-52

M. Mirasoli, A. Nascetti, D. Caputo, M. Zangheri, R. Scipinotti, L. Cevenini, G. de Cesare, A. Roda, Anal. Bioanal. Chem., 406 (2014), pp. 5645-5656

D. Moscone, D. D'Ottavi, D. Compagnone, G. Palleschi, A. Amine, Anal. Chem., 73 (2001), pp. 2529-2535

A. Morrin, J. Killard, M.R. Smyth,Anal. Lett., 36 (2003), pp. 2021-2039

M. Nakazono, Y. Oshikawa, M. Nakamura, H. Kubota, S. Nanbu, J. Org. Chem., 82 (5) (2017), pp. 2450-2461

A. Nascetti, M. Mirasoli, E. Marchegiani, M. Zangheri, F. Costantini, A. Porchetta, L. Iannascoli, N. Lovecchio, D. Caputo, G. de Cesare, S. Pirrotta, A. Roda, Biosens. Bioelectron., 123 (2019), pp. 195-203

J.M. Park, H.W. Jung, Y.W. Chang, H.S. Kim, M.J. Kang, J.C. Pyun, Anal. Chim. Acta, 853 (2015), pp. 360-367

J. Ping, Y. Wang, K. Fan, J. Wu, Y. Ying,Biosens. Bioelectron., 28 (2011), pp. 204-209

M. Rezazadeh, S. Seidi, M. Lid, S. Pedersen-Bjergaard, Y. Yamini, TrAC-trend. Anal. Chem., 118 (2019), pp. 548-555

A. Roda, E. Michelini, C. Caliceti, M. Guardigli, M. Mirasoli, P. Simoni, Anal. Bioanal. Chem., 410 (3) (2018), pp. 669-677

A. Roda, M. Mirasoli, L.S. Dolci, A. Buragina, F. Bonvicini, P. Simoni, M. Guardigli,Anal. Chem., 83 (2011), pp. 3178-3185

A. Roda, M. Mirasoli, E. Michelini, M. Di Fusco, M. Zangheri, L. Cevenini, B. Roda, P. Simoni,Biosens. Bioelectron., 76 (2016), pp. 164-179

A. Roda, M. Zangheri, D. Calabria, M. Mirasoli, C. Caliceti, A. Quintavalla, M. Lombardo, C. Trombini, P. Simoni, Sensor. Actuator. B Chem., 279 (2019), pp. 327-333

I.Y. Sakharov, M.M. Vdovenko, Anal. Biochem., 434 (2013), pp. 12-14

G. Scordo, D. Moscone, G. Palleschi, F. Arduini, Sensor. Actuator. B Chem., 258 (2018), pp. 1015-1021

S.J. Setford, R.M. Van Es, Y.J. Blankwater, S. Kröger,Anal. Chim. Acta, 398 (1999), pp. 13-22

A.P. Schaap, R.S. Handley, B.P. Giri, Tetrahedron Lett., 28 (1987), pp. 935-938

J. Shu, Z. Han, H. Cui,Anal. Bioanal. Chem., 411 (18) (2019), pp. 4175-4183

S. Singh, D.V.S. Jain, M.L. Singla, Sensor. Actuator. B., 182 (2013), pp. 161-169

R.R.G. Soares, D.R. Santos, V. Chu, A.M. Azevedo, M.R. Aires-Barros, J.P. Conde, Biosens. Bioelectron., 87 (2017), pp. 823-831

S. Tang, P. Tong, W. Lu, J. Chen, Z. Yan, L. Zhang, Biosens. Bioelectron., 15 (59) (2014), pp. 1-5

A. Tiwari, S.J. Dhoble, Talanta, 180 (2018), pp. 1-11

D.M. Wang, K.L. Lin, K.Z. Huang, Luminescence, 34 (2019), pp. 4-22

J. Wang, M. Musameh, Analyst, 129 (1) (2004), pp. 1-2

J. Wang, M. Pedrero, H. Sakslund, O. Hammerich, J. Pingar-ron, Analyst, 121 (1996), pp. 345-350

J. Wang, B. Tian, V.B. Nascimento, L. Angnes, Electrochim. Acta, 43 (1998), pp. 3459-3465

J. Wang, W.H. Zhong, X.Y. Liu, T.T. Yang, F. Li, Q. Li, W.R. Cheng, C. Gao, Z. Jiang, J. Jiang, H. Cui, Anal. Chem., 89 (24) (2017), pp. 13518-13523

T. Wang, E.P. Randviir, C.E. Banks, Analyst, 139 (2014), pp. 2000-2003

H. Wei, J.J. Sun, Y. Xie, C.G. Lin, Y.M. Wang, W.H. Yin, G.N. Chen, Anal. Chim. Acta, 588 (2007), pp. 297-303

Y.J. Yoon, K.H.H. Li, Y.Z. Low, J. Yoon, S.H. Ng, Sensor. Actuator. B Chem., 198 (2014), pp. 233-238

M. Zangheri, F. Di Nardo, L. Anfossi, C. Giovannoli, C. Baggiani, A. Roda, M. Mirasoli, Analyst, 140 (2015), pp. 358-365

M. Zangheri, F. Di Nardo, M. Mirasoli, L. Anfossi, A. Nascetti, D. Caputo, G. De Cesare, M. Guardigli, C. Baggiani, A. Roda, Anal. Bioanal. Chem., 408 (2016), pp. 8869-8879

M. Zangheri, M. Mirasoli, M. Guardigli, F. Di Nardo, L. Anfossi, C. Baggiani, P. Simoni, M. Benassai, A. Roda, Biosens. Bioelectron., 129 (2019), pp. 260-268

Z.F. Zhang, H. Cui, C.Z. Lai, L.J. Liu, Anal. Chem., 77 (2005), pp. 3324-3329

H. Zhang, M. Liu, G. Huang, Y. Yu, W. Shen, H. Cui, J. Mater. Chem. B, 1 (2013), pp. 970-977

N. Zhu, L. Gu, J. Wang, X. Li, G. Liang, J. Zhou, Z. Zhang, J. Phys. Chem. C, 123 (2019), pp. 9388-9393

G.Y. Zhu, X.D. Yin, D.L. Jin, B. Zhang, Y.Y. Gu, Y.R. An, TrAC-trend. Anal. Chem, 111 (2019), pp. 100-117

6

IN-PARALLEL POLAR MONITORING OF CHEMILUMINESCENCE EMISSION ANISOTROPY AT THE SOLID–LIQUID INTERFACE BY AN OPTICAL FIBER RADIAL ARRAY

Reproduced from: "In-Parallel Polar Monitoring of Chemiluminescence Emission Anisotropy at the Solid–Liquid Interface by an Optical Fiber Radial Array?"
Simone Berneschi, Cosimo Trono, Mara Mirasoli, Ambra Giannetti, Martina Zangheri, Massimo Guardigli, Sara Tombelli, Elisa Marchegiani, Francesco Baldini, Aldo Roda
Chemosensors, 2020,8, 18
Reproduced by permission of The Royal Society of Chemistry
https://www.mdpi.com/2227-9040/8/1/18

6.1. INTRODUCTION

Chemiluminescence (CL, i.e., the light emission originating from a strongly exergonic chemical reaction yielding a product in its electronically excited state) is an optical detection method which, due to its intrinsic characteristics, is gaining a growing interest in the development of high-performance biosensing devices [1–3]. In fact, when compared to other optical detection principles, such as absorption or fluorescence, CL offers considerable advantages including a high detectability even in low volumes, due to the possibility of producing photons "in the dark", thus minimizing any other nonspecific signal contribution coming from excitation photons and maximizing the resulting signal-to-noise ratio. As the CL light signal is the result of a chemical reaction, no external source, together with the connected filtering apparatus, is requested. All these features can lead to the development of very simple and miniaturized analytical devices [4–7]. In many bioanalytical applications, such as the CL-based enzyme-linked immunoassay, the CL reaction is catalyzed by an enzyme conjugated with a bio-specific capture element bound on a solid surface (e.g., glass, polymer, or paper) [8–12]. This means that the light-emitting product of the CL enzymatic reaction can be represented as a whole as an electromagnetic dipole emitter generated in the proximity of a surface. The anisotropic emission of electric and/or magnetic dipoles, when the distance from a dielectric interface is small or comparable with the emitted wavelength, is a well-known phenomenon [13–19]. Indeed, when a light emitter is located at the interface between two dielectric media with different refractive indexes (n1 and n2, with n2 > n1), the majority of the light signal propagates in the denser medium with higher refractive index (n2) at angles θ above the critical angle θ_c ($\theta_c=\sin^{-1}(n1/n2)$) [18].

If the denser medium is a substrate with flat and parallel faces (e.g., a microscope slide), most of the emitted light will propagate through successive total internal reflections inside the substrate. In the case of a fluorescence signal, this propagation regime beyond the critical angle is called supercritical angle fluorescence (SAF). The other contribution to the overall emission is represented by the refracted light, which is emitted at angles below the critical angle c, generally referred to as undercritical angle fluorescence (UAF) [20–23]. Therefore, while it is possible to collect the UAF contribution by placing a detector close to the bottom face of the substrate, the same cannot be done for the SAF component, which, by its nature, is undetected because it remains trapped inside the denser medium. Consequently, this phenomenon must be taken into serious consideration in order to optimize the signal collection efficiency of optical devices and increase their performance in terms of sensitivity [18,24–29]. Although the anisotropic emission has been deeply investigated for fluorescence emitters, the same cannot be said for CL reactions. In the case of CL reactions, the emission phenomenon is even more complicated because, even if the catalyzing enzyme is immobilized on the solid surface, the excited-state product of the reaction could diffuse in the solution prior to the photon emission [30]. Therefore, depending on the properties of the emitter (i.e., excited-state lifetime and diffusion coefficient), light emission does not necessarily take place in proximity of the surface. Evidence of a strongly polarized and directional emission has been reported by M.H. Chowdhury et al. in their studies on surface plasmon-coupled chemiluminescence (SPCC), where the light radiation produced by a CL reaction in solution was coupled to the surface plasmons in glass slides coated with a metal thin film. The authors attributed the nature of this emission to the surface plasmons, rather than to the luminophores themselves. For such studies, the authors developed a rotary stage in which a single optical fiber connected to a spectrometer collected the light at a given angle around the sample chamber [31,32], with the limitation of a time-consuming polar scanning. In this work we propose a simple method for the real-time evaluation of the emission anisotropy of CL enzyme reactions at the liquid–solid interface, based on an array of plastic multimode optical fibers. The optical fibers are radially placed at fixed polar angles to monitor, as a function of the angle, the CL signal intensity. The input face of each fiber is embedded in a plastic semicylinder while the other face is imaged by a CCD camera though a suitable interface. Experiments were conducted by using two different enzymes, namely horseradish peroxidase (HRP) and alkaline phosphatase (ALP), immobilized on a poly(methyl methacrylate) (PMMA) slide (heterogeneous configuration), as well as using HRP in solution (homogeneous configuration). Evidence of the anisotropy phenomenon is reported for all the cases examined. As it will be shown in the experimental section, HRP and ALP in the heterogeneous configuration, although showing different kinetics of the CL reactions, displayed similar polar distributions of their emission, while a time-dependent behaviour of the polar distribution was evidenced for HRP in the homogeneous configuration.

6.2. MATERIALS AND METHODS

6.2.1. Optical Setup and Methods

Figure 1 sketches the experimental setup adopted for collecting the CL signal and studying its behavior at the interface in terms of emission anisotropy (i.e., polar distribution of the emission). All transparent elements were made of PMMA, with a mean refractive index nPMMA = 1.50 in the 420–

480 nm wavelength interval (the HRP- and ALP-catalyzed CL emissions have maxima at about 425 and 470 nm, respectively).

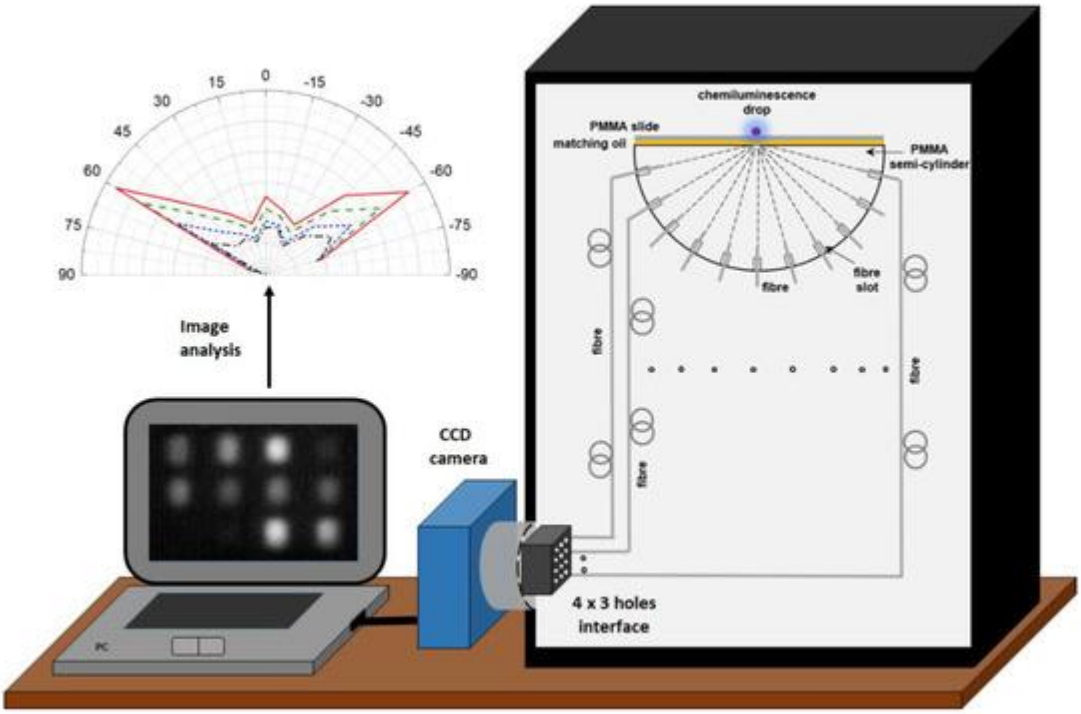

Figure 1. Sketch of the experimental setup adopted for the real-time detection of the chemiluminescence (CL) signal.

Multimode PMMA optical fibers Broadcom HFBR-RUS100Z (Broadcom, San Jose, CA, USA) were used, characterized by a diameter of 1 mm and a numerical aperture (NA) of 0.47 and cut in pieces 60 cm in length. The ends of each fiber were accurately polished by means of a lapping machine, using aluminum oxide and silicon carbide abrasive disks with different grind size from 12 μm down to 0.3 μm (Buehler FibrMet Disc, PSA Backed, 4″). All Buehler products were obtained from Buehler (Lake Bluff, IL, USA). A PMMA semicylinder was obtained by cutting a PMMA rod (35 mm in length, 40 mm in diameter) along a plane parallel to the cylinder axis and 1 mm far from it (see Figure 2). The obtained rectangular flat top surface (35 mm × 40 mm) was manually polished by using a nonabrasive cloth (Buehler microcloth PSA 2-7/8″) and colloidal diamond suspension (Buehler MetaDiTM Supreme–

Polycrystalline Diamond Suspension) with a grit of 0.25 μm. The semicylinder block was then drilled in correspondence with its circular outer surface in order to realize eleven radial cylindrical holes (1.1 mm in diameter, 4 mm in depth) with a constant azimuthal angular spacing of 15°, necessary to house the input ends of the optical fibers used for CL signal collection. The fibers were glued inside the holes with the NOA 68 optical glue (Norland Products Inc., Cranbury, NJ, USA).

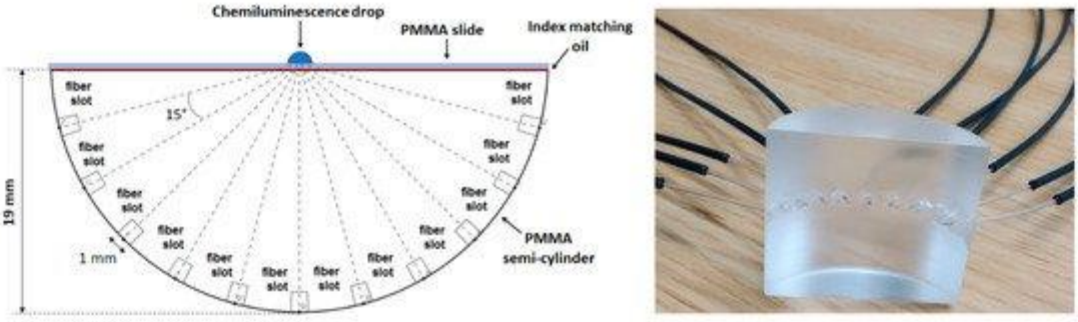

Figure 2. Detail of the poly(methyl methacrylate) (PMMA) semicylinder with the angular displacement of the 11 fibers (not in scale). On the right is a photo of the semicylinder.

A PMMA slide (microfluidic ChipShop, Jena, Germany), with a thickness of 1 mm, was set on the top of the PMMA semicylinder and used as support for the CL reaction. With reference to Figure 2, considering that the height of the semicylinder is 19 mm (i.e., 1 mm less than the cylinder radius), the upper surface of the 1-mm-thick slide will be coincident with the cylinder axial plane. During the experiments, a refractive index matching oil (pure glycerol from Sigma-Aldrich, St. Louis, MO, USA, with a refractive index nOIL = 1.48) was used to improve the optical coupling condition of the PMMA slide with the underlying PMMA semicylinder. The optical configuration allowed the maximum efficiency of light collection by optical fibers. Indeed, if r = 0.5 mm is the radius of the optical fiber and D = 16 mm is the distance between the fiber face and the CL drop, the acceptance angle, or angular resolution, for every fiber, assuming a point emitter placed on the semicylinder axis, can be calculated as:

$$2tan^{-1}\left(\frac{r}{D}\right) = 3.58°$$

This value of the acceptance angle is under the numerical aperture of the fiber, so all the light reaching the fiber input end will be conveyed to the CCD camera. The eleven optical fiber output ends were fixed in the holes of a support obtained by drilling a parallelepiped of black polyvinylchloride (PVC) polymer (17 mm × 13 mm × 10 mm, see Figure 1) to obtain a 4 × 3 holes matrix (1.1 mm diameter, 5 mm spacing). Such support acted as an interface between the collecting system (PMMA semicylinder and plastic fibers) and the imaging detector (cooled MZ-2PRO CCD camera, MagZero, Pordenone, Italy) equipped for lensless contact imaging through a round fiber optic taper (25 to 11 mm, Edmund Optics, Barrington, NJ, USA) placed in contact with the CCD sensor [33]. Since each position in the 4 × 3 holes matrix of the support corresponded to a specific optical fiber, the CL emissions at different angles can be acquired independently and simultaneously (the twelfth position of the matrix was used to measure the background signal of the CCD camera). The measurements were performed inside a black box to avoid any spurious light contribution from the environment that could interfere with the measurement.

6.2.2. Reagents and Reaction Protocols

The enzymes HRP (type VI-A, from horseradish) and ALP (from bovine intestinal mucosa) were purchased from Sigma-Aldrich. Enzyme solutions were prepared in 0.1 M phosphate-buffered saline (PBS), pH 7.7. The Super Signal ELISA Femto CL cocktail for HRP was purchased from Thermo Fisher Scientific (Rockford, IL, USA), while the Lumiphos Plus CL cocktail for ALP was from Lumigen (Southfield, MI, USA). Figure 3 illustrates the heterogeneous and homogeneous configurations adopted in the experiments for measuring the polar distribution of the emission from enzyme-catalyzed CL reactions. For enzyme immobilization (heterogeneous configuration), the PMMA slides were first functionalized by one-minute dip-coating in a 2 mM Eudragit L100 copolymer (Evonik Degussa GmbH, Düsseldorf, Germany) ethanol solution, then air-dried to form a polymeric thin film on the surface. Eudragit L100 is an anionic copolymer made of methacrylic acid and methyl methacrylate used to provide carboxylic (–COOH) functional groups for the binding of biospecific molecules. The slide surfaces were activated with 2 mM 1-ethyl-3-[3-dimethylaminopropyl] carbodiimide hydrochloride (EDC) and 5 mM N-hydroxysuccinimide (NHS) (Thermo Fisher Scientific). Then, 1 µL of 1 µg/mL enzyme solution (HRP or ALP) was deposited on the activated PMMA slide surface and incubated for 1 h in a humid chamber at room temperature. The slides were then thoroughly washed with PBS and dried under a nitrogen stream.

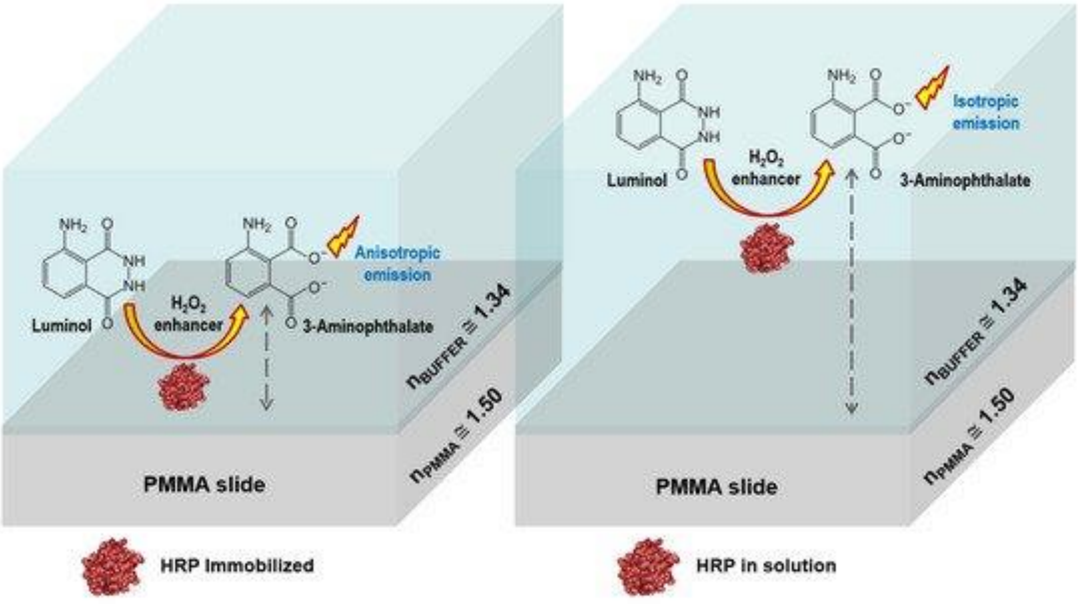

Figure 3. Sketch of the CL reaction performed with the enzyme either immobilized onto the PMMA slide (heterogeneous configuration, left part of the figure) or free in solution (homogeneous configuration, right part of the figure). The grey dashed lines represent the distances of the light-emitting molecule from the surface.

For the measurement, the slide was positioned on the PMMA semicylinder with the spot of immobilized enzyme placed in correspondence with the focus of the optical collecting system, univocally identified by the axis of the PMMA semicylinder and the plane of the fibers. Then, 10 µL of CL cocktail (Super Signal ELISA Femto or Lumiphos Plus for HRP or ALP, respectively) were added and CL images were acquired. A similar procedure was adopted for the measurements in the homogeneous configuration, except for the fact that pristine PMMA slides were used. For each measurement, 1 µL of 10 ng/mL HRP enzyme solution and 9 µL of Super Signal ELISA Femto CL cocktail were dispensed on the slide in correspondence with the focus of the optical collecting system and CL images were acquired.

6.2.3. Signal Acquisition and Processing

Images (grayscale images, 16-bit depth in the FITS file format) were acquired at regular time intervals employing a 5-s integration time and analyzed with the freely available open source ImageJ software [34]. The overall signal of each spot (corresponding to a fiber output end and, therefore, proportional to the CL emission intensity at the polar angle of the fiber) was evaluated by integration over the whole spot area. An example of a frame is reported in Figure 4.

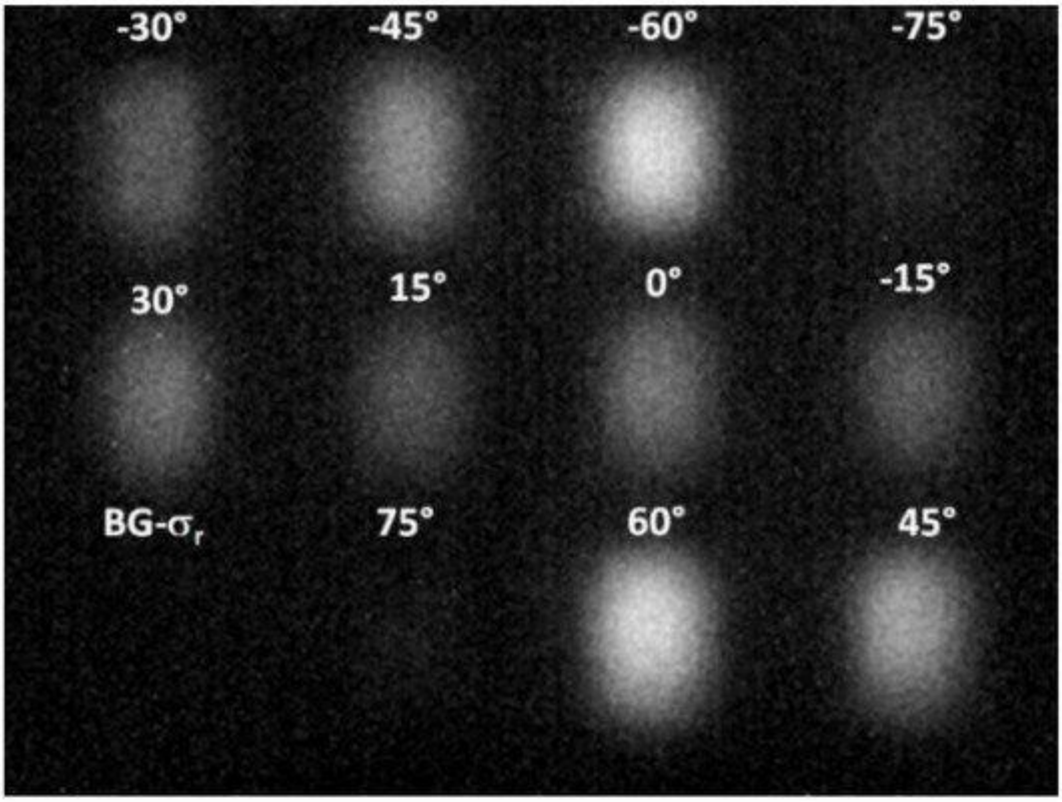

Figure 4. Image of the ends of the eleven fibers as measured for the CL reaction in the heterogeneous configuration. The twelfth point (bottom left), indicated with BG-σ_r, was used for the background and the statistical relative error estimation.

The twelfth position of the matrix, indicated in Figure 4 as BG- σ_r, was used to measure the background signal of the CCD camera and for the estimation of the statistical relative error σ_r of the measurements, calculated as the standard deviation–average signal ratio of said point.

6.3. RESULTS AND DISCUSSION

6.3.1. Chemiluminescence Systems

Chemiluminescent measurements were performed by using the CL reactions catalyzed by HRP or ALP enzymes, which are widely used in bioanalytical applications, in particular in enzyme-based assays and in binding assays such as gene probe hybridization and immunoassays.

Calf intestinal ALP is a 160 kDa enzyme often detected by means of 1,2-dioxetane derivatives as enzymatic substrates. In this work, the Lumiphos Plus CL cocktail for ALP containing 4-methoxy-4-(3-phosphatephenyl)spiro[1,2-dioxetane-3,2′-adamantane] disodium salt (AMPPD) and an enhancer (which increases the duration and intensity of the emission) was employed. The catalytic action of the enzyme on AMPPD results in dephosphorylation of the aryl phosphate moiety of the dioxetane with subsequent cleavage of the 1,2-dioxetane ring and production of a phenolate moiety in its excited state [35]. Horseradish peroxidase, which is largely employed in bioanalytical assays owing to its rather small dimension (44 kDa) and high turnover rate, catalyzes the oxidation reaction of luminol, which produces 3-aminophthalate in its excited state. In this work, a commercial CL cocktail containing an N-alkylated phenothiazine enhancer and 4-morpholinopyridine as the acylation catalyst was employed. These molecules are added to the system to increase the enzyme turnover number and the equilibrium concentration of the key intermediate luminol radical anion, providing more intense and prolonged light emission [36].

6.3.2. Heterogeneous Configuration

In the heterogeneous configuration, the enzyme, either ALP or HRP, was immobilized onto the Eudragit functionalized PMMA slide. A drop of CL reaction cocktail was then deposited on the surface of the slide in correspondence with the axis of the optical collecting system (Figure 2). A representative CL image acquired by the CCD camera is depicted in Figure 4. The elliptical shape of the spots is generated by a slight distortion introduced by the fiber taper adapter, considering also that the end of the taper is about 2 mm distant from the camera sensor. Figure 5a shows the kinetic profile of the emission obtained for ALP immobilized on the PMMA surface (i.e., the sum of the signals collected by the eleven fibers). The error bars were calculated considering the relative standard deviation σr = 1% calculated on the 15 samples acquired in the BG-σr point. The intensity of the CL emission increases with time in accordance to the typical kinetics of the CL reaction of 1,2-dioxetane substrates catalyzed by ALP. Indeed, such reactions usually show slow emission kinetics, and the CL signal often reaches a plateau 20–30 min after the start of the reaction [37]. A similar behavior can be observed in Figure 5b where the CL emissions at the various angles (i.e., the average of the signals measured for each couple of fibers at symmetrical angles) are reported as a function of time.

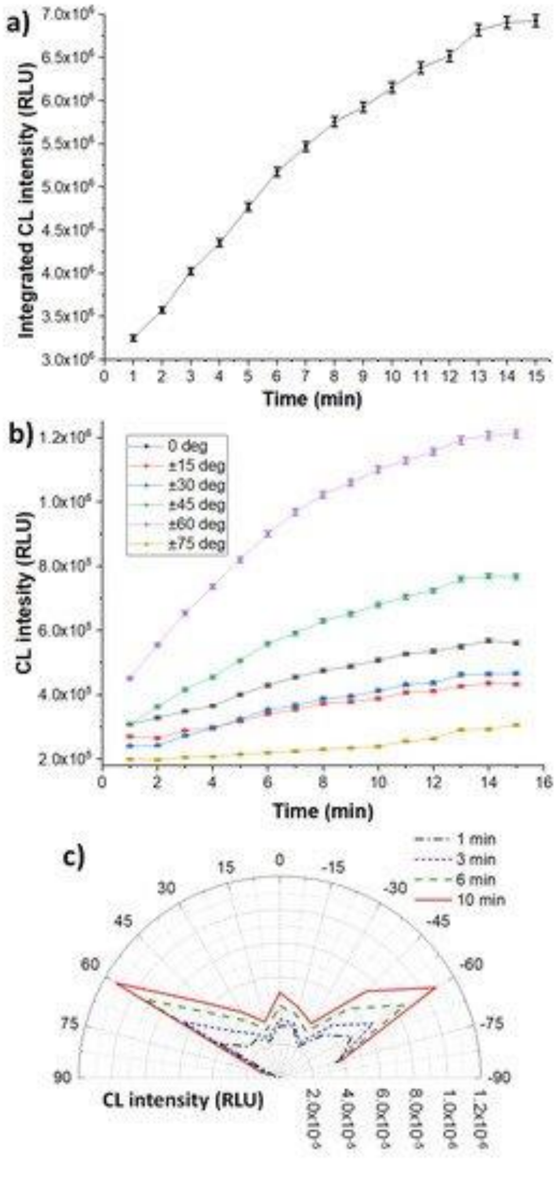

Figure 5. Kinetic profiles of the CL emission with immobilized horseradish peroxidase alkaline phosphatase (ALP): (**a**) CL emission integrated on the whole flat angle; (**b**) average CL emission per angle; (**c**) polar distribution of the CL emission.

Figure 5b clearly shows that the intensity of the CL emission also depends on the polar angle. Indeed, the CL emission is strongly anisotropic (Figure 5c), with maxima at ±60° angles that are very close to the critical angle of the PMMA–buffer interface ($\theta c_{,PMMA-buffer} = \sin^{-1}(1.34/1.50) \cong 63°$). This indicated that the CL emission occurs, on average, close to the PMMA surface, in particular within a distance from the surface less than or comparable with the CL emission wavelength (i.e., around 470 nm). Thus, the lifetime of the excited product of the enzyme-catalyzed reaction is significantly shorter than the time required for its diffusion far from the surface. As expected, the polar distribution remains practically unchanged over time, demonstrating that the CL emission occurs close to the PMMA surface for the entire duration of the reaction. In the case of immobilized HRP, the kinetic profile of the overall CL emission (Figure 6a) is quite different, since the maximum emission intensity is immediately reached, then the signal decreases with time. Again, the behaviour is in line with the typical kinetics of the luminol/peroxide/enhancer CL system in the presence of HRP, characterized by a rapid onset of the CL emission followed by a gradual decrease due to reagent consumption and enzyme degradation caused by the CL radical reaction [37].

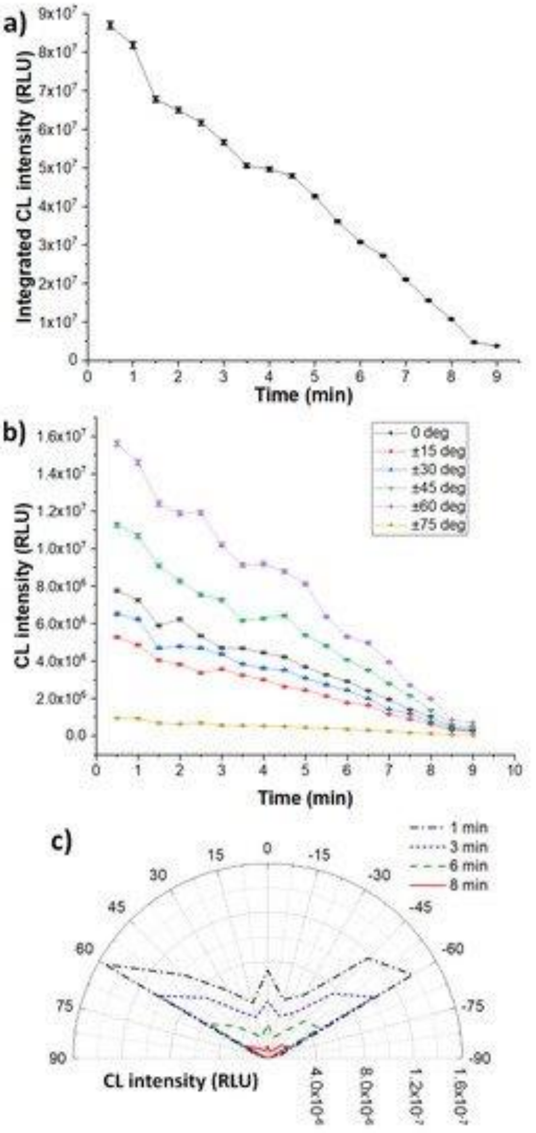

Figure 6. Kinetic profiles of the CL emission with immobilized horseradish peroxidase (HRP): (**a**) CL emission integrated on the whole flat angle; (**b**) average CL emission per angle; (**c**) polar distribution of the CL emission.

The kinetic profiles of the CL signals measured at the two symmetrical angles are reported in Figure 6b, while the resulting polar distribution of the emission at different times is depicted in Figure 6c. The error bars were calculated considering the relative standard deviation $\sigma_r = 1\%$ calculated for the 18 samples acquired in the BG-σ_r point. As already observed for the immobilized ALP, the CL emission is markedly anisotropic and the maximum emission is at ±60° angles, again confirming the proximity of the CL emitters to the PMMA surface.

Figure 7 shows the comparison between the polar distributions of the CL emissions observed for immobilized ALP and HRP. It is evident that the emissions display the same anisotropy independently from the catalyzing enzyme and the absolute intensity of the emission.

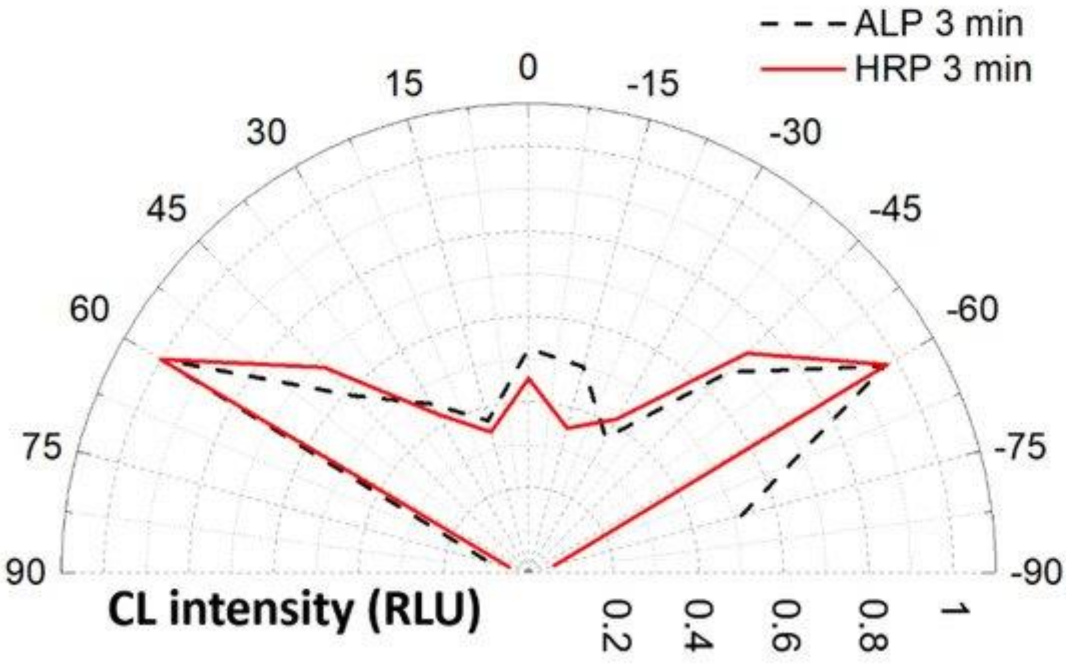

Figure 7. Comparison of the normalized polar distribution of CL emissions obtained for immobilized ALP and HRP.

6.3.3. Homogeneous Configuration

The CL emission in the homogeneous configuration was investigated to demonstrate that the employed measurement system was able to correctly differentiate between isotropic and anisotropic CL emission. In this configuration, the CL reaction cocktail containing the enzyme HRP was deposited onto pristine PMMA slide in the same position defined by the axis of the optical detection system. As far as the HRP in solution is concerned, the kinetic profile of the CL emission is quite similar to that of the immobilized HRP (Figure 8a). However, the kinetic profiles of the CL signals measured at the two symmetrical angles (Figure 8b) and the resulting polar distribution of the emission at different times (Figure 8c) display a different behaviour. The error bars were calculated considering the relative standard deviation σ_r = 1% calculated for the 18 samples acquired in the BG-σ_r point. Indeed, as expected, the CL emission is almost isotropic at short reaction times, according to the fact that the CL emitters produced by the chemical reaction are homogeneously distributed in the solution volume. However, with increasing time, the intensity of the CL emission decreases while its polar distribution evolves to anisotropy, becoming similar to that observed for HRP in the heterogeneous configuration. This can be reasonably due to the gradual absorption of HRP onto the PMMA surface, which moves the average reaction/emission volume closer to the surface. Indeed, it has been reported that protein adsorption on the surface of pristine PMMA, which occurs through interaction of the hydrophobic domains of the protein with the polymer surface, is quite fast, reaching a significant degree of surface coverage after only 10 min of incubation [38,39]. This observation demonstrated the possibility to use the developed system to monitor the absorption of the HRP enzyme on a surface in real time.

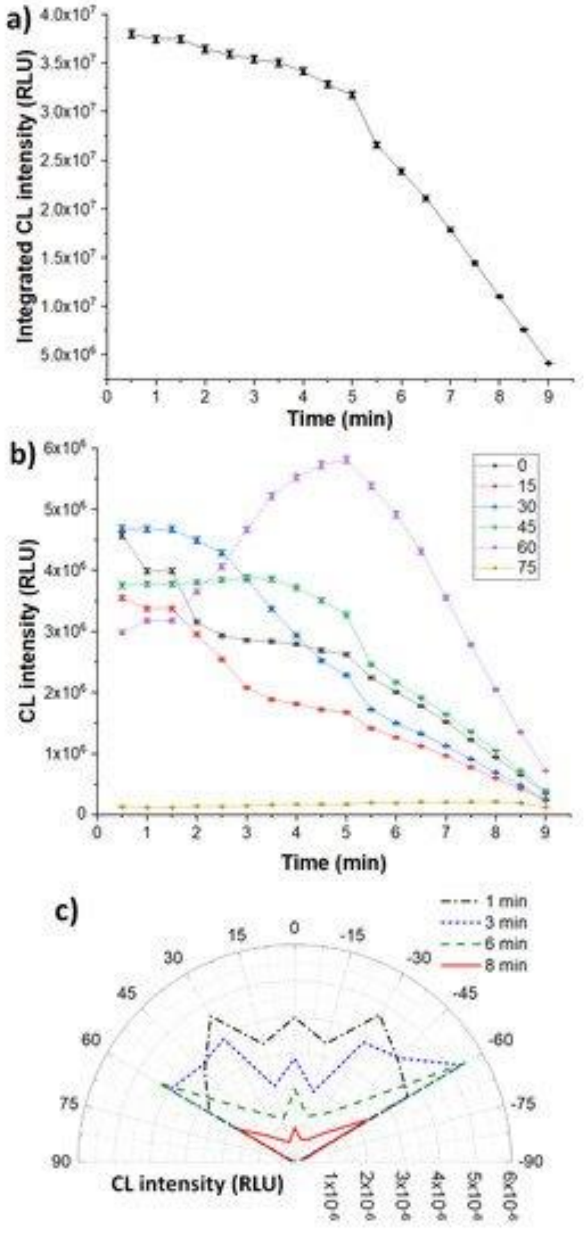

Figure 8. Kinetic profiles of the CL emission with HRP free in solution: (**a**) CL emission integrated on the whole flat angle; (**b**) average CL emission per angle; (**c**) polar distribution of the CL emission.

6.4. CONCLUSIONS

In this manuscript, an optical detection methodology for the real-time polar monitoring of CL emission has been described. The optical device consisted of a PMMA semicylinder with a radial array of eleven collecting optical fibers. The output ends of the fibers were faced to a CCD camera, which allowed the single-shot acquisition of the optical signals from all fibers. In this way, it was possible to evaluate the polar distribution of the CL emission from a chemical reaction that took place at the liquid–solid boundary and its evolution with time. With this methodology, it is worth observing that the angular resolution can be easily improved by increasing the number of fibers and/or decreasing the core diameter of each fiber. Two different configurations have been studied: heterogeneous (HRP or ALP enzymes bound on a PMMA surface) and homogeneous (HRP enzyme free in solution). Experimental results showed a markedly anisotropic emission in the heterogeneous configuration, confirming that the photon emission resulting from the decay of the excited-state products of the CL reaction catalyzed by immobilized enzymes occurred close to the PMMA surface. It is worth noting that this behavior might not be confirmed for other CL systems, being dependent on the lifetime of intermediate products of the CL reaction [30]. Additionally, the presence of enhancers in the CL substrate could also affect the polar behavior of the emission (e.g., by introducing energy acceptors that represent the actual emitting species of the CL reaction). For the homogeneous configuration, the CL emission was almost isotropic at short reaction times, while evolving towards an anisotropic emission over time. This suggested that absorption of the enzyme on the PMMA surface took place during the measurement, bringing the reaction volume closer and closer to the PMMA surface. The observed anisotropic behavior of the CL emission occurring when the enzymes catalyzing the CL reaction are in close proximity to the boundary between two dielectric media with different refractive indexes opens new perspectives in the design of CL biosensors. This phenomenon must be taken into consideration when designing miniaturized CL-based analytical devices or even exploited to improve the signal collection efficiency. Indeed, in many biosensor configurations the detector is placed close to the bottom part of a transparent substrate on which the CL reaction takes place. With this setup, a large fraction of emitted photons remains undetected, thus greatly reducing assay detectability. On the contrary, anisotropic coupling of the CL emission to a transparent substrate could be used to guide the emitted photons towards the light detector, thus improving light collection efficiency without using dedicated optics.

REFERENCES

1. Pinto Da Silva, L.; Esteves Da Silva, J.C.G. Firefly chemiluminescence and bioluminescence: Efficient generation of excited states. ChemPhysChem 2012, 13, 2257–2262.
2. Vacher, M.; Fdez Galván, I.; Ding, B.W.; Schramm, S.; Berraud-Pache, R.; Naumov, P.; Ferré, N.; Liu, Y.J.; Navizet, I.; Roca-Sanjuán, D.; et al. Chemi- and Bioluminescence of Cyclic Peroxides. Chem. Rev. 2018, 118, 6927–6974.
3. Magalhães, C.M.; Esteves da Silva, J.C.G.; Pinto da Silva, L. Chemiluminescence and Bioluminescence as an Excitation Source in the Photodynamic Therapy of Cancer: A Critical Review. ChemPhysChem 2016, 2286–2294.
4. Pires, N.; Dong, T.; Hanke, U.; Hoivik, N. Recent Developments in Optical Detection Technologies in Lab-on-a-Chip Devices for Biosensing Applications. Sensors 2014, 14, 15458–15479.
5. Mirasoli, M.; Guardigli, M.; Michelini, E.; Roda, A. Recent advancements in chemical luminescence-based lab-on-chip and microfluidic platforms for bioanalysis. J. Pharm. Biomed. Anal. 2014, 87, 36–52.
6. Roda, A.; Mirasoli, M.; Michelini, E.; Di Fusco, M.; Zangheri, M.; Cevenini, L.; Roda, B.; Simoni, P. Progress in chemical luminescence-based biosensors: A critical review. Biosens. Bioelectron. 2016, 76, 164–179.
7. Alahmad, W.; Uraisin, K.; Nacapricha, D.; Kaneta, T. A miniaturized chemiluminescence detection system for a microfluidic paper-based analytical device and its application to the determination of chromium(III). Anal. Methods 2016, 8, 5414–5420.

8. Marquette, C.A.; Blum, L.J. Chemiluminescent enzyme immunoassays: a review of bioanalytical applications. Bioanalysis 2009, 1, 1259–1269.
9. Chong, R.; Rho, J.E.R.; Yoon, H.J.; Rho, T.H.D.; Park, P.S.; Kim, Y.H.; Lee, J.H. 1,1′-Oxalyldiimidazole chemiluminescent enzyme immunoassay capable of simultaneously sensing multiple markers. Biosens. Bioelectron. 2012, 32, 19–23.
10. Fereja, T.H.; Hymete, A.; Gunasekaran, T. A Recent Review on Chemiluminescence Reaction, Principle and Application on Pharmaceutical Analysis. ISRN Spectrosc. 2013, 2013, 1–12.
11. Xie, H.; Wang, Z.; Kong, W.; Wang, L.; Fu, Z. A novel enzyme-immobilized flow cell used as end-column chemiluminescent detection interface in open-tubular capillary electrochromatography. Analyst 2013, 138, 1107–1113.
12. Zangheri, M.; Di Nardo, F.; Mirasoli, M.; Anfossi, L.; Nascetti, A.; Caputo, D.; De Cesare, G.; Guardigli, M.; Baggiani, C.; Roda, A. Chemiluminescence lateral flow immunoassay cartridge with integrated amorphous silicon photosensors array for human serum albumin detection in urine samples. Anal. Bioanal. Chem. 2016, 408, 8869–8879.
13. Lukosz, W.; Kunz, R.E. Light emission by magnetic and electric dipoles close to a plane dielectric interface II Radiation patterns of perpendicuar oriented dipoles. J. Opt. Soc. Am. 1977, 67, 1615–1619.
14. Lukosz, W. Light emission by magnetic and electric dipoles close to a plane dielectric interface III Radiation patterns of dipoles with arbitrary orientation. J. Opt. Soc. Am. 1979, 69, 1495.
15. Thompson, N.L.; Burghardt, T.P. Measurement of spatial and orientational distribution of fluorophores near planar dielectric interfaces. Biophys. Chem. 1986, 25, 91–97.

16. Enderlein, J.; Ruckstuhl, T.; Seeger, S. Highly efficient optical detection of surface-generated fluorescence. Appl. Opt. 1999, 38, 724.

17. Polerecký, L.; Hamrle, J.; MacCraith, B.D. Theory of the radiation of dipoles placed within a multilayer system. Appl. Opt. 2000, 39, 3968.

18. Blue, R.; Kent, N.; Polerecky, L.; McEvoy, H.; Gray, D.; MacCraith, B.D. Platform for enhanced detection efficiency in luminescence-based sensors. Electr. Lett. 2005, 41, 682–684.

19. Dasallas, L.L.; Jaculbia, R.B.; Balois, M.V.; Garcia, W.O.; Hayazawa, N. Position, orientation, and relative quantum yield ratio determination of fluorescent nanoemitters via combined laser scanning microscopy and polarization measurements. Opt. Mater. Express 2018, 8, 1290.

20. Ruckstuhl, T.; Verdes, D. Supercritical angle fluorescence (SAF) microscopy. Opt. Express 2004, 12, 4246. [Google Scholar] [CrossRef]

21. Winterflood, C.M.; Ruckstuhl, T.; Verdes, D.; Seeger, S. Nanometer axial resolution by three-dimensional supercritical angle fluorescence microscopy. Phys. Rev. Lett. 2010, 105, 1–4.

22. Bourg, N.; Mayet, C.; Dupuis, G.; Barroca, T.; Bon, P.; Lécart, S.; Fort, E.; Lévêque-Fort, S. Direct optical nanoscopy with axially localized detection. Nat. Photonics 2015, 9, 587–593.

23. James Shirley, F.; Neutens, P.; Vos, R.; Mahmud-Ul-Hasan, M.; Lagae, L.; Verellen, N.; Van Dorpe, P. Supercritical Angle Fluorescence Characterization Using Spatially Resolved Fourier Plane Spectroscopy. Anal. Chem. 2018, 90, 4263–4267.

24. Bernini, R.; Cennamo, N.; Minardo, A.; Zeni, L. Planar waveguides for fluorescence-based biosensing: Optimization and analysis. IEEE Sens. J. 2006, 6, 1218–1225.

25. Kurzbuch, D.; Bakker, J.; Melin, J.; Jönsson, C.; Ruckstuhl, T.; MacCraith, B.D. A biochip reader using super critical angle fluorescence. Sens. Actuators B Chem. 2009, 137, 1–6.

26. Baldini, F.; Carloni, A.; Giannetti, A.; Porro, G.; Trono, C. An optical PMMA biochip based on fluorescence anisotropy: Application to C-reactive protein assay. Sens. Actuators B Chem. 2009, 139, 64–68.

27. Zhou, X.-H.; Liu, L.-H.; Xu, W.-Q.; Song, B.-D.; Sheng, J.-W.; He, M.; Shi, H.-C. A reusable evanescent wave immunosensor for highly sensitive detection of bisphenol A in water samples. Sci. Rep. 2014, 4, 17–20.

28. Hung, T.Q.; Sun, Y.; Poulsen, C.E.; Linh-Quyen, T.; Chin, W.H.; Bang, D.D.; Wolff, A. Miniaturization of a micro-optics array for highly sensitive and parallel detection on an injection moulded lab-on-a-chip. Lab Chip 2015, 15, 2445–2451.

29. Nguyen, T.; Anh Ngo, T.; Duong Bang, D.; Wolff, A. Optimising the supercritical angle fluorescence structures in polymer microfluidic biochips for highly sensitive pathogen detection: A case study on: Escherichia coli. Lab Chip 2019, 19, 3825–3833.

30. Roda, A.; Pasini, P.; Baraldini, M.; Musiani, M.; Gentilomi, G.; Robert, C. Chemiluminescent imaging of enzyme-labeled probes using an optical microscope-videocamera luminograph. Anal. Biochem. 1998, 257, 53–62.

31. Chowdhury, M.H.; Malyn, S.N.; Aslan, K.; Lakowicz, J.R.; Geddes, C.D. Multicolor directional surface plasmon-coupled chemiluminescence. J. Phys. Chem. B 2006, 110, 22644–22651.

32. Chowdhury, M.H.; Malyn, S.N.; Aslan, K.; Lakowicz, J.R.; Geddes, C.D. First observation of surface plasmon-coupled chemiluminescence (SPCC). Chem. Phys. Lett. 2007, 435, 114–118.

33. Roda, A.; Mirasoli, M.; Dolci, L.S.; Buragina, A.; Bonvicini, F.; Simoni, P.; Guardigli, M. Portable device based on chemiluminescence lensless imaging for personalized diagnostics through multiplex bioanalysis. Anal. Chem. 2011, 83, 3178–3185.
34. Schneider, C.A.; Rasband, W.S.; Eliceiri, K.W. NIH Image to ImageJ: 25 years of image analysis. Nat. Methods 2012, 9, 671–675.
35. Adam, W.; Bronstein, I.; Edwards, B.; Engel, T.; Reinhardt, D.; Schneider, F.W.; Trofimov, A.V.; Vasil'ev, R.F. Electron exchange luminescence of spiroadamantane-substituted dioxetanes triggered by alkaline phosphatases. Kinetics and elucidation of pH effects. J. Am. Chem. Soc. 1996, 118, 10400–10407.
36. Marzocchi, E.; Grilli, S.; Della Ciana, L.; Prodi, L.; Mirasoli, M.; Roda, A. Chemiluminescent detection systems of horseradish peroxidase employing nucleophilic acylation catalysts. Anal. Biochem. 2008, 377, 189–194.
37. Roda, A.; Pasini, P.; Musiani, M.; Girotti, S.; Baraldini, M.; Carrea, G.; Suozzi, A. Chemiluminescent low-light imaging of biospecific reactions on macro- and microsamples using a videocamera-based luminograph. Anal. Chem. 1996, 68, 1073–1080.
38. Liu, C.; Meenan, B.J. Effect of Air Plasma Processing on the Adsorption Behaviour of Bovine Serum Albumin on Spin-Coated PMMA Surfaces. J. Bionic Eng. 2008, 5, 204–214.
39. Palacio, M.; Schricker, S.; Bhushan, B. Morphology and protein adsorption characteristics of block copolymer surfaces. J. Microsc. 2010, 240, 239

CONCLUSIONS AND FUTURE PERSPECTIVES

DNA nanotechnology has the potential for self-assembly and formation of programmable nanostructures, leading to their application as coding materials in many research fields. Indeed, structural DNA nanotechnology has already become an interdisciplinary research field, in which chemists, material scientists, computational theorists, biologists and physicists work together to tackle important problems [1]. Currently, many efforts have been made, but there is the urgent need to develop intelligent and refined structures that have viable physical, chemical, and biological applications [2]. The DNA nanotechnology field has just started to progress towards the industry-friendly use and it probably will require collaborative effort from multiple disciplines to overcome some challenges, such as scalability and stability of DNA nanomaterials, as well as a balance between design simplicity and functional complexity, especially for in vivo applications [3]. However, DNA nanotechnology will become a powerful tool for the traditional approaches to manipulate and tune biological information, because of the progress that has already been shown during the past decades [4]. In the next future, it is certain that more and more functional and intelligent nanomaterials based on DNA will be developed for biosensing and therapy applications. In the meantime, it is clear that more efforts should also be devoted for the improvement of the safety of DNA-based nanomaterials [5]

REFERENCES

1. Pinheiro AV, Han D, Shih WM, Yan H. Challenges and opportunities for structural DNA nanotechnology. Nat Nanotechnol. 2011;6(12):763-772.
2. Zahid M, Kim B, Hussain R, Amin R, Park SH. DNA nanotechnology: a future perspective. Nanoscale Res Lett. 2013;8(1):119. Published 2013 Mar 4. doi:10.1186/1556-276X-8-119.
3. Chidchob P, Sleiman HF. Recent advances in DNA nanotechnology. Curr Opin Chem Biol. 2018 Oct;46 63-70.
4. Chen YJ, Groves B, Muscat RA, Seelig G. DNA nanotechnology from the test tube to the cell. Nat Nanotechnol. 2015 Sep;10(9):748-60. doi: 10.1038/nnano.2015.195. PMID: 26329111.
5. Kumar V, Palazzolo S, Bayda S, Corona G, Toffoli G, Rizzolio F. DNA Nanotechnology for Cancer Therapy. Theranostics 2016; 6(5):710-725.